

UNIVERSITÀ DEGLI STUDI DI NAPOLI “FEDERICO II”



DIPARTIMENTO DI FARMACIA

Dottorato di Ricerca
in Scienza del
Farmaco XXVIII
ciclo

*Computational methods applied to
drug discovery: the rational
design of dual inhibitors of FAAH
and COX*

PhD Candidate: CARMINE MARCO MORGILLO
Supervisor: Dr. BRUNO CATALANOTTI
Co-tutor: Prof. F. JAVIER LUQUE
Coordinator: Prof. MARIA VALERIA D’AURIA

“– Dico a voi, ehi, paladino! – insisté Carlomagno.

– Com’è che non mostrate la faccia al vostro re?

La voce uscì netta dal barbazzale.

– Perché io non esisto, sire.

– Mah, mah! – fece Carlomagno.

– E com’è che fate a prestar servizio, se non ci siete?

*– Con la forza di volontà, – disse Agilulfo, – e la fede nella nostra santa
causa!”*

<i>Abstract</i>	vii
Abbreviations	ix
<i>RATIONAL DESIGN OF DUAL INHIBITORS OF FAAH AND COX</i>	1
1. Introduction.....	1
1.1 Connections between pain and inflammation.....	1
1.2 Interacting pathways between endocannabinoids and prostanoids	1
1.3 FAAH/COX dual inhibition efficacy in pain-relief treatments	4
1.4 Structural characterization of Fatty Acid Amide Hydrolase	5
1.5 FAAH inhibition and current state of the art	7
1.6 NSAIDs derivatives as FAAH/COX dual inhibitors.....	9
2. Aims of the study	11
3. Experimental section.....	13
3.1 Molecular docking.....	13
3.2 Molecular Dynamics.....	13
3.3 Free energies calculations	14
3.3.1 MM/PBSA method.....	14
3.3.2 SIE method	15
3.3.3 QM/MM calculations.....	15
3.3.4 Thermodynamic integration	16
3.4 Homology building	17
4. Inhibition of FAAH by the enantiomers of Flu-AM1 and Ibu-AM5	19
4.1 Introduction	19
4.2 Pharmacological studies.....	19
4.3 Validation of the computational protocol	20
4.4 Molecular docking of the enantiomers of Flu-AM1 and Ibu-AM5	21
4.5 Molecular dynamics studies of the enantiomers of Flu-AM1 and Ibu-AM5 ..	23
4.6 Comparison of the binding mode of the enantiomers of Flu-AM1 and Ibu-AM5.....	26
4.7 Comparison with other non-covalent FAAH inhibitors	27
4.8 Guidelines for drug design.....	28

5. Inhibition of FAAH by 2-(4-((2-(Trifluoromethyl)Pyridin-4-yl)amino)phenyl)propan Amides (TPA)	31
5.1 Rational design of TPA derivatives and TPA5 pharmacological profile	31
5.2 Molecular docking of TPA5	32
5.3 Molecular dynamics and free energies calculation of TPA5 in the competitive site.....	34
5.4 Structure Activity Relationships of TPA derivatives	39
5.5 Comparison with other FAAH inhibitors.....	45
6. Structural investigation of the allosteric site in FAAH	47
6.1 Pocket detection	49
6.2 Molecular docking in the allosteric pocket.....	53
6.3 Molecular dynamics studies in the allosteric pocket	54
6.3.1 Ibu-AM5 MD simulations	54
6.3.2 Flu-AM1 MD simulations	58
6.3.3 TPA27 MD simulations.....	61
6.4 Profen amide derivatives.....	63
6.4.1 Ibu-AM5 derivatives	63
6.4.2 Flu-AM1 derivatives.....	67
7. Identification and rational design of novel peptides that interfere with the interaction between hUbA1/UbcH10.	71
7.1 Introduction	71
7.2 Building of the 3D trimeric complex of hUbA1 with doubly loaded Ub	72
7.3 Building of the quaternary complex hUbA1~Ub(T)-Ub(A)-UbcH10	77
7.4 Final refinement of the tetrameric complex	81
7.5 Rational design of peptides that interfere with the formation of the tetrameric complex.....	86
7.6 Conclusions	88
7.7 Experimental section.....	89
7.7.1 Homology building.....	89
7.7.2 General strategy for docking calculations.....	90
7.7.3 The UbA1~Ub(T)-Ub(A)-UbcH10 complex	91
7.7.4 Molecular Dynamics	92

7.7.5 Steered Molecular Dynamics and refinement of the final complex....	93
7.7.6 Binding free energy evaluation and virtual alanine scanning	93
8. Structural studies of small Peptide Nucleic Acid, a new inhibitor of miR-509-3p involved in the regulation of Cystic Fibrosis Disease-Gene expression	95
8.1 Introduction	95
8.2 MD simulations of the heteroduplex miR-509-3p/PNA1 and miR-509- 3p/PNA2	97
8.3 Experimental section.....	99
9. Conclusions.....	101
Bibliography.....	103

Abstract

The search for effective and safe drugs in pain-relief treatment represents a great challenge for medicinal chemists. Lipid derived mediators, such as endocannabinoids, may have different roles as agonists of cannabinoid receptors, relieving pain, or as substrates of cyclooxygenase (COX), generating the pro-inflammatory prostamides. Moreover, the tissue-protective endocannabinoid anandamide is metabolised by fatty acid amide hydrolase (FAAH). Therefore, a new challenging approach in pain-relief might be the development of dual action FAAH/COX inhibitors.

The purpose of this thesis is to apply computational methods in drug discovery to assist medicinal chemistry studies targeting the rational design of novel FAAH/COX inhibitors, and to exploit structural studies relative to two side projects on other biological targets.

The wider project of this thesis explores the mechanism of action and the rational design of novel FAAH/COX dual inhibitors. The reversible mixed-type inhibitors Flu-AM1 and Ibu-AM5, derivatives of flurbiprofen and ibuprofen, respectively, retain similar COX inhibitory properties and are more potent FAAH inhibitors than the parent compounds. Applying a combination of molecular docking, MD simulations and free energy evaluation of the ligand-receptor complex, the binding mode of the enantiomer forms of Flu-AM1 and Ibu-AM5 has been found in the substrate access channel of FAAH and has been supported by studies of site-directed mutagenesis. The substitution of the isobutyl group of Ibu-AM5 with 4-(2-((trifluoromethyl)pyridin-4-yl)amino group led to the design of TPA5 derivative, which showed an inhibitory activity ($IC_{50} = 0.59 \mu\text{M}$) similar to the lead compound (Ibu-AM5, $IC_{50} = 0.52 \mu\text{M}$). Kinetic studies of TPA5 revealed that it is a pure competitive inhibitor of rat FAAH and molecular modeling studies supported a binding mode that overlap the anandamide analog MAFP. Among TPA5 derivatives, compound TPA27 exhibited a 10-fold enhancement in the inhibitory profile against FAAH ($IC_{50} = 0.058 \mu\text{M}$). Thermodynamic Integration calculations performed to complete the transformation of TPA5 in TPA27 yielded a free energy difference of 0.3 kcal/mol, which indicates a slight lower affinity of TPA27 with respect to TPA5, in the competitive binding site. Kinetics studies showed that TPA27 could be considered the first non-competitive reversible FAAH inhibitor reported so far, and that it more likely binds to an allosteric site.

Differences in the inhibitory potency against rat and mouse FAAH for all compounds studied suggested different aminoacid composition of both competitive and non-competitive binding sites. This information was used as criteria of selection for a putative allosteric site found between the cytosolic port and the interface of the FAAH monomers. Computational studies in the allosteric site allowed the definition of the binding mode of Ibu-AM5 and

TPA27. Nevertheless, a series of derivatives of Ibu-AM5 and Flu-AM1 were designed in order to get more information on the structure-activity relationships, leading to the identification of novel derivatives with improved activity against FAAH (Ibu-AM56, $IC_{50} = 0.08 \mu\text{M}$; Ibu-AM57, $IC_{50} = 0.1 \mu\text{M}$; Flu-AM3, $IC_{50} = 0.02 \mu\text{M}$).

Finally, the thesis also reports the results of two other projects: i) the design of potential anticancer peptides that interfere in the formation of the tetrameric complex hUbA1/Ubch10/Ub², key intermediate of the ubiquitination cascade.; ii) structural studies on the hybridization of PNA of different length with miR-509-3p, involved in regulating the expression of the CFTR gene, as a way to validate a potential new strategy for the treatment of Cystic Fibrosis.

Abbreviations

Abbreviations used for amino acids and designation of peptides follow the rules of the IUPAC-IUB Commission of Biochemical Nomenclature in *J. Biol. Chem.* 1972, 247, 977-983. Amino acid symbols denote L-configuration unless indicated otherwise. The following additional abbreviations are used:

2-AG, 2-ArachidonoylGlycerol;
3D, three-dimensional;
 Δ TM, deleted transmembrane;
AA, Arachidonic Acid;
ABP, Acyl-chain Binding Pocket;
AD, Adenylation Domain;
AEA, *N*-Arachidonoylethanolamine;
Ago, Argonaute;
CF, Cystic Fibrosis;
COX, Cyclooxygenase;
CP, Cytosolic Port;
FAAH, Fatty Acid Amide Hydrolase;
FAE, Fatty Acid Ethanolamide;
FCCH, First Catalytic Cysteine Half-domain;
GALS, Lamarckian Genetic Algorithm;
hFAAH, human FAAH;
h/rFAAH, humanized rat FAAH;
MAC, Membrane Access Channel;
MAFP, Methyl Arachidonyl Fluorophosphonate;
MD, Molecular Dynamics;
mFAAH, mouse FAAH;
MM, Molecular Mechanics;
MM/GBSA, Molecular Mechanics Generalized Born Surface Area;
MM/PBSA, Molecular Mechanics Poisson Boltzmann Surface Area;
miRNA, microRNA;
mRNA, messenger RNA;
NSAID, Non-Steroidal Anti-Inflammatory Drug;
OEA, *N*-Oleoylethanolamine;
ON, Oligonucleotide;
PB, Poisson-Boltzmann;
PDB, Protein Data Bank;
PEA, *N*-Palmitoylethanolamine;
PG, Prostanoid;
PGE₂, Prostaglandin E₂;
PGI₂, Prostacyclin;
PNA, Peptide Nucleic Acid;
PPAR α , Peroxisome Proliferator-Activated Receptor α ;
QM/MM, Quantum Mechanical Molecular Mechanics;
rFAAH, rat FAAH;
RMSD, Root Mean Square Deviation;
SA, Surface Area;

SAR, Structure-Activity Relationships;
SCCH, Second Catalytic Cysteine Half-domain;
ScUba1, Saccharomyces Cerevisiae UbA1;
SIE, Solvated Interaction Energy;
SMD, Steered Molecular Dynamics;
spUba1, Scizosaccharomyces Pombe UbA1;
TI, Thermodynamic Integration;
TPA, 2-(4-((2-(Trifluoromethyl)Pyridin-4-yl)amino)phenyl)propan Amides;
TRPV1, Transient Receptor Potential Vanilloid type-1;
TXA₂, Thromboxane A₂;
Ub, Ubiquitin;
Ub(A), Activated Ubiquitin;
UbA, Ubiquitin Activating enzyme;
Ubc, Ubiquitin Conjugation enzyme;
Ub(T), Thioester-linked Ubiquitin;
UFD, Ubiquitin Folding Domain;

RATIONAL DESIGN OF DUAL INHIBITORS OF FAAH AND COX

1. Introduction

1.1 Connections between pain and inflammation

The current treatment for acute and chronic pain consists in the administration of different classes of drugs acting through distinct molecular mechanisms involved in pain generation, such as i) agonists of opioid receptors, ii) gabapentinoids, which inhibit voltage-dependent calcium channels (VDCCs), and iii) nonsteroidal anti-inflammatory drugs (NSAIDs), which are inhibitors of Cyclooxygenase (COX), an enzyme involved in the generation and propagation of inflammation. These drugs are subject to some limitations due to common side effects that poses difficulties in the handling of the dose, and to the possibility to induce addiction or dependence as in the opioids case. Albeit in the last decades substantial advances in the pain-relief treatment were made, the search for effective and safe drugs still represents a great challenge for medicinal chemists. As an example, one can mention inflammation bowel disease, where pain conditions arise from non-resolving inflammation [1], which involves complex mechanisms and many different actors. Among them, lipid-derived mediators, such as prostanoids, may promote and maintain pain and inflammation. Other lipid derived mediators, such as endocannabinoids, may have different roles as agonists of cannabinoid receptors, relieving pain, or as substrates of COX, generating the pro-inflammatory prostamides. As suggested by numerous evidences, functional and biochemical interactions support the existence of a cross-talk between endocannabinoids and prostanoids signalling pathways [2]. Since the two most studied endocannabinoids, 2-arachidonoylglycerol (2-AG) and *N*-arachidonylethanolamine (anandamide, AEA) present some redundancy in the way they are metabolised, a new challenge might be the development of multitarget drugs, inhibiting fatty acid amide hydrolase (FAAH) and cyclooxygenase (COX) as molecular targets for pain-relief and anti-inflammatory therapy.

1.2 Interacting pathways between endocannabinoids and prostanoids

2-AG and fatty acid ethanolamines (FAEs) such as AEA, *N*-palmitoylethanolamine (PEA), and *N*-oleoylethanolamine (OEA) (Fig. 1), are a family of signalling lipids involved in the regulation of a wide range of physiological and pathological processes, including pain and inflammation.

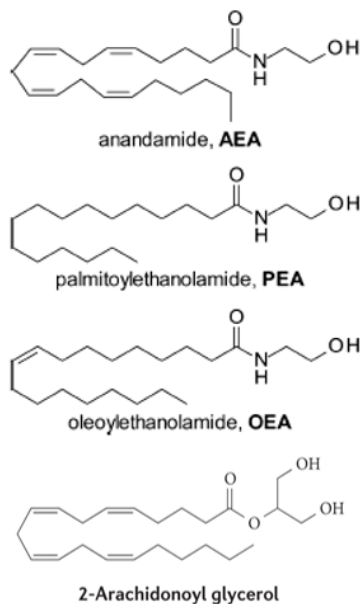


Figure 1: Chemical structure of the substrates of FAAH.

AEA modulates nociception and mediates the majority of its biological effects acting as an endogenous agonist of G-protein coupled CB₁ and CB₂ cannabinoid receptors [3]. During inflammation, activation of cannabinoid receptors results in attenuation of neutrophil migration and immune-cell recruitment, [4]. Moreover, AEA also targets the transient receptor potential vanilloid type 1 (TRPV1) but the effects of this interaction remains unclear [5].

OEA and PEA exhibit little activity at cannabinoid receptors, but may affect nuclear peroxisome proliferator-activated receptor- α (PPAR α) and, to a lesser extent, GPR119 [6].

FAEs are produced from phospholipid precursors in membranes by very different pathways on the basis of their physiological demand. Therefore, the signalling activity of these substances is strictly dependent on the enzymes responsible for their formation and degradation [7]. AEA is mainly hydrolysed by FAAH into arachidonic acid (AA) and ethanolamine [8], while 2-AG is also FAAH substrate, but is mostly inactivated by monoacylglycerol lipase (MAGL) [9] (Fig. 2).

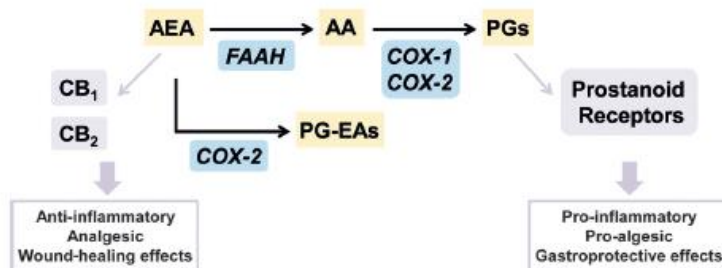


Fig. 2: Simplified scheme of the endocannabinoid and prostanoid signalling pathways with some nodes of biological interactions (from ref. 1).

FAAH inhibition will lead to increased concentration of AEA, and therefore the development of FAAH inhibitors has been examined in the search of novel strategies to reduce neuropathic pain. This strategy was proven to be effective in many animal models, as exemplified in the work by Sharkey and coworkers, who showed that the use of selective FAAH inhibitors reduced the inflammatory symptoms in animal models of intestinal inflammation [10].

COX is membrane-bound enzyme that catalyses the cyclooxygenation of arachidonic acid (AA) in a variety of pro-algesic and inflammatory eicosanoids that includes prostaglandin E₂ (PGE₂), prostacyclin (PGI₂) and thromboxane A₂ (TXA₂) [11] (Fig. 2). These signalling molecules regulate important physiological and pathological functions through the activation of selective G-protein-coupled receptors, such as inflammation, mucosal protection, cardiovascular homeostasis and cancer [12]. There are two COX isoforms, COX-1 and COX-2, which share ~60% sequence identity. COX-1 is expressed in most tissues and is considered to be a constitutive enzyme, while COX-2 is normally expressed in brain, spinal cord and kidney and is considered an inducible enzyme [13]. COX-2 expression increases in innate immune response and other host defence mechanisms during tissue damage or inflammation in response to cytokines, mitogens and growth factors [14].

In particular, COX-2 mediates the transformation of the endocannabinoids 2-AG and AEA into prostaglandin-glycerol esters and prostaglandin-ethanolamides (prostamides, PG-EAs), respectively [15]. These products are pro-algesic agents and do not show interactions with prostanoid or endocannabinoid receptors [16], but their mechanism of action is still under investigation. Nevertheless, they represent a potential interplay between endocannabinoid and prostanoid signalling networks. Therefore, COX-2 mediated transformations of AEA and 2-AG into pro-nociceptive and pro-inflammatory substances have led to the hypothesis of the presence of multiple functional connections between endocannabinoid and prostanoid systems, which may offer new molecular targets in the development of multitarget FAAH/COX inhibitors.

1.3 FAAH/COX dual inhibition efficacy in pain-relief treatments

Traditionally, NSAIDs are used in the treatment of mild to moderate pain and in co-administration with opioids in the management of moderate to severe pain [17]. The clinical effects of NSAIDs are based on the inhibition of the two COX isoforms, COX-1 and COX-2, which catalyse the conversion of membrane-derived AA into the prostaglandin endoperoxides PGG₂ and PGH₂ [18]. One of the major problems associated with the use of NSAIDs is the high incidence of gastrointestinal adverse effects, due to inhibition of the production of gastro-protective prostaglandins, and possibly to topical effects in the gastric epithelium [19]. Recently, the use of a highly selective FAAH inhibitor was found to reduce by almost an order of magnitude the dose of NSAID diclofenac required for analgesia in a model of visceral pain [20]. This study indicated that the analgesic actions of NSAIDs are enhanced in a synergistic manner by drugs that inhibit FAAH. In fact, by increasing AEA levels, FAAH inhibitors enhance the ability of this compound to control emerging nociceptive signals [21], such as those mediated by prostanoids, resulting in an overpotentiation of NSAID-mediated analgesia. Apart from the increase in the analgesic action of the NSAIDs, FAAH inhibitors reduce the frequency and severity of gastric side effects exerted by those compounds [22]. However, the recent failure of a selective FAAH inhibitor in clinical trial in patients with osteoarthritic pain [23] has demonstrated that the increased levels in AEA are suboptimal due to COX-2 transformation of this substrate to PG-EAs, owing to the pro-nociceptive effects of prostamide F2 α [24]. Therefore, besides gastro-protective effects, combined FAAH and COX inhibition may guarantee the therapeutic effectiveness through additive or synergistic effects rather than the use of selective compounds for the treatment of pain [25].

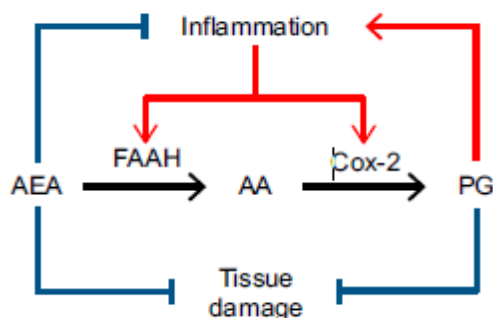


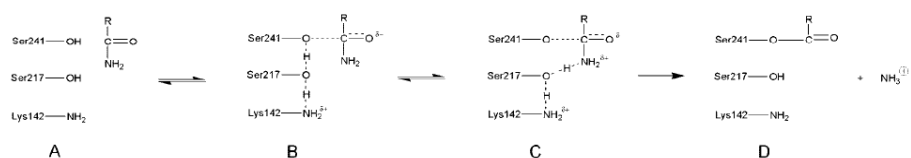
Fig. 3. Targeting both FAAH and COX to treat pain and inflammation. In multiple inflammatory condition the elevated expression of FAAH and COX-2 may exacerbate inflammation by lowering levels of anti-inflammatory and tissue-protective anandamide (AEA), while concurrently increasing levels of arachidonic acid (AA) and its prostanoid (PG) metabolites.

The co-administration of drugs, either given separately or as a multicomponent formulation, has the disadvantage that different rates and

processes in metabolism of the individual drugs can trigger a wide variation in delivered dosages, which opens a potential risk for drug interactions and thereby could affect the treatment outcome, showing unexpected side effects [26]. An alternative approach, termed “designed multiple ligands”, concerns the use of a single compound with efficacy towards both targets [27]. In this approach, the pharmacokinetic properties of the formulations will be less complex than in the multicomponent strategy, but a potential drawback is the loss of flexibility in dosing. Therefore, dual inhibitors of FAAH and COX may be a promising therapeutic strategy for providing superior efficacy and greater safety than current non-narcotic analgesics [28].

1.4 Structural characterization of Fatty Acid Amide Hydrolase

FAAH is an integral membrane enzyme that hydrolyses the endocannabinoid AEA and related amidated signalling lipids. Being a member of the amidase signature superfamily of serine hydrolases [29] FAAH serves its hydrolytic function in alkaline conditions (optimum is pH 9.0), revealing a titrable group with a pKa of ~7.9 (presumably Lys142). Mutation of Lys142 creates altered pH rate profiles that are similar to those of histidine mutants in classical Ser/His/Asp proteases. Unlike other amidases, FAAH is characterised by a unique Ser/Ser/Lys catalytic triad [30], where Ser241 acts as nucleophile, Ser217 stabilises the formed negative charge, and Lys142 acts as active base for catalysis [31]. The three-dimensional (3D) structure of FAAH was firstly solved by X-ray crystallography in complex with the covalent inhibitor methyl arachidonyl fluorophosphonate (MAFP) bound to Ser241, thus demonstrating that Ser241 is the nucleophilic residue [32]. Scheme 1 shows the catalytic mechanism for the acylation step of amide hydrolysis, and Fig. 4 shows that Ser241 was covalently attached to the phosphonate inhibitor, while the bridging Ser217 was hydrogen bonded to Lys142.



Scheme 1: Proposed mechanism for the acylation step of amide hydrolysis catalysed by FAAH. Lys142, initially in a deprotonated state (A), abstracts a proton from Ser217, which in turn abstracts a proton from the Ser241 nucleophile (B). Attack of the nucleophile on the substrate carbonyl is proposed to occur in a coupled manner with proton donation from Ser217 to the nitrogen atom of the amide substrate (C). This latter step requires the coincidental donation of a proton from Lys142 to Ser217, resulting in the formation of an acyl intermediate where both Lys142 and Ser217 have returned to their initial protonation states (D). (from ref. 30)

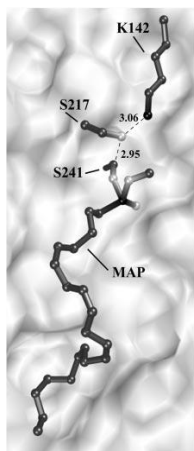


Fig. 4: The catalytic triad of FAAH, bearing the Ser241 bound to the inhibitor metoxyarachidonoyl phosphonate (MAP). Distances among Ser241, Ser217 and Lys142 are shown in Å. (from ref. 30)

Endogenous FAAH substrates, such as AEA, serve regulatory functions in the body and have been implicated in a variety of pathological conditions including pain, inflammation, sleep disorders, anxiety, depression and vascular hypertension, which explains the interest in the development of FAAH inhibitors [33]. FAAH is a homodimer and, in each monomer, the core structure adopts an α/β fold with a twisted 11-strand β -sheet in the centre and 24 α -helices surrounding the sheet (Fig. 5A). The catalytic triad is located in the centre of the enzyme. Three principal channels spread out from the catalytic core (Fig. 5B), known as i) the membrane access channel (MAC), which points to the protein surface facing the membrane bilayer and is considered the channel that gives access to the substrate; ii) the acyl-chain binding pocket (ABP), which binds the substrate acyl chain during the enzymatic reaction; and iii) the cytosolic port (CP), which connects the active site to the cytosol, and therefore it may allow the entrance of water molecules to the catalytic centre and bring out the ethanolamine produced in the enzymatic hydrolysis. In the proximal portion of the active site, the MAC and the ABP merge into a single section. Together, MAC and ABP form a wide channel that is predominantly hydrophobic in nature on one side and moderately polar on the other side.

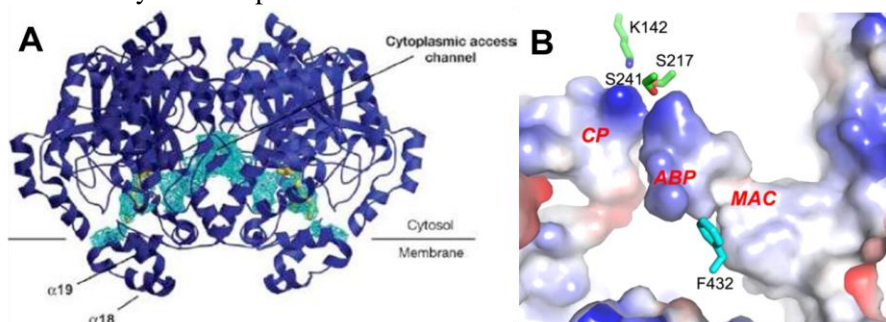


Fig. 5: 3D structure and localization of FAAH (A, from ref. 30) and representation of the principal structural features (B, from ref. 44). Principal channels are shown in surface, while Phe432 and catalytic triad are shown in sticks.

1.5 FAAH inhibition and current state of the art

A variety of selective FAAH inhibitors have already been described and, judging from the reported patents, the development of high-throughput screening strategies for the enzyme [34], and the recent creation of a web server for binding affinity prediction of ketoxazole derivatives against FAAH [35], there is renewed interest in the development of FAAH inhibitors.

Different structural classes of FAAH inhibitors have been reported including α -keto heterocycles, carbamates, piperidine ureas, arylureas and others [36]. Several rat FAAH (rFAAH) or humanized rat FAAH (h/rFAAH) structures have been stored in the PDB database. The first X-ray structure of rFAAH was determined for the deleted transmembrane (Δ TM) enzyme in complex with an AEA analogue, the irreversible inhibitor MAFP at 2.8 Å resolution (PDB code: 1MT5) [32]. Given the multiple membrane association possibilities of FAAH [37], protein expression and purification have been challenging for the human isoform (hFAAH), which shares ~82% sequence identity with rFAAH. Therefore, due to the difficulties to solve the 3D human structure, a h/rFAAH structure was solved at 2.5 Å (PDB code: 2VYA) in complex with the piperidine-based inhibitor PF-750. In this structure, six amino acids of the active site were mutated into those of the hFAAH enzyme (namely Leu192Phe, Phe194Tyr, Ala377Thr, Ser435Asn, Ile491Val, and Val495Met) [38]. The h/rFAAH structure showed similar structural features as rFAAH. A remarkable difference was the orientation of Phe432 at the interface between ABP and MAC pockets. The presence of different classes of inhibitors induce a rotation by about 80° along the C α -C β axis of Phe432 (for instance, PF-750 in the h/rFAAH structure vs. MAFP in the rFAAH, Fig. 6A). Thus, the MAC pocket of h/rFAAH in presence of PF-750 was remarkably larger than in rFAAH. A more pronounced reshaping of the channels may be observed from the comparison of rFAAH bound to carprofen (PDB code: 4DO3 [39]) and MAFP, where the different orientation of Phe432 lead to a wider channel in the case of carprofen binding, as from the smaller occupancy of the channel by carprofen (Fig. 6B). This led to the suggestion that the flexibility of Phe432 sidechain might help the FAAH substrate to switch into pre-active conformations for hydrolysis, located in either ABP or MAC during catalysis. Following the first h/rFAAH structure, several additional FAAH structures bound with different covalent inhibitors were determined, confirming the structural flexibility of Phe432 [38, 40-44].

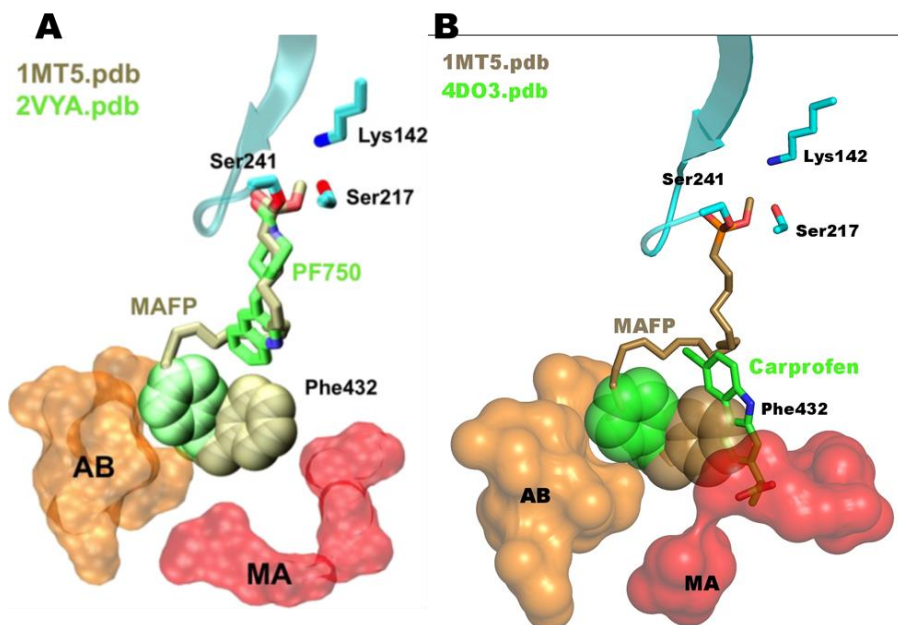


Fig. 6. Superimposition of the crystal structures of the rat FAAH covalently bound to methyl arachidonoyl fluorophosphonate (MAFP, 1MT5.pdb) with: A) h/rFAAH in complex with piperazine-based inhibitor PF-750 (2VYA.pdb); B) rFAAH in complex with carprofen (4DO3.pdb). The covalently bound MAFP (tan), PF-750 and carprofen (green) inhibitors, as well as the catalytic Ser241-Ser217-Lys142 residues (cyan) are shown in sticks. The two structures share a similar active site with one remarkable difference at the interface between the MAC and ABP channels, given by the rotation of the interface residue Phe432 (shown in space-filling representation).

The first attempts to design FAAH inhibitors concerned the use of natural substrates of FAAH as a template. This generated the AEA analogue MAFP inhibitor and trifluoromethyl ketones. These series of FAAH inhibitors were characterised by the formation of a covalent bond with the nucleophilic Ser241, blocking the catalytic function as long as the inhibitor remained irreversibly bound to the enzymatic pocket. However, these classes of inhibitors were not selective, inhibiting other serine hydrolases. Later, several reversible inhibitors were discovered, such as α -ketoesters, α -ketoamides, and α -ketoheterocycles, including the highly selective OL135 [45]. Very recently, a new series of α -ketoheterocycles compounds, derived from the inhibitor OL135, have been described as irreversibly targeting a cysteine in the FAAH catalytic site (Cys269), while also forming a reversible covalent bond with Ser241 [46]. Another class of irreversible FAAH inhibitors was characterized by a carbamic moiety functionalized with aryl or alkyl group at their O- and N- termini [47, 48]. URB524 is the first potent compound identified in the carbamate-based inhibitors series ($IC_{50} = 63$ nM). Modifications in URB524 led to the more potent URB597 ($IC_{50} = 4.6$ nM) [49]. Recently, a brain impenetrable member of this class of compounds was disclosed (namely URB937, $IC_{50} = 26.8$ nM), with substantial analgesic effects in animal models [21]. Crystallographic and theoretical studies have shown that carbamate-

based inhibitors act via the formation of covalent bond with Ser241 [42, 50, 51]. Replacing the carbamic group by the urea functionality has led to the discovery of a newer class of FAAH inhibitors [36]. This series of inhibitors showed similar behaviour compared to carbamate-based inhibitors, forming a covalent bond with Ser241. In particular, compounds bearing a cyclic piperidine/piperazine urea scaffold, such as PF-750 ($IC_{50} = 16.2$ nM), PF-622 ($IC_{50} = 33.0$ nM) and urea JNJ1661010 ($IC_{50} = 33$ nM) [52], showed improved selectivity in the inhibition of FAAH [53].

The profile of FAAH inhibitors seem appropriate for pain-relief, although a lack of effect after repeated administration has been reported in a preclinical model [54]. Even more striking is the failure of an irreversible inhibitor of the FAAH, PF04457845, in clinical trials for the osteoarthritis [23]. A possible explanation of this failure could be that although FAAH is blocked, the substrate AEA is consumed by COX-2, undermining the analgesic effect [55].

1.6 NSAIDs derivatives as FAAH/COX dual inhibitors

Another approach to pain relief therapy consists of the inhibition of FAAH and COX enzymes through a multitarget inhibitor. NSAIDs are known for their anti-inflammatory and painkiller actions, inhibiting COX enzymes. Furthermore, some NSAIDs (like ibuprofen, flurbiprofen, paracetamol and carprofen) are able to weakly inhibit FAAH (i.e. ibuprofen $IC_{50} = 134$ μ M and flurbiprofen $IC_{50} = 29$ μ M) [56, 57]. This finding provided a rationale for the design of molecules that carry multitarget FAAH and COX inhibitory activities. The development of single molecules with such a profile would exploit several advantages over combination therapies, including a more predictable pharmacokinetic profile and a decreased potential for drug-drug interactions. As a proof of concept, the groups of Prof. V. Onnis (Università di Cagliari, Italy) and Prof. C. J. Fowler (Umea University, Sweden) developed in 2003 a series of heteroaromatic ibuprofen anilides bearing substituted pyridine or pyrimidine groups, which showed improved analgesic activity and reduced gastrointestinal side effects relative to the parent acid [26]. In this regard, the *N*-3-methyl-pyridin-2-yl amide of ibuprofen (Ibu-AM5) was found to be the best analogue. This compound produced very low ulcerogenic effects compared to its parent molecule, ibuprofen. In a subsequent study, a series of other amide analogues derivative of ibuprofen were generated. Ibu-AM5 and Ibu-AM14 resulted to be the most potent inhibitors of rFAAH relative to ibuprofen, showing IC_{50} values of 0.65 and 3.6 μ M respectively [58]. Moreover, ibuprofen, Ibu-AM5 and Ibu-AM14 showed substrate-selective inhibition of COX-2, being poor inhibitors of the cyclooxygenation of AA by COX-2 and producing incomplete inhibition of this substrate. When AEA was used as substrate, these compounds were relatively potent inhibitors of COX-2, with IC_{50} values of ~ 6 (ibuprofen), ~ 19 (Ibu-AM5) and ~ 10 μ M (Ibu-AM14). Later, a small series of racemic

flurbiprofen and naproxen amide derivatives, bearing the same substitutions of Ibu-AM5, were also investigated [25]. Within this set, Flu-AM1 and Nap-AM1 demonstrated increased inhibitory potency for rFAAH, relative to the parent NSAIDs (flurbiprofen and Flu-AM1 FAAH IC₅₀ values of 29 and 0.44 μM respectively; naproxen and Nap-AM1 FAAH IC₅₀ values of > 100 and 0.74 μM respectively). Moreover, the ability for these compounds to inhibit the cyclooxygenation of AA by COX-1 and COX-2 and the cyclooxygenation of 2-AG by COX-2 was also tested. A similar pattern of COX-1 and COX-2 inhibition was observed between Flu-AM1 and parent compound, although in general 2- 3-fold higher concentration were required to produce the same effect as flurbiprofen (Flu-AM1: COX-1 AA IC₅₀ = 6.6 μM; COX-2 AA IC₅₀ = 42 μM; COX-2 2-AG IC₅₀ = 1.7 μM, respectively; flurbiprofen: COX-1 AA IC₅₀ = 3.6 μM; COX-2 AA IC₅₀ = 103 μM; COX-2 2-AG IC₅₀ = 1.3 μM, respectively). By contrast Nap-AM1 was a rather poor inhibitor of both COX isoforms (COX-1 AA IC₅₀ = 56 μM; COX-2 AA IC₅₀ > 100 μM; COX-2 2-AG IC₅₀ = 6.3 μM, respectively).

Very recently, a different strategy for the design of dual FAAH/COX inhibitors was proposed by the group of Piomelli and co-workers based on the integration of the alkyl carbamic acid group of the URB597 in the flurbiprofen structure. Among these derivatives, the compound ARN2508 showed submicromolar activity against rFAAH, ovine COX-1 and human COX-2 [59]. However, this compound blocks irreversibly both FAAH and COX enzymes.

2. Aims of the study

The main aim of the PhD project herein presented was the design of novel dual inhibitors of FAAH and COX.

NSAIDs amide derivatives Flu-AM1 and Ibu-AM5 represented valuable leads for the design of novel dual inhibitors, considering their pharmacological profile and mechanism of action. Indeed, they showed an increased FAAH activity and comparable COX inhibition with respect to parent NSAIDs. Moreover, they are reversible inhibitors, showing a mixed type inhibition kinetics.

Previous efforts aimed at improving the activity of ibuprofen amide derivatives using classical medicinal chemistry approaches allowed to define some structure-activity relationships, but failed to identify compounds with improved potency toward FAAH [26]. Therefore, in collaboration with the groups of Prof. V. Onnis and Prof. C. J. Fowler, we undertook a multidisciplinary study of the mechanism of action of Flu-AM1 and Ibu-AM5. In particular, we were interested in understanding the molecular basis of the inhibition kinetics of these compounds. Indeed, different molecular mechanisms may result in a mixed type inhibition. The experimental findings that closely related ibuprofen amide derivatives might show different inhibition kinetics (Ibu-AM5 *vs.* Ibu-AM14) prompted us to investigate, with an approach including computational methods, enzymology, chemical synthesis and mutant expression, the hypothesis that the mixed inhibition showed by Ibu-AM5 and Flu-AM1 were due to the capability to interact with two distinct binding site with different affinity.

In this context, computational methods offer unique opportunities to investigate the mutual structural rearrangements induced by ligand binding in the complex. We used an approach including a combination of molecular docking, molecular dynamics (MD) simulations and free energy methods. Hence, the study of the dynamical process of the formation of ligand-target complex would provide a molecular rationale for the design of more potent NSAIDs derivatives with FAAH/COX dual activity. Therefore, in order to design more potent FAAH inhibitors we investigated the binding mode of NSAIDs and related compounds, since little was known about the nature of interactions of these compounds with FAAH, or to the role of chirality in binding affinity. According with the inhibition kinetics, we started our analysis of the binding mode from the known competitive binding site, and we explored FAAH structure to search for potential allosteric binding sites.

Eventually, since MD simulations render a series of structural ensembles, clustered based on structural similarities, we also used methods for the

evaluation of the free energy of the system in order to select the more favourable binding mode.

Taken together these approaches will be used to analyse dynamical conformations of the complex induced by the ligand with the goal of discovering structural insight that might be useful to design novel FAAH/COX inhibitors.

3. Experimental section

Direct interactions between compounds and FAAH were investigated combining molecular docking studies with MD simulations. The simulations were performed on the rFAAH with deprotonated Lys142, as proposed for the catalytic mechanism [30]. A preliminary validation of the computational protocol, was performed by reproducing the experimentally determined binding mode of the pyrrolopyridine inhibitor found in the crystal structure 3QK5, which showed reliability of the procedure not only to reproduce the ligand binding, but also the position of key water molecules within the active site.

3.1 Molecular docking

Rigid docking calculations were performed using the software Autodock 4.2 [60]. The 3D structures of compounds were generated with pymol. Docking was performed on a single monomer of rat FAAH (PDB code 3QK5) [61], after crystallized ligand removal. Rigid docking in the competitive binding site was performed using a cubic docking box of 60^3 grid points, centred on the position of the original ligand (3-((3R)-1-[4-(1-benzothiophen-2-yl)pyrimidin-2-yl]piperidin-3-yl)-2-methyl-1H-pyrrolo[2,3-b]pyridin-1-yl)acetonitrile. The grid for the rigid docking in the allosteric site was centred on the basis of the result of cavity screening on mouse and rat FAAH in a pocket between CP and the interface between FAAH monomers and the maximum size of the axes were set to 54 grid points. The rotatable bonds of the compound were automatically detected by Autodock default parameters. For each docking run, 100 iterations were performed using default parameters of Lamarckian genetic algorithm (GALS). The results were clustered on the basis of RMSD criterion (≤ 4 Å). The representative poses of the best clusters, according to Autodock 4.2 score, of each system were used for further analysis.

3.2 Molecular Dynamics

MD simulations were performed to refine best docking results with Amber12 [62]. To this end, the representative poses of the best clusters retrieved from docking calculations were loaded in the two monomers of the dimeric form of rat FAAH (PDB code 3QK5), after removal of the pyrrolopyridine derivative and water molecules.

Each complex was immersed in a pre-equilibrated octahedral box of TIP3P water molecules, and the system was neutralized. The final systems contained

about 80000 atoms. All simulations were performed with the Amber 99SBildn force field [63] for the protein and the gaff force field [64] for the ligands. The charge distribution of the inhibitors was refined using RESP charges [65] fitted to the B3LYP/6-31G(d) electrostatic potential obtained with Gaussian09 [66]. For each complex the geometry was minimized using convergence criterion for the energy gradient set to $0.01 \text{ kcal/mol}\cdot\text{\AA}^2$ in three steps, which involve: i) hydrogen atoms in the system (5000 steps of steepest descent and 10000 steps of conjugate gradient), ii) hydrogen atoms, water molecules and counterions (2000 steps of steepest descent and 18000 steps of conjugate gradient), iii) finally the whole system (2000 steps of steepest descent and 18000 steps of conjugate gradient). Thermalization of the system was performed in four steps of 60 ps, increasing the temperature from 50 to 298 K. Concomitantly, the atoms that define the protein backbone were restrained during thermalization using a variable restraining force. Thus, a force constant of $30 \text{ kcal/mol}\cdot\text{\AA}^2$ was used in the first stage of the thermalization and was subsequently decreased by increments of $5 \text{ kcal/mol}\cdot\text{\AA}^2$ in the next stages. Then, an additional step of 250 ps was performed in order to equilibrate the system density at constant pressure (1 bar) and temperature (298 K). Finally, an extended trajectory was run using a time step of 2 fs. SHAKE was used for those bonds containing hydrogen atoms in conjunction with periodic boundary conditions at constant pressure and temperature, particle mesh Ewald for the treatment of long range electrostatic interactions, and a cutoff of 10 \AA for non-bonded interactions. The structural analysis was performed using in-house software and standard codes of Amber 12.

A preliminary validation of the computational protocol was obtained by predicting the experimentally determined binding mode of the pyrrolopyridine derivative in the 3QK5 crystal structure. The non-covalent ligand of the X-ray structure was chosen as reference due to higher structural similarity toward our compounds with respect to carprofen. It is worth noting that computational procedure successfully reproduced the binding mode of the pyrrolopyridine inhibitor, as well as the distribution of water molecules around the ligand in the binding cavity.

3.3 Free energies calculations

Analysis of the MD trajectory was carried out by calculating MM/GBSA, MM/PBSA and SIE on a 0.1 ns interval at the end of the trajectories. QM/MM calculations were performed for a set of 50 snapshots taken on a 0.1 ns interval along the last 5 ns of the trajectories, averaging the electrostatic and van der Waals components of the individual snapshots.

3.3.1 MM/PBSA method

The MM/PBSA method was used to calculate the free energies of molecules in solution including those related to protein-ligand binding, which enables

analysis of the stabilities of different patterns of interactions in protein-ligand complex formation [67]. We used open source AmberTools package (MMPBSA.py) [68] to perform binding free energy calculations. The energy constituents included molecular mechanics (MM), electrostatic contributions to solvation (PB), and nonpolar contributions to solvation (SA). The binding free energy for protein-ligand complexes was calculated based on the following equation (1) [68]:

$$\Delta G_{binding} = \Delta G_{complex} - \Delta G_{protein} - \Delta G_{ligand} \quad (1)$$

where $\Delta G_{complex}$ represents the free energy of a ligand-protein complex, and $\Delta G_{protein}$ and ΔG_{ligand} are the free energies of protein and ligand, respectively.

The vacuum-potential energy, $E_{Molecular-Mechanics}$, includes the energies of both bonded and non-bonded interactions and is calculated based on the molecular mechanics force field parameters [69], as shown in eq. 2:

$$E_{Molecular-Mechanics} = E_{bonded} + E_{non-bonded} \quad (2)$$

where $E_{Molecular-Mechanics}$ represents the gas-phase energy, E_{bonded} represents bonding interactions consisting of the bond, angle, dihedral, and improper interactions. Non-bonded interactions, $E_{non-bonded}$, include both electrostatic and van der Waals interactions.

In the MM/PBSA approach, the solvation free energy was calculated using an implicit-solvent model. The solvation free energy is given by the eq. 3:

$$\Delta G_{solvation} = \Delta G_{Polar} + \Delta G_{Non-Polar} \quad (3)$$

where, ΔG_{Polar} and $\Delta G_{Non-polar}$ are the electrostatic and non-electrostatic contributions to the solvation free energy, respectively. The electrostatic term, ΔG_{Polar} , is estimated by solving the Poisson–Boltzmann (PB) equation. The non-polar solvation energy, $\Delta G_{Non-Polar}$ is separated into attractive (dispersion) and repulsive (cavity) interactions.

3.3.2 SIE method

Sietraj is an alternative to the MM/PBSA software provided by the AMBER distribution. Solvated interaction energies (SIE) are calculated using parameters that have been fitted to reproduce binding free energies of a data set of 99 protein-ligand complexes [70]. Note that the underlying physics behind the electrostatic components of SIE and MM/PBSA is the same. Hence, all the caveats of implicit solvation apply. The main differences lie in the choice of parameters, surface generation method [71] and Poisson solver [72].

3.3.3 QM/MM calculations

The contribution due to the formation of the ligand-protein complex in the gas phase was determined by QM/MM calculations. To this end, the ligand was

treated at the QM level and all the residues located at less than 15 Å of the ligand were treated classically. Accordingly, the electrostatic term accounts for the QM interaction (determined at the B3LYP/6-311+G(d,p) level) of the ligand with the set of point charges of the residues included in the MM region. The van der Waals term was determined using the 6-12 expression as implemented in AMBER. The contribution due to the solvation of the complexes (ΔG_{sol}) was calculated by MM/GBSA and MM/PBSA methods.

3.3.4 Thermodynamic integration

The A1-mode binding of TPA5 in monomer A of rFAAH was used as starting structure for the free energy calculation using TI. The TI simulations of the alchemical transformation from TPA5 into TPA27 was separated into two parts: ligand transformation within the protein active site (ΔG_{bound}) and ligand transformation in solvent (ΔG_{free}). The binding free energy difference between these two similar ligands [$\Delta\Delta G_{(A\rightarrow B)}$] can be calculated from eq. (4):

$$\Delta\Delta G_{(A\rightarrow B)} = \Delta G_{\text{bindB}} - \Delta G_{\text{bindA}} - \Delta G_{\text{bound}} - \Delta G_{\text{free}} \quad (4)$$

We have performed one-step TI, since the van der Waals and electrostatic transformation of the unique regions between ligands A and B both occur in the same step. The simultaneous electrostatic and van der Waals transformation events in the one-step TI could result in high system instabilities, which is overcome in this study by activating both Lennard-Jones (eq. 5) and Coulomb Softcore potentials (eq. 6) simultaneously [73].

$$V_{\text{softcore}\epsilon\text{vanderWaals}} = 4\epsilon(1 - \lambda) \left[\frac{1}{\left[\alpha\lambda + \left(\frac{r_{ab}}{\sigma} \right)^6 \right]^2} - \frac{1}{\left[\alpha\lambda + \left(\frac{r_{ab}}{\sigma} \right)^6 \right]} \right] \quad (5)$$

Softcore potential in van der Waals is activated to avoid any instability as atoms appear and disappear, where λ is a coupling parameter, r_{ab} is the atomic distance between two particles, ϵ is the Lennard-Jones potential well depth, σ is the distance where the two particles intermolecular potential is equal to zero, and α is the Lennard-Jones Softcore potential energy function curvature control parameter, which has previously been recommended to be $\alpha = 0.5$ [73].

$$V_{\text{softcore}\epsilon\text{electrostatics}} = (1 - \lambda) \frac{q_a q_b}{4\pi\sqrt{\beta\lambda + r_{ab}^2}} \quad (6)$$

Electrostatic transformation is mediated by softcore potential, where q_a and q_b are electrostatic charges of transformed atoms in two ligands and β is the Coulomb Softcore potential energy function curvature control parameter, which has previously been recommended to be $\beta = 12 \text{ \AA}^2$ [73].

In the ΔG_{bound} and ΔG_{free} steps, each step is divided into 9 windows with different coupling parameters (λ), where $\lambda = 0$ is the initial state and $\lambda = 1$ is

the final state. The energy in each step (ΔG) can be calculated using eq. (7) where the bracket represents the average of the potential energy of the studied system [$\sigma(\lambda)$] for the given λ value, which is calculated using the trapezoid integration method. The λ values in this study are taken from the Table 21.1 in the Amber reference manual [74].

Each window was subjected to a 1000-step steepest descent minimization to remove bad initial contacts and a 50 ps NPT heating run in which the system temperature was raised to 298 K with a target pressure of 1 bar. Equilibration was followed by a 5 ns NPT simulation for data collection. Therefore, TI simulation required at least 90 ns MD simulation, since it include 2 transformations of 9 windows. Therefore, TI calculations are a very expensive computational method.

The following equation (7) was used to derive the MD simulation settings for each window.

$$\Delta G = \int_0^1 \left(\frac{\partial V(\lambda)}{\partial \lambda} \right) \partial \lambda \quad (7)$$

3.4 Homology building

The amino acid sequence of mouse FAAH was retrieved from the Universal Protein Resource database (<http://www.uniprot.org> accession ID O08914). The 3D structure of the target protein was modelled using SWISSMODEL [75]. The X-ray determined structure of rat FAAH 3QK5 was used as template (covered sequence 100%; sequence identity of 91.7 %).

4. Inhibition of FAAH by the enantiomers of Flu-AM1 and Ibu-AM5

4.1 Introduction

Ibu-AM5 and Flu-AM1 are valuable leads for the design of novel dual inhibitors of FAAH and COX enzymes, due to their pharmacological profile. Both compounds, that are profens derivatives, retain a chiral centre as the parent compounds, but it is not known how this affects their ability to inhibit FAAH. Previously reported studies [56, 76-78]. Demonstrated pronounced enantioselectivity towards inhibition of FAAH of some classes of inhibitors. In consequence, we have faced the study of the interaction between the enantiomers of Ibu-AM5, Flu-AM1 and FAAH through a multidisciplinary approach including biochemical, molecular biological and molecular modelling methodologies.

The results of this study have been already published in a peer-reviewed journal article [79] and is the result of an international collaboration including pharmacology and enzymology experiments (J. Karlsson, M. Svensson and C. J. Fowler of University of Umea, Sweden,), chemical synthesis (A. Deplano, C. Congiu and V. Onnis of University of Cagliari, Italy), mutant protein expression (G. Smaldone and E. Pedone of CNR, Naples, Italy) and computational methods (C. M. Morgillo, F. J. Luque, E. Novellino and B. Catalanotti of University of Naples Federico II, Italy).

4.2 Pharmacological studies

The interaction of the enantiomers of Flu-AM1 and Ibu-AM5 with rFAAH have been extensively investigated by the group of Prof. Fowler in order to determine the main features that characterise the binding mode and to explain the importance of the chiral centre in ligand binding. As showed in Fig. 7, the experiments of FAAH inhibition in rat brain proved the relevance of the chiral centre, since Ibufenac-AM1, which lacks the methyl group on the C-2 carbon atom and hence the chiral centre of Ibu-AM5, was a weak inhibitor of rat brain FAAH ($IC_{50} = 68 \mu M$).

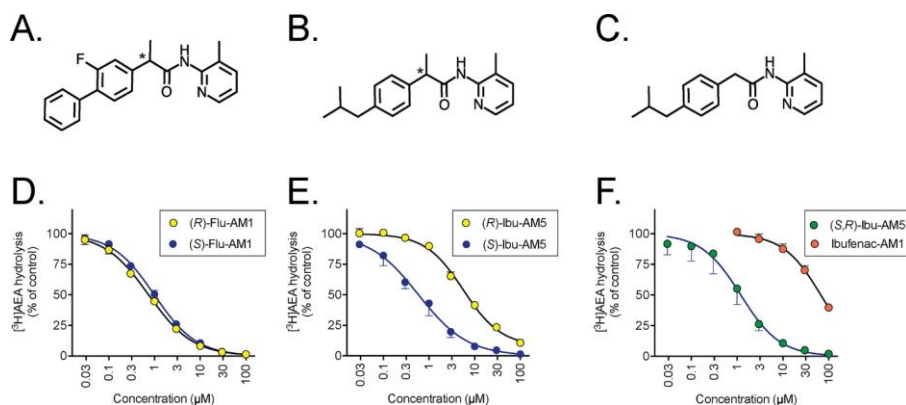


Fig. 7: Inhibition of FAAH by the enantiomers of Ibu-AM5 and Flu-AM1 and by Ibufenac-AM1. Structures of the compounds are shown in panels A-C: A, Flu-AM1; B, Ibu-AM5; C, Ibufenac-AM1. The asterisks show the chiral centres. In panels D-F, the inhibition of 0.5 μM [3H]AEA hydrolysis in rat brain homogenates by the compounds is shown. Data are means ± SEM (when not enclosed by the symbols), N = 3 for the enantiomers of D, Flu-AM1; E, Ibu-AM5 and F, racemic Ibu-AM5 and Ibufenac-AM1.

Inhibition experiments evidenced different behaviour between enantiomers of Flu-AM1 and Ibu-AM5. (*R*)-Flu-AM1 was marginally more potent FAAH inhibitor than the corresponding (*S*)-enantiomer (IC₅₀ values of 0.74 and 0.99 μM, respectively). In contrast, the (*R*)-enantiomer of Ibu-AM5 was 10-fold less potent than the (*S*)-enantiomer (IC₅₀ values of 5.7 and 0.59 μM, respectively). In order to investigate the diversity in the behaviour of the enantiomers of Flu-AM1 and Ibu-AM5, molecular modelling was undertaken using both docking and MD simulations.

4.3 Validation of the computational protocol

We have performed a preliminary validation of the whole computational protocol, including rigid docking and 50 ns MD simulations by reproducing the experimentally determined binding mode of the pyrrolopyridine derivative in the crystal structure 3QK5. Among the experimental determined structures of the rFAAH inhibitors only carprofen and pyrrolopyridine derivative were reported on the PDB server. We have chosen pyrrolopyridine derivative as a validation system because of the structural similarity with Flu-AM1 and Ibu-AM5, while carprofen was less suitable due to the smaller size (18 heavy atoms vs. 25 of Flu-AM1 or 22 of Ibu-AM5), and especially to the negative charge, while our compounds are neutral.

The docking was performed without water, albeit water is likely involved in the binding of the pyrrolopyridine derivative. In the validation study, we found that the protocol used was able not only to reproduce the ligand binding, but also the water position within the active site (Fig. 8).

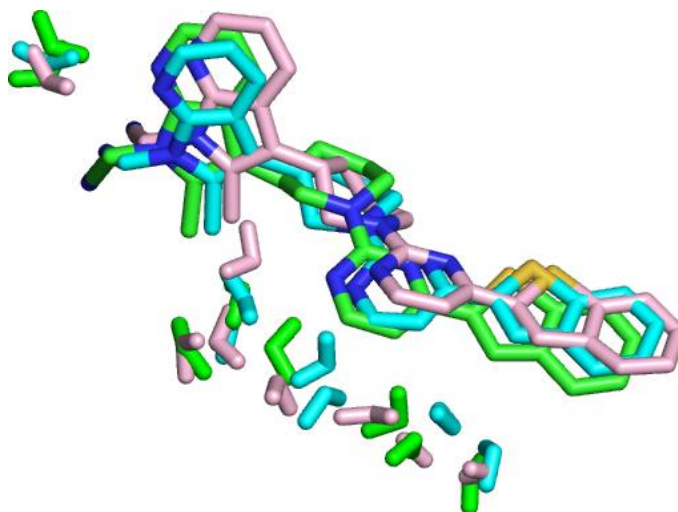


Fig. 8: Comparison of the position of the pyrrolopyridine inhibitor and water molecules in the crystal structure 3QK5 (green), in the docking result (yellow), in the best cluster obtained after 50 ns in the monomer A (cyan) and in the best cluster obtained after 50 ns MD in the monomer B (pink). Superimposition was made on protein backbone.

4.4 Molecular docking of the enantiomers of Flu-AM1 and Ibu-AM5

The binding mode of the enantiomeric forms of Flu-AM1 and Ibu-AM5 to rFAAH enzyme was studied combining docking studies and MD simulations. Docking was performed with the software Autodock 4.2 [60], which was successful in predicting the binding mode of non-covalent ligands (see experimental section §3.1). The ligand poses were ranked considering the cluster population and the binding energy. The results showed that the ligand bind to a region formed by the ABP channel and the MAC, filling the cavity experimentally found for other non-covalent ligands [39, 61]. Two binding modes that differ in the orientation of the amide moiety were found (Fig. 9). Thus, the amide moiety points towards either the catalytic triad (A-mode) or the membrane interacting helices $\alpha 18$ - $\alpha 19$ (B-mode). The B-mode was found to be the most populated cluster for the two enantiomers, but the scores of A- and B-modes were highly similar, thus preventing a firm distinction between the ligand orientations (Table 1).

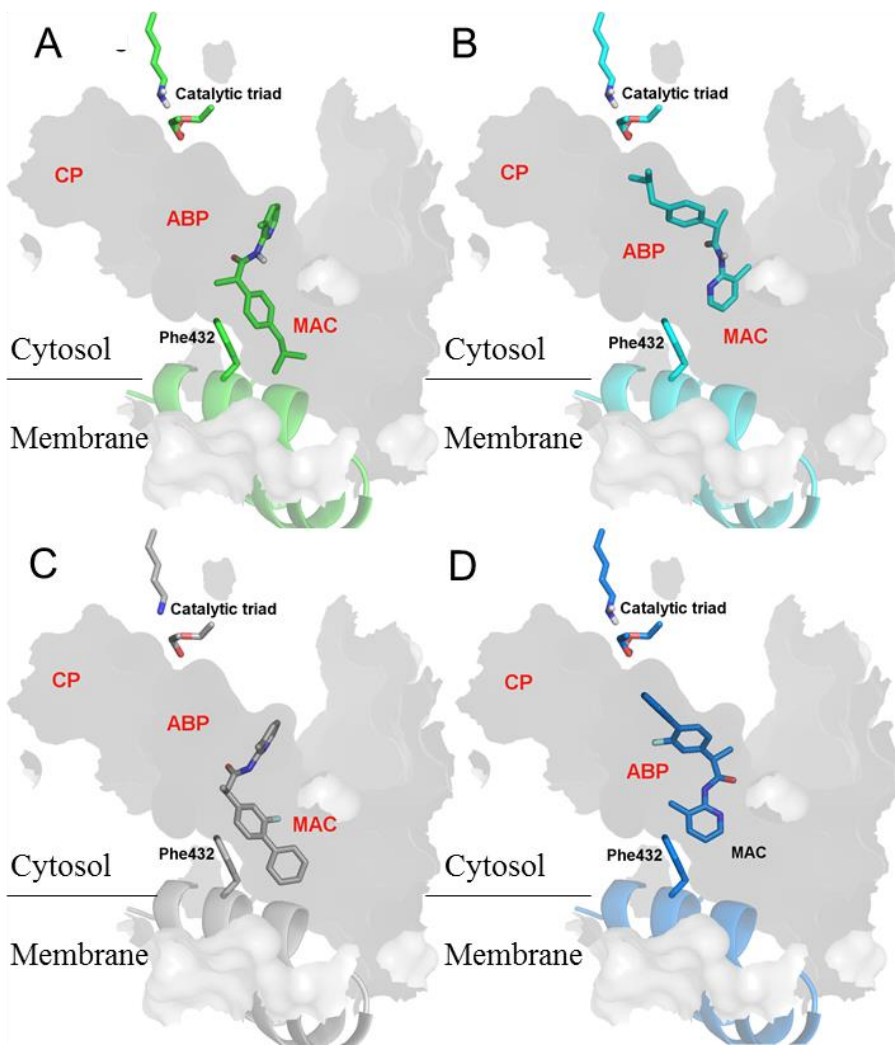


Fig. 9: Molecular docking of (*S*)-Ibu-AM5 and (*R*)-Flu-AM1 in the competitive site of FAAH. Structures of the compounds are shown in relation to their localization in the channels of FAAH: A, A-mode of (*S*)-Ibu-AM5; B, B-mode of (*S*)-Ibu-AM5; C, A-mode of (*R*)-Flu-AM1; D, B-mode of (*R*)-Flu-AM1.

Compound	Docking		
	Mode	Popn (%)	AD score ^a
(R)-FluAM5	A	11	-9.02
	B	47	-9.22
(S)-FluAM1	A	11	-9.22
	B	43	-9.21
(S)-Ibu-AM5	A	9	- 8.59
	B	70	- 8.45
(R)-Ibu-AM5	A	14	-8.45
	B	57	-8.46

Table 1: Docking results of the enantiomers of Ibu-AM5 and Flu-AM1 predicted by the software Autodock 4.2. ^a Predicted binding energy of the best pose in the relative cluster family.

4.5 Molecular dynamics studies of the enantiomers of Flu-AM1 and Ibu-AM5

To further check structural integrity of two binding modes, the best poses of each docking cluster were submitted to 50 ns MD simulation. Two independent MD simulations were run on the FAAH dimer, thus enabling loading the same docking pose in each monomer, affording four complexes for each enantiomeric species.

As a general trend, the simulations starting from the B-mode remained stable along the whole trajectory, whilst the ligand showed significant rearrangements when the simulation started from the A-mode. The simulation started from the B-mode of (*R*)-Flu-AM1 remained stable along the whole trajectory, as noted in the lack of significant alterations in the positional root-mean square-deviation (RMSD) for the ligand after an initial stabilization (Fig. 10). In contrast, simulations started from the A-mode showed a continuous rearrangement and larger fluctuations were observed for the ligand (Fig. 10A).

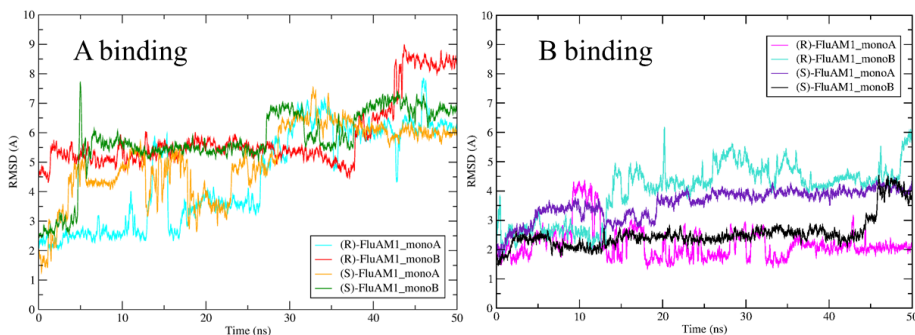


Fig. 10: Time evolution (ns) of the RMSD (Å) of the (*R*)- and (*S*)-Flu-AM1 enantiomers in the MD run starting from A-mode best poses (left), and MD run starting from B-mode best poses (right).

The B-mode binding led to a consistent pattern of interactions in the binding pocket, whereas the A-mode exhibited less consensus in the interactions between ligand and protein. As an additional test, an independent MD simulation was run for (*R*)-Flu-AM1 bound to FAAH dimer starting from the B-mode binding, and the results confirmed the structural integrity of the ligand arrangement. Indeed, three out of the four complexes converged to a common binding mode, which is characterized by the presence of a hydrogen bond between the hydroxyl group of Thr488 and the carbonyl unit of the (*R*)-enantiomer, as noted in the similar arrangement obtained upon superimposition of representative snapshots of MD (Fig. 11). Based on these results we have chosen B-mode binding as putative binding for further analysis.

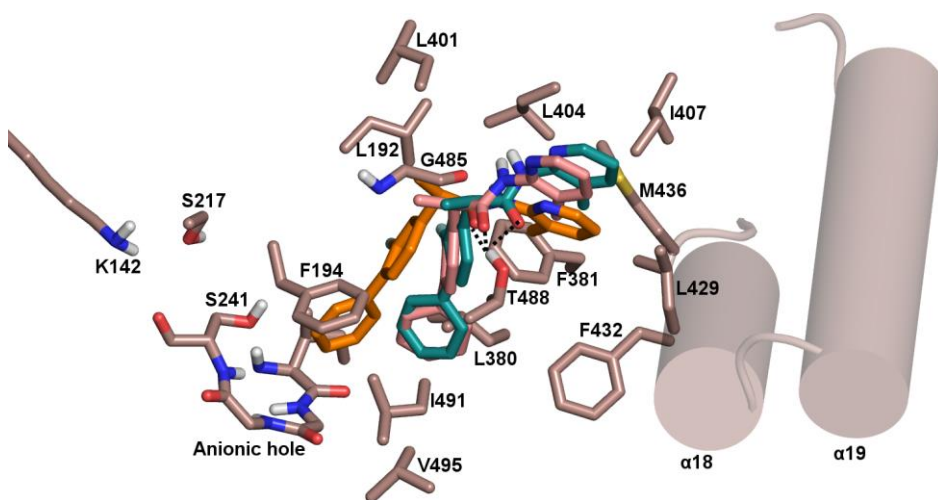


Fig. 11: Superposition of representative snapshots taken from the two MD runs of (*R*)-Flu-AM1 bound to monomer A (protein in marron, ligand in orange and pink) and monomer B (dark cyan).

The ligand (*R*)-Flu-AM1 is closely packed in the binding site (Fig. 12A), forming interactions that are preserved along most of the trajectory. The biphenyl moiety fills a hydrophobic cavity, with the distal ring pointing to the centre of the anionic hole and forming van der Waals contacts with hydrophobic residues lining the ABP channel: Ile491 (at 4.0 Å), Phe381 (at 4.1 Å) and Leu380 (at 4.0 Å) Ile238 (at 3.8 Å). The fluorinated ring shows contacts with the methyl group of Thr488 (at 4.1 Å) and with Phe194 (at 3.7 Å). The fluorine atom shows a constant distance from aromatic hydrogen of the Phe381 (average 3.3 Å). No specific interactions of the methyl group on the chiral centre were observed. On the other side, transient hydrogen bonds were observed between the pyridine nitrogen and the backbone of Asp403, or, alternatively Gly485 (through a water molecule), and between the amide NH

unit and the backbone of Leu401. Van der Waals contacts are observed with side chains of Met436 and Ile407. The structural integrity of this binding mode was maintained upon extension of the trajectory up to 100 ns.

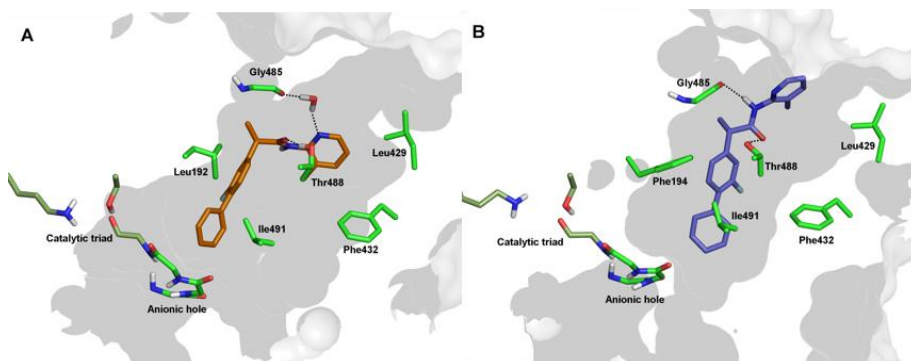


Fig. 12: Representation of (*R*)-Flu-AM1 (A) and (*S*)-Flu-AM1 (B) in the competitive binding site of the dimeric FAAH as obtained from MD simulations.

The MD trajectories run for (*S*)-Flu-AM1 led to similar poses in the two monomers of FAAH (Fig. 12B). The results showed that the amide bond establishes stable hydrogen bonds between the amide NH unit and the backbone of Gly485, and between the amide carbonyl with the Thr488 sidechain. Moreover, the terminal phenyl ring formed van der Waals contacts with Leu192, Val495 and Ile491 (at 3.9-4.3 Å), and the fluorinated ring was close to Phe381, Leu401, Phe432 and the methyl ring of Thr488. The methyl group on the chiral carbon pointed towards Leu404 (at 3.9 Å) and Leu401 (at 4.5 Å).

Comparison of (*R*)- and (*S*)-Flu-AM1 binding modes is shown in Fig. 12, which highlights how the enantiomers were bound in slightly different arrangements in the same site located between ABP and MAC channels. Nevertheless, the enantiomers showed a very similar pattern of interactions: i) the aromatic rings formed a number of van der Waals contacts mainly involving aliphatic side chains, ii) the fluorine atom weakly interacted with Phe381, and iii) the amidopyridine moiety established hydrogen-bonds with Gly485 and Thr488.

MD simulations of (*S*)-Ibu-AM5 B-mode converged to similar binding modes in the two monomers of FAAH, while no convergence was observed for the A-mode. Extension of the MD to 100 ns confirmed the stability of the B-mode, which remained stable for the last 70 ns of the simulation. (*S*)-Ibu-AM5 binds the bottom of the ABP channel and the MAC (Fig. 13A) with the pyridine nitrogen fitting the position of the carprofen carboxylic group (PDB code 4DO3). The pyridine ring is firmly packed in a hydrophobic residues at the gorge of the MAC, interacting with Trp531 (at 3.6 Å), Leu429 (at 3.9 Å), and Ile407 (at 4.0 Å from the methyl group). The amide unit of the ligand formed hydrogen bonds with the backbone carbonyl of Gly485 and to the

Thr488 side chain. The profen moiety is placed in the apolar gorge of the ABP with the methyl group on the chiral carbon pointing toward Leu404 (at 4.2 Å) and Leu401 (at 4.2 Å). The phenyl ring is packed between Phe194 (at 3.9 Å) and Phe432 (4.2 Å) while the isobutyl group formed van der Waals contacts only with Ile238 (at 4.2 Å) and Ile491 (at 3.9 Å).

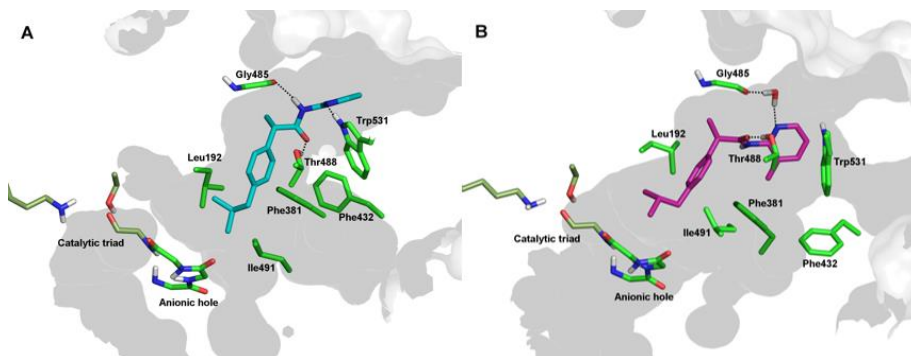


Fig. 13: Representation of (*S*)-Ibu-AM5 (A) and (*R*)-Ibu-AM5 (B) in the competitive binding site of the dimeric FAAH as obtained from MD simulations.

Simulations run for (*R*)-Ibu-AM5 also supported the B-mode binding, leading to similar ligand arrangements in the two monomers. Compared to the (*S*)-enantiomer, most of the differences arise from the interactions established by the amidopyridine moiety, since a hydrogen-bond was formed between the carbonyl unit of the amide group and the hydroxyl group of Thr488 and the pyridine nitrogen formed a water-mediated contact with Gly485, in addition to hydrophobic contacts with Trp531 (at 4.0 Å), Ile407 (at 4.3 Å), and Phe381 (at 4.0 Å from the methyl).

4.6 Comparison of the binding mode of the enantiomers of Flu-AM1 and Ibu-AM5

The comparison of the best representative poses of (*R*)- and (*S*)-Flu-AM1 showed very different binding modes for the two enantiomers, with the (*S*)-enantiomer binding deeper in the MAC. The same behaviour was observed from the MD simulations of (*R*)- and (*S*)-Ibu-AM5 (Fig. 14), suggesting that chirality is a main determinant of the binding mode.

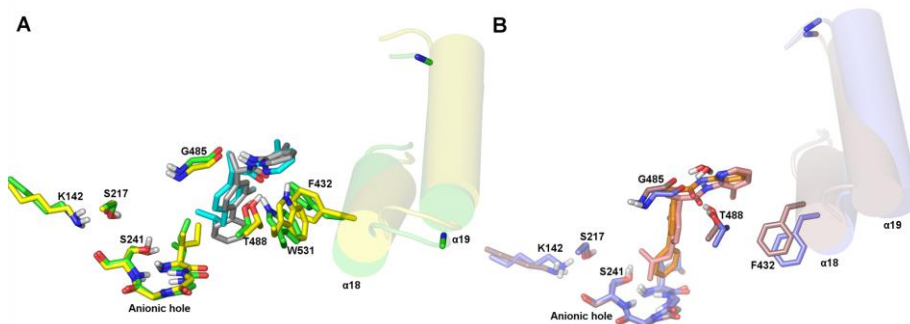


Fig. 14: Superimposition of the binding mode proposed for (*S*)-enantiomers (A) and (*R*)-enantiomers (B) in the competitive binding pocket of FAAH.

Interestingly, this behaviour seems to be associated to the conformational change of Phe432. In the MD trajectories of (*S*)-enantiomers the Phe432 χ_1 dihedral switched from $\sim 90^\circ$ to $\sim 180^\circ$, allowing the packing of the methylpyridine in a hydrophobic cavity formed by Trp531, Leu429 and Ile407. The same Phe432 rotamer ($\chi_1 = \sim 180^\circ$) was found in the crystal structure of rFAAH bound to anandamide analogue (PDB code 1MT5), while in the binding mode of (*R*)-enantiomers the Phe432 assume the same conformation found in 3QK5 and 4DO3 crystal structures ($\chi_1 = \sim 90^\circ$). Nevertheless, enzymatic activity showed that these differences in the binding mode slightly affected the activity of Flu-AM1 enantiomers, while it has more remarkable effect on the Ibu-AM5 enantiomers. The binding modes of (*R*)- and (*S*)-Flu-AM1, albeit different, resulted comparable, being characterized by a similar pattern of hydrophobic interactions and two hydrogen bonds, which is in agreement with the similar activities showed by these enantiomers. On the contrary, the (*S*)-Ibu-AM5 binding mode resulted more stable in the light of the higher number of hydrogen bonds.

4.7 Comparison with other non-covalent FAAH inhibitors

These results suggested that Flu-AM1 and Ibu-AM5 bind a region located between ABP channel and the entrance of the MAC, overlapping the binding of other non-covalent FAAH inhibitors, such as carprofen (PDB code 4DO3) and the pyrrolopyridine derivative in the 3QK5 crystal structure. Among the two possible binding mode found in docking studies, MD simulations showed that only the B-mode shows a relevant interaction with Thr488. The finding that (*R*)-Flu-AM1 is a less potent inhibitor of the FAAH^{T488A} mutated variant relative to the wild-type enzyme supported this conclusion, as showed also for carprofen inhibition assays (Fig. 15).

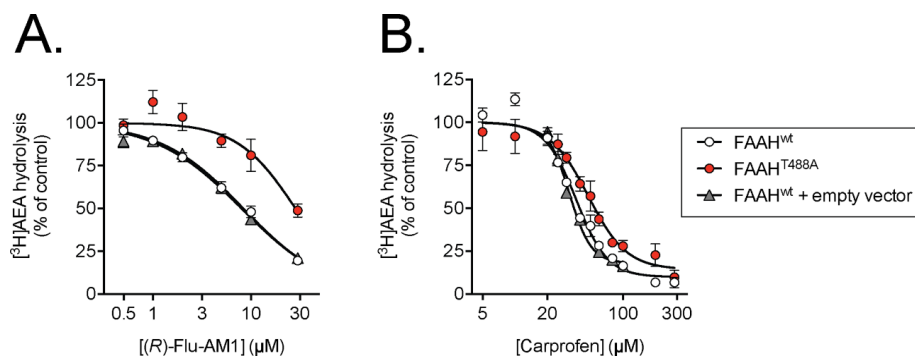


Fig. 15: Inhibition of rat wild-type and FAAH^{T488A} by (R)-Flu-AM1 (A) and carprofen (B).

The binding mode of these compounds agrees with biochemical experiments, since multiple inhibition experiments with carprofen and assays on mutated FAAH^{T488A} enzyme suggest that these inhibitors inhibit FAAH in a mutually exclusive manner. In fact, comparison between the proposed binding mode for (R)-Flu-AM1, (S)-Ibu-AM5, and the binding pose in the crystal structure of carprofen and pyrrolopyridine derivative, highlights a similar pattern of interaction with FAAH and especially the presence of a hydrogen bond with the sidechain of Thr488 (Fig. 16).

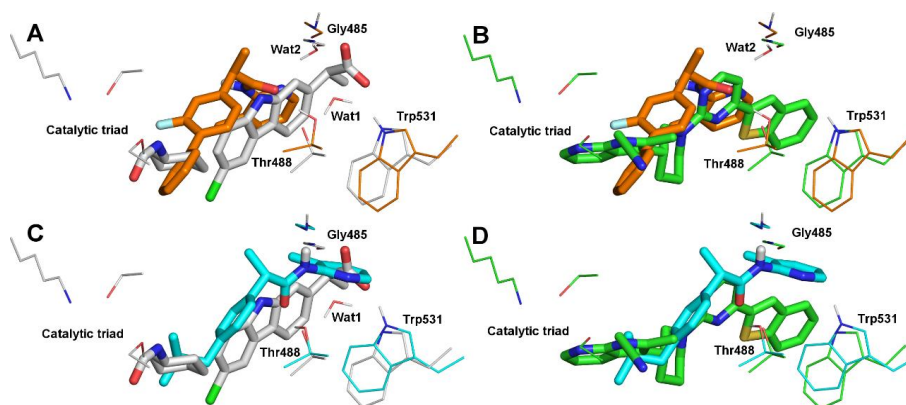


Fig. 16: Comparison of the binding modes of (R)-Flu-AM1, (S)-Ibu-AM5, carprofen and the pyrrolopyridine derivative. (A) (R)-Flu-AM1 (orange) compared to carprofen (white; PDB ID: 4DO3); (B) (R)-Flu-AM1 (orange) compared to pyrrolopyridine derivative (green; PDB ID: 3QK5); (C) (S)-Ibu-AM5 (cyan) compared to carprofen (white); (D) (S)-Ibu-AM5 (cyan) compared to pyrrolopyridine derivative (green). Alignment was obtained by superimposition of the protein backbone. For sake of clarity only polar Hydrogen were shown.

4.8 Guidelines for drug design

The above discussion has only considered a single binding site for the compounds. However, the kinetic experiments suggested a mixed-type of inhibition. This mechanism implies that these compounds should bind to two mutually exclusive sites [80]. Therefore, it is difficult to suggest

modifications to improve the activity of these compounds dealing with only one of the possible sites of action of these inhibitors. In fact, a series of substitutions has been attempted on the structure of Ibu-AM5 inhibitor with no success in improving the activity against FAAH [25, 26, 58]. As a result of the binding mode investigated by computational methods, by two series of modification on different branches of the molecule have been simultaneously developed: i) modification of different scaffolds from ibuprofen and flurbiprofen structure, and ii) modification on the pyridine moiety would investigate interactions with FAAH through the polar branch of the compound.

5. Inhibition of FAAH by 2-(4-((2-(Trifluoromethyl)Pyridin-4-yl)amino)phenyl)propan Amides (TPA)

5.1 Rational design of TPA derivatives and TPA5 pharmacological profile

The Ibu-am derivatives are characterized by the presence of the isobutyl chain of the parent ibuprofen. MD studies on the binding mode of Ibu-AM5 enantiomers, showed that in both (*S*)- and (*R*)-Ibu-AM5 the isobutyl chain fills a wide pocket within the ABP channel, allowing two main populated and opposite positions of the isobutyl chains (Fig. 17).

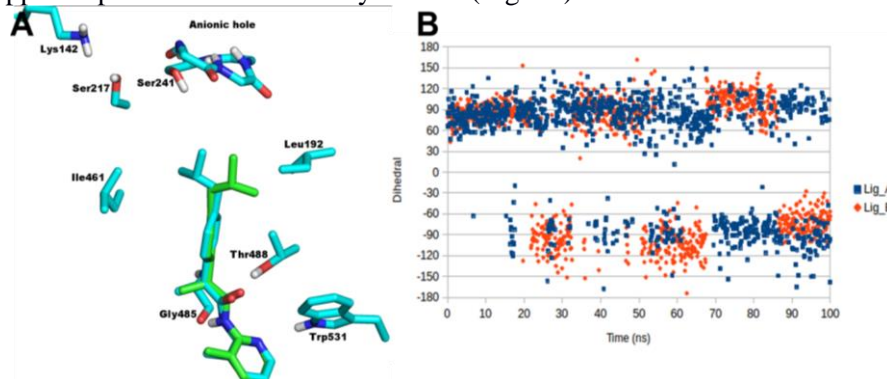


Fig. 17: Isobutyl moiety flexibility during MD of Ibu-AM5. A) Two subsequent snapshots of the MD run of (*S*)-Ibu-AM5. The ligand is shown in green and cyan sticks, while the surrounding residues are labeled and shown in cyan sticks. B) Time evolution of the dihedral angle of isobutyl moiety during MD of the ligand in monomer A (blue) and in monomer B (orange).

With the aim to modulate the lipophilicity of the compounds and achieve a tighter binding, we explored the possibility to substitute the isobutyl group of Ibu-AM5 with 4-((2-(Trifluoromethyl)Pyridin-4-yl)amino) group, obtaining a new series of profen derivatives synthesized by the group of Prof V. Onnis and tested by the group of Prof C. J. Fowler: 2-(4-((2-(Trifluoromethyl)Pyridin-4-yl)amino)phenyl)propanAmides (TPA) (Fig. 18).

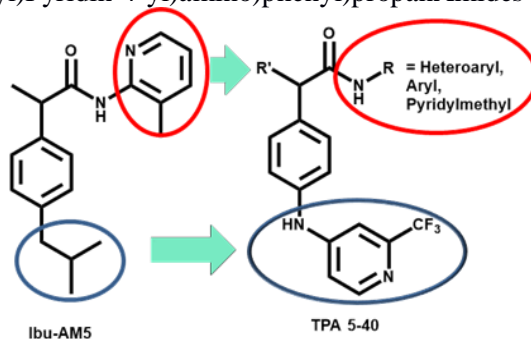


Fig. 18: Design strategy starting from Ibu-AM5 to TPA.

Replacing iso-butyl group of Ibu-AM5 with a trifluoromethylpyridinylamino moiety led to TPA5, which maintains the FAAH inhibitory activity (IC_{50} value = $0.59 \mu\text{M}$). The kinetics of TPA5 binding was also examined to gain insight into the mechanism of action of this novel class of FAAH inhibitors. TPA5 resulted a competitive inhibitor (Fig. 19, B1), showing little dependency upon preincubation time, which suggests a reversible inhibition (Fig. 19, A1).

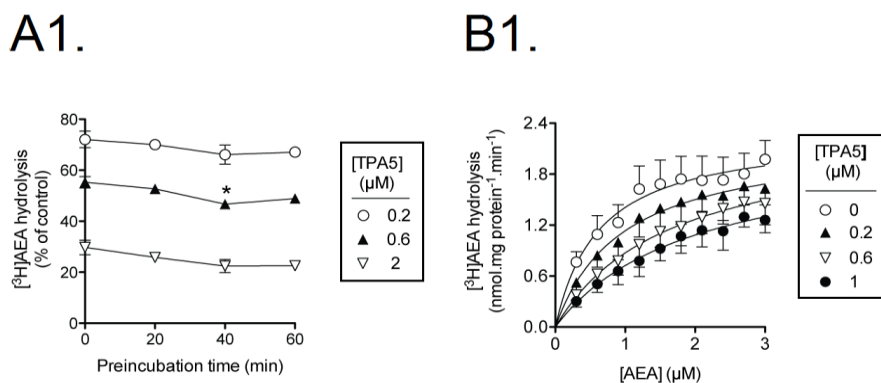


Fig. 19: Mode of inhibition of rat brain FAAH by TPA5. Panel A: homogenates were preincubated with the compounds for the times shown prior to addition of $0.5 \mu\text{M}$ [^3H]AEA and assay for FAAH activity (means and s.e.m., $n=3-4$) Panel B: AEA hydrolysis at the substrate and inhibitor concentrations shown (means and s.e.m, $n=3$).

Taking into account the competitive mechanism of TPA5, we studied its binding mode by using the docking and MD protocol previously described for enantiomers of Flu-AM1 and Ibu-AM5 (see §4.3). Given that (*S*)-Ibu-AM5 is 10-fold more potent than (*R*)-Ibu-AM5 as inhibitor of FAAH, while the (*S*)-Flu-AM1 enantiomer is almost as equipotent as the more active (*R*)-enantiomer, we used the (*S*)-enantiomer for computational studies on the TPA derivatives.

5.2 Molecular docking of TPA5

Docking was performed in the competitive site of the enzyme, adopting the same approach used for the enantiomers of Flu-AM1 and Ibu-AM5 (see §4.4). The results showed that the ligand binds a region formed by the ABP channel in proximity to the catalytic triad, but adopting up to four different arrangements (Table 2).

Mode	AD score (kcal/mol)	Popn (%)
A1	-9,11	50
B1	-9,01	30
B2	-8,67	9
A2	-8,66	3

Table 2: Docking results for TPA5 predicted by Autodock 4.2

The binding modes differed in the orientation and positioning of the molecule along the channels, having the amide moiety pointing towards the cytosolic port (A1-mode), the catalytic triad (A2-mode), the membrane access channel (B1-mode) or the membrane interacting helices $\alpha 18$ - $\alpha 19$ (B2-mode) (Fig. 20).

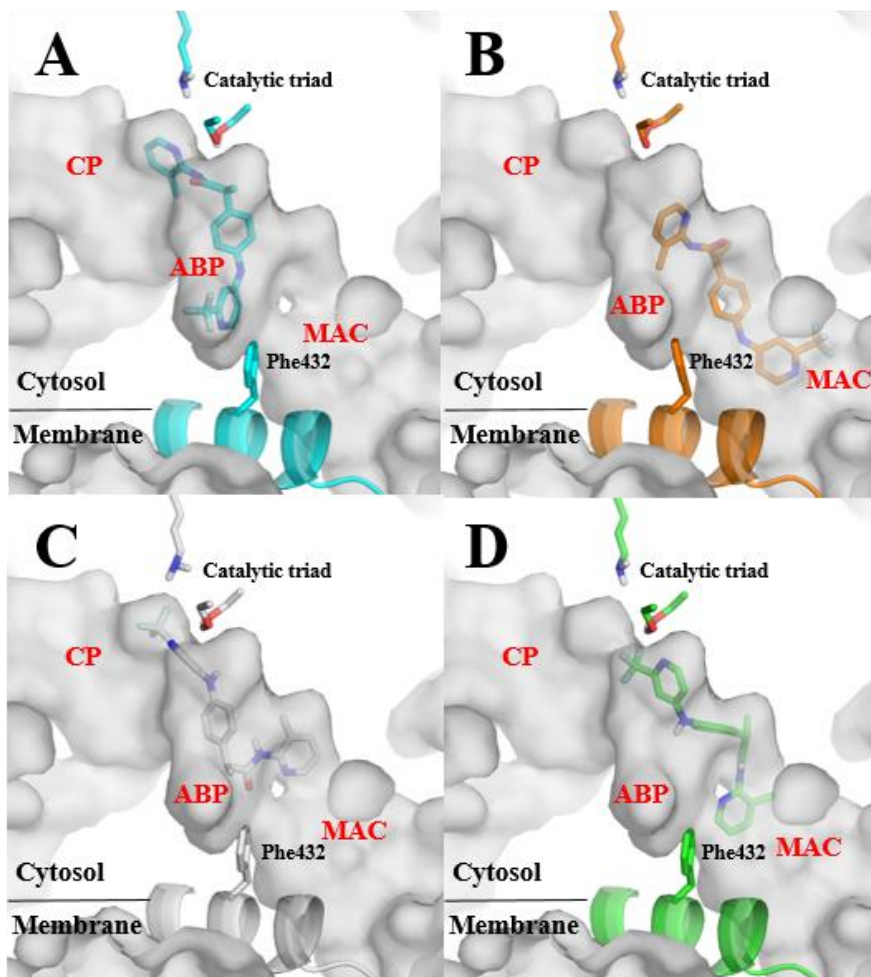


Fig. 20: Molecular docking of TPA5 in the competitive site of FAAH. Structures of the compounds are shown in relation to their localization in the channels of FAAH: A, A1-mode; B, A2-mode; C, B1-mode; D, B2-mode.

5.3 Molecular dynamics and free energies calculation of TPA5 in the competitive site

The A1-mode was found to be the most populated and energetically favoured cluster for TPA5, but we preserved also other binding modes for MD simulation analyses, due to their similarity to the binding modes found for the enantiomers of Ibu-AM5 and Flu-AM1.

The best pose for each binding mode was submitted to 100 ns MD simulations. Compared to the MD studies on the enantiomers of Ibu-AM5 and Flu-AM1, we have doubled the length of the simulation time to perform more exhaustive analysis on the stability of the four binding modes found for

TPA5. The calculations were performed on the dimeric form of the enzyme loading the docking pose on both monomers, while analyses were performed on the single monomers.

The A1-mode was found to be very stable during 100 ns of MD, as showed in the RMSD plot of the ligand (Fig. 21A), and the convergence to the same binding mode in the two monomers (Fig. 21B).

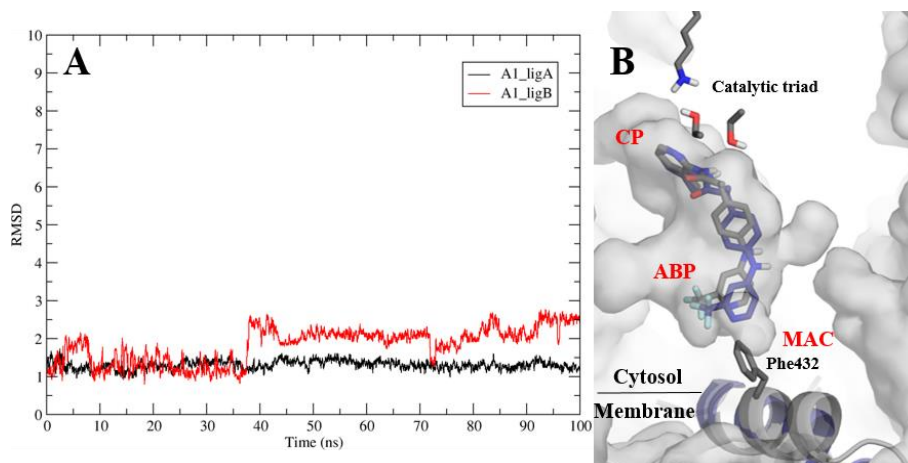


Fig. 21: MD refinement of TPA5 A1-mode. A: RMSD plot during 100 ns of MD refinement of the ligand in monomer A (black) and monomer B (red). B: superimposition of the competitive binding site refinement at the end of 100 ns of MD in monomer A (grey) and monomer B (indigo).

The MD refinement of A1-mode led to a tight packed binding between the catalytic triad and the ABP channel, showing the high stability of the TPA5 conformation adopted during the trajectory. It is worth noting that this binding mode influences the arrangements of the residues in the MAC channel, leading to the closure of the entrance gate for the FAAH substrates.

The A2-mode showed little differences in the binding of TPA5 in the two monomers. As observed in the RMSD plot, the ligand in monomer B showed a net conformational change after 75 ns, corresponding to the switch of the torsional of the trifluoromethyl-pyridin moiety (Fig. 22A), while the other parts of the ligand bind in a stable manner to the ABP channel (Fig. 22B).

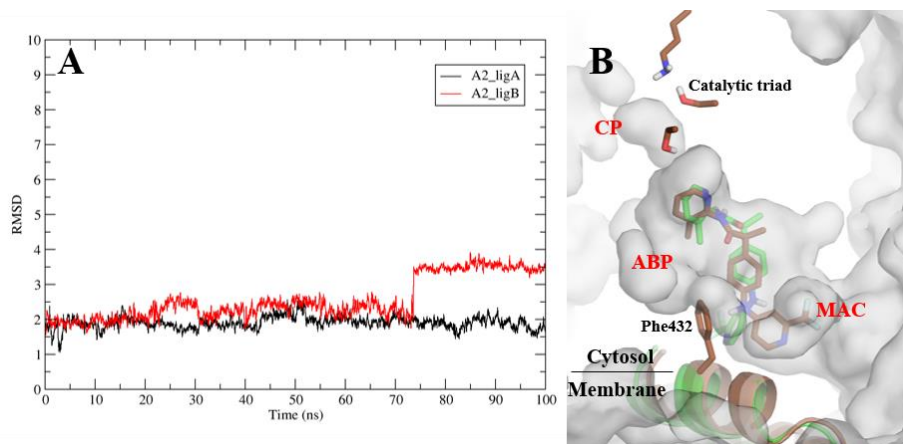


Fig. 22: MD refinement of TPA5 A2-mode. A: RMSD plot during 100 ns of MD refinement of the ligand in monomer A (black) and monomer B (red). B: superimposition of the competitive binding site refinement at the end of 100 ns of MD in monomer A (brown) and monomer B (green).

The B1-mode showed a quick rearrangement of TPA5, reflected in the RMSD plot of the ligand in the monomers A and B, which show a firm fluctuation in the initial phase of MD refinement (Fig. 23A). Cluster analysis of the ligand in the two monomers led to a similar binding mode with different orientations of the methyl-pyridine moiety in the MAC channel (Fig. 23B).

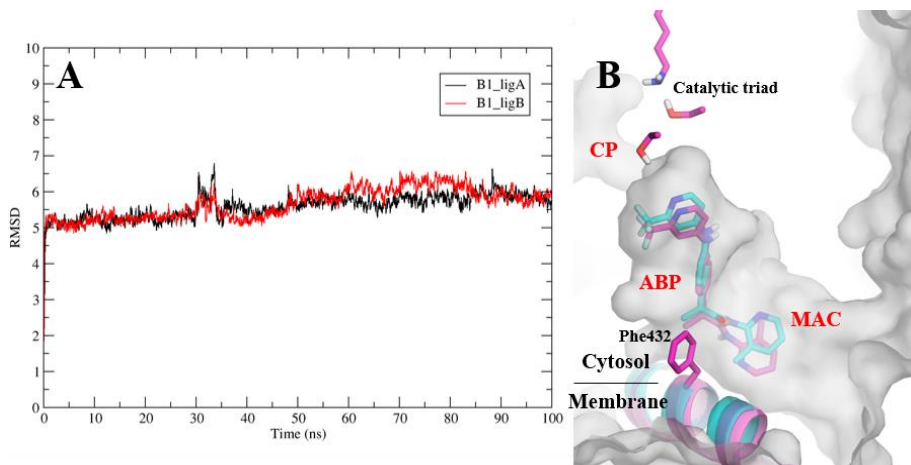


Fig. 23: MD refinement of TPA5 A1-mode. A: RMSD plot during 100 ns of MD refinement of the ligand in monomer A (black) and monomer B (red). B: superimposition of the competitive binding site refinement at the end of 100 ns of MD in monomer A (cyan) and monomer B (magenta).

The B2-mode showed very distinct binding modes in the two monomers. As seen in the RMSD plot, the ligand in the monomer A showed large fluctuation and binds a region between ABP and MAC channels (Fig. 24A). Moreover, the different positioning of the ligand in the two monomers influenced the

arrangement of the surrounding residues, as seen for $\alpha 18$ and $\alpha 19$ helices (Fig. 24B).

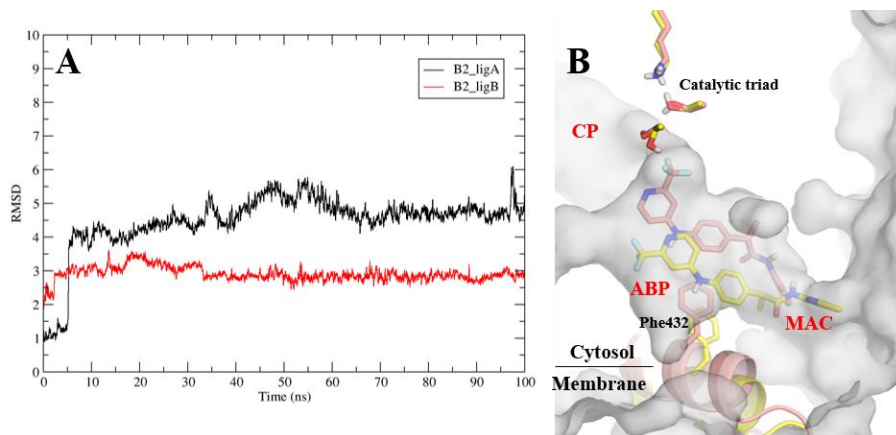


Fig. 24: MD refinement of TPA5 A1-mode. A: RMSD plot during 100 ns of MD refinement of the ligand in monomer A (black) and monomer B (red). B: superimposition of the competitive binding site refinement at the end of 100 ns of MD in monomer A (yellow) and monomer B (pink).

To discriminate among the conformational ensembles sampled for each binding mode in the MD refinement, the binding free energies were determined using three approaches: Molecular Mechanics Generalized Born Surface Area (MM/GBSA) and Molecular Mechanics Poisson Boltzmann Surface Area (MM/PBSA) and Solvated Interaction Energy (SIE) (see Experimental Section for details of the underlying formalisms). As said before, only A1-mode was found to converge to the same binding mode in the two monomers A and B, while other bindings led to distinct conformational ensembles for each monomer (Fig. 21B-24B). Both MMPBSA, MMGBSA and SIE calculations supported the preference for the A1-binding mode of TPA5 (Table 3).

ligand	DOCKING				MD analysis					
	mode	Pop%	AD score	MMGBSA	cl	Pop%	Time (ns)	MMGBSA	MMPBSA	SIE
TPA5	A1	50	-9,11	-59,46	a0	97,8	95-100	-58,47	-15,76	-10,2
					b0	96,2	95-100	-48,04	-2,46	-9,29
	A2	30	-8,41	-49,65	a0	38,6	95-100	-48,64	5,26	-9,39
					b0	66,7	95-100	-45,79	3,03	-8,91
	B1	9	-9,01	-49,18	a0	75,1	95-100	-48,23	-2,65	-9,13
					b0	94,5	95-100	-42,41	3,00	-8,62
	B2	3	-8,67	-50,68	a0	48,7	95-100	-47,63	1,13	-9,29
					b0					

Table 3: Free energy calculation of the representative binding modes refined through MD runs of 100 ns. In case of non-convergent binding mode, the evaluation of free energies of binding are reported for the best cluster in the monomer A (a0) and B (b0). MMPBSA, MMGBSA and SIE values are in kcal/mol.

Docking scores, MD convergence and estimation of binding affinity strongly indicated the A1-binding mode as the preferred pose. Nevertheless, taking into account that very similar compounds, such as Flu-AM1 and Ibu-AM5, showed binding modes comparable to the B2-mode, we opted for a more robust method to further assess the preference of the A1-binding mode for TPA5. Indeed, hybrid quantum mechanical molecular mechanics (QM/MM) calculations were submitted for each representative binding mode. Being QM/MM computationally more expensive method, we restricted these calculations to the residues surrounding a subset of 15 Å from the centre of mass of the binding modes refined by MD to avoid any loss of the interactions that might influence the binding affinities. The QM/MM results confirmed the previous free binding energies calculations (Table 4).

mode	QM/MM	$\Delta G_{\text{solv(GB)}}$	$\Delta G_{\text{solv(PB)}}$	$\Delta G_{\text{tot(GB)}}$	$\Delta G_{\text{tot(PB)}}$
A1	-89,89	21,47	65,57	-68,42	-24,32
A2	-67,32	13,46	58,91	-53,86	-8,41
B1	-71,93	20,71	62,43	-51,22	-9,5
B2	-76,55	19,79	66,76	-56,76	-9,79

Table 4: QM/MM results on the binding modes for TPA5. QM/MM scores were obtained on the dry complexes, therefore solvation energies from GBSA and PBSA calculations were added to obtain final values of binding energies.

The analysis of the more representative snapshot of the A1-mode (Fig. 25) showed that TPA5 binds through a series of hydrogen bonds and prevalently by hydrophobic interactions with the apolar gorge of ABP (Fig. 25). In particular, the methyl-pyridine moiety is in the proximity of the catalytic triad, tightly packed by apolar interactions with residues Met191, Leu192, Ile228, Val270 and Leu278 (Fig. 25B). The carbonyl oxygen of the amide resides permanently near the anionic hole formed by the main chains of residues Ile238, Gly239, Gly240 and Ser241, while the NH group forms a stable hydrogen bond with the backbone of Met191. The interactions of the amide group and of the methyl-pyridine ring required the adoption of a specific conformation, which seems therefore to be a key requisite for FAAH inhibition for this class of compounds. Further apolar interactions of the aromatic groups with residues along the channel, and a water-bridged H-bond of aromatic and the backbone of Leu192 contribute to stabilize the binding (Fig. 25A).

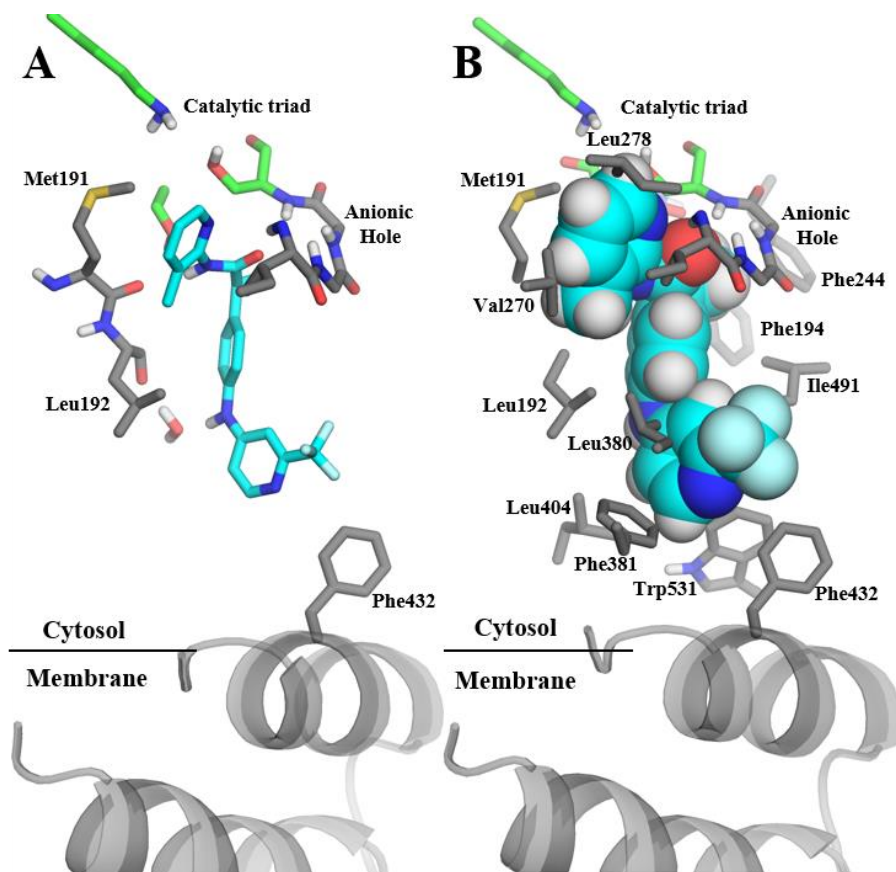


Fig. 25: A1-mode of TPA5 refined after 100 ns of MD. A) Hydrogen bond of TPA5 (cyan, in sticks) in A1-mode. B) Apolar interaction in the binding pocket of the FAAH. The ligand TPA5 is represented in cyan by van der Waals spheres.

5.4 Structure Activity Relationships of TPA derivatives

A series of substitutions were designed on the TPA5 structure with the aim to explore the structure-activity relationships of the ligand in the binding pocket. Substitutions on the methyl-pyridine amide moiety, which allows more flexibility to this region, as the introduction of a methylene linker (TPA8, TPA9), as well as the linker extension through an additional amide moiety (TPA10), caused a decrease in activity (Table 5). According to the selected binding mode A1, these modifications avoid the positioning of the methyl-pyridine ring in the pocket defined by residues Met191, Leu192, Ile228, Val270 and Leu278.

Compound	Formula	Max inhibition (%)	IC ₅₀ (μM)
TPA5		100	0.59
TPA8		100	23.0
TPA9		100	32.0
TPA10		100	2.4

Table 5: Maximum percentage and IC₅₀ values for inhibition of rat brain AEA hydrolysis by compounds TPA5, TPA8-10.

Similarly, we can explain the drop of activity showed by derivatives bearing different position of the methyl group on the pyridine ring (TPA11, TPA12) (Table 6) or lacking the methyl in position 5 on the methyl-pyridine ring, such as TPA13 (Table 6), TPA14 and TPA15 (Table 7) and in a lesser extend TPA18 (Table 7). The methyl group plays a key role in the conformational behaviour of TPA5, determining the relative positioning of the methyl-pyridine ring with respect to the amide bond, besides the specific apolar interactions formed by the methyl group with side chains of Val270 and Leu192.

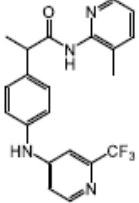
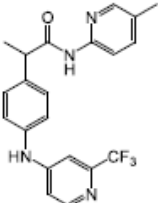
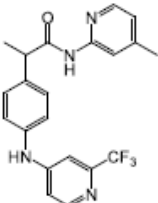
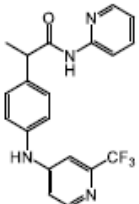
Compound	Formula	Max inhibition (%)	IC ₅₀ (μM)
TPA5		100	0.59
TPA11		68±4	11.0
TPA12		100	4.0
TPA13		93±3	12.0

Table 6: Maximum percentage and IC₅₀ values for inhibition of rat brain AEA hydrolysis by compounds TPA5, TPA11-13.

Moreover, the position of nitrogen on the methyl-pyridine ring is not implicated in direct polar interaction in the binding mode presented for TPA5. In fact, the toluene analogue TPA16 showed similar activity in respect to TPA5, while analogues with different position of the nitrogen in the pyridine ring showed a decrease in activity (TPA14, TPA15, TPA17, TPA18). These data confirm the greater importance of the presence of the 3-methyl pyridine substituent than nitrogen atom position. Finally, the introduction of a larger and more lipophilic ring, like the 8-aminoquinoline group in TPA19, caused a reduction in activity (Table 7), indicating that there is no space to accommodate larger groups.

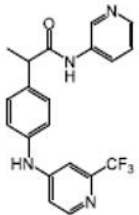
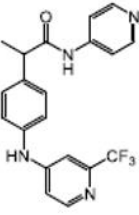
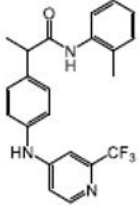
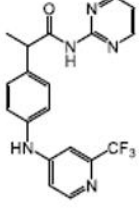
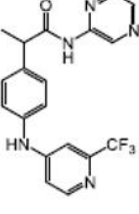
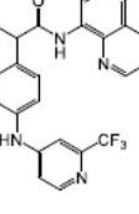
TPA14		86±2	6.4
TPA15		100	52.0
TPA16		100	0.74
TPA17		100	0.99
TPA18		100	2.0
TPA19		75±7	4.3

Table 7: Maximum percentage and IC₅₀ values for inhibition of rat brain AEA hydrolysis by compounds TPA14-19.

The inclusion or replacement of the methyl group in the pyridine ring by halogens (TPA24-27) increased the inhibitory activity. In particular,

substitution by chloride (TPA27) led to a 10-fold enhancement in inhibitory potency (Table 8). This group of derivatives presented relative small changes in structure compared to the lead TPA5. Hence, we focused our studies in understanding why the substitution of the methyl (TPA5) by chlorine (TPA27) increased the inhibitory activity.

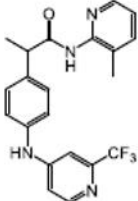
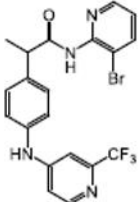
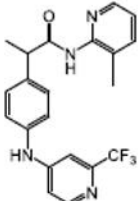
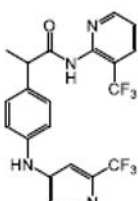
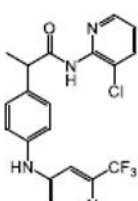
Compound	Formula	Max inhibition (%)	IC ₅₀ (μM)
TPA5		100	0.59
TPA24		100	0.13
TPA25		100	0.10
TPA26		100	0.33
TPA27		100	0.058

Table 8: Maximum percentage and IC₅₀ values for inhibition of rat brain AEA hydrolysis by compounds TPA5, TPA24-27.

The binding of TPA27 was further analysed by means of inhibition kinetics experiments in order to define the mechanism of action of this derivative. The

results showed that TPA27 (Fig. 26B), unlike TPA5, behaves as non-competitive inhibitor with K_i and α values of $0.28 \mu\text{M}$ and 1.03 , respectively. Since for pure non-competitive inhibitors α is expected to be 1, these results demonstrated that TPA27 is essentially non-competitive in its action. Moreover, preincubation and dilution experiments also demonstrated the reversibility of its action (Fig 26A).

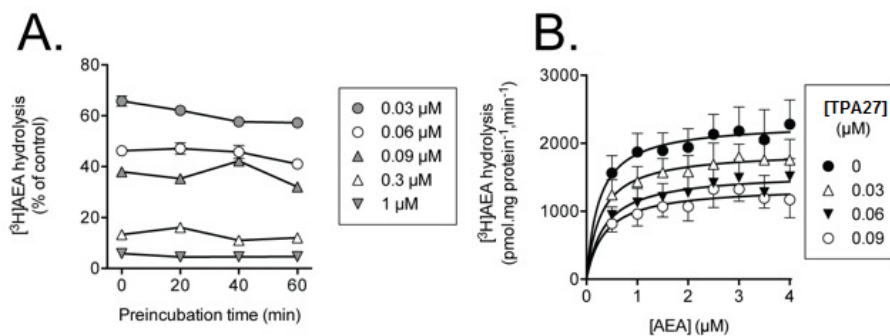


Fig. 26: Mode of inhibition of rat brain FAAH by TPA27. Panel A: homogenates were preincubated with the compounds for the times shown prior to addition of $0.5 \mu\text{M}$ $[^3\text{H}]\text{AEA}$ and assay for FAAH activity (means and s.e.m., $n=3-4$). Panel B: AEA hydrolysis at the substrate and inhibitor concentrations shown (means and s.e.m, $n=3$).

Taken into account these data, it may be assumed that TPA5 and TPA27 act as FAAH inhibitors interacting with two different binding sites in the enzyme. Therefore, kinetic experiments highlighted how small substitutions in the compounds belonging to the series of TPA derivatives, should dramatically affect the inhibition mechanism and binding preferences of these inhibitors. In light of such considerations, caution should be taken in order to derive the structure-activity relationships, since apparently minor structural modifications could influence not only the binding mode, but also the inhibition mechanism.

In order to analyse the molecular basis of these subtle effects, thermodynamic integration (TI) calculations [81] were used to calculate the differences in binding free energy between TPA5 and TPA27. TI is best used in situations where small changes in structure correlate with relatively substantial changes in the binding affinity. Therefore, TI was used to specifically address to the role of substitution of the methyl group on the pyridine ring in TPA5 with the chlorine group in TPA27, performing the alchemical mutation from TPA5 to TPA27 in the selected binding mode of TPA5 (A1-mode). The calculation yielded a free energy difference of 0.3 kcal/mol , thus indicating a slightly higher affinity of TPA5 with respect to TPA27, whereas the experimental data indicated that TPA27 was 10-fold more potent inhibitor than TPA5. In our view, this is indirect evidence that TPA27 could not bind the enzyme mimicking the competitive binding mode of TPA5, as the estimated change in binding affinity is opposite to the experimental evidence. Indeed, this finding

would agree with the experimental finding that TPA27 follows essentially a non-competitive inhibition mechanism.

5.5 Comparison with other FAAH inhibitors

Our results suggest that TPA5 binds a region located between the catalytic triad and the MAC, overlapping the binding of the anandamide analogue MAFP (PDB code 1MT5) and consequently, overlapping the binding mode of the series of α -ketoheterocycle covalent FAAH inhibitors [41, 42, 45, 46]. In fact, the superimposition of the X-ray structure of MAFP with TPA5 highlights how the ligand adopts a conformation to bind the FAAH that matches well the structure of MAFP, although this latter compounds binds even deeper in the MAC (Fig. 27A). A similar behaviour is observed by the superimposition with three different compounds of the series of α -ketoheterocycle covalent FAAH (Fig. 27B-D). In particular, the carbonyl moiety of the two compounds fills the same position, pointing towards the anionic hole, while the nitrogen on the pyridine ring of TPA5 overlaps the nitrogen in the oxazole moiety (Fig. 27D).

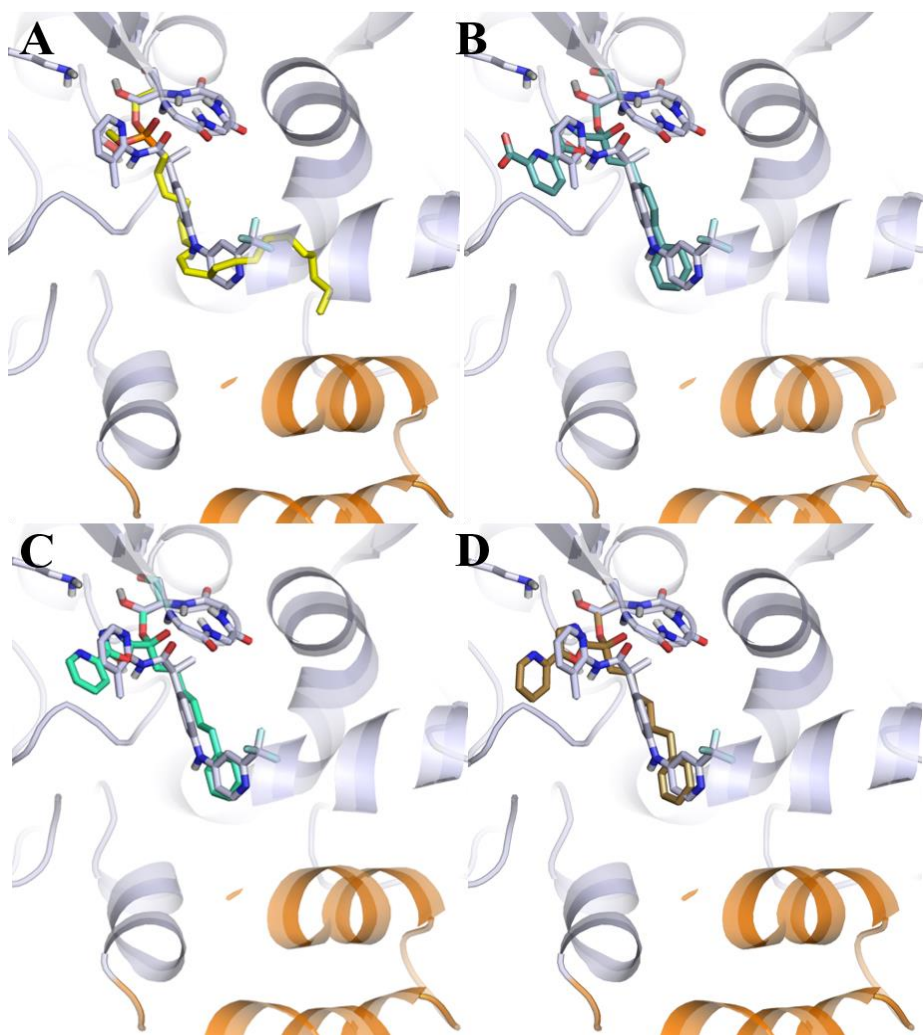


Fig. 27: Superimposition of the binding mode of TPA5 (grey sticks) with X-ray structure of anandamide analogue MAFP (A: pdb code 1MT5, yellow sticks), and series of α -ketoheterocycle covalent FAAH inhibitors (B: pdb code 3K83, aquamarine sticks; C: pdb code 3PRO, light green sticks; D: pdb code 2WJ2, tan sticks). Catalytic triad and anionic hole are represented in sticks, helices $\alpha 18$ - $\alpha 19$ are represented in orange cartoon.

6. Structural investigation of the allosteric site in FAAH

The above discussion has only considered a single binding site for the compounds. However, the kinetic experiments performed by Prof. Fowler and co-workers at the University of Umea (Sweden) suggested a variety of mechanisms underlying the inhibitory activity (Table 9).

Compound	Rat				Mouse			
	IC ₅₀	Mode of inhibition	K _i	α	IC ₅₀	Mode of inhibition	K _i	α
Ibu-AM14	3.6	competitive	2.1	→∞ ^a				
TPA5	0.59	competitive	0.39	→∞ ^a	2.8	mixed	6.3	4.2
TPA27	0.058	Non-competitive	0.11	1 ^a	0.48	mixed	3.0	3.2
±Ibu-AM5	0.52							
S-IbuAM5	0.59	mixed	0.80	3.2	7			
R-IbuAM5	5.7	mixed	10	3.1	53			
±Flu-AM1	0.44	mixed	0.18	6.9				
S-FluAM1	0.99	mixed	0.79	5.6	11			
R-FluAM1	0.74	mixed	0.63	3.2	8.8	competitive	19	→∞ ^a

Table 9: Comparison of potencies (μM) and modes of inhibition for key compounds identified in this thesis: species dependency between rat and mouse FAAH. IC₅₀ values refer to the inhibition of the hydrolysis of 0.5 μM [³H]AEA by rat or mouse brain homogenates, as appropriate. K_i and α values were obtained using the enzyme kinetics inhibition curve fitting algorithms available in the GraphPad Prism programme. Under settings “weightings” and “replicates” in the programme, “no weighting” and “only consider the mean Y value of each point” were used. Only data using ≥8 substrate concentrations has been included here. Comparisons of different models: competitive, non-competitive, mixed-type inhibition were undertaken and the best fit was chosen by Akaike’s informative criteria. ^aThese values of α are by definition for the competitive or non-competitive inhibition.

In the rat brain homogenates, Ibu-AM14 [26] and TPA5 inhibited [³H]AEA hydrolysis in a competitive manner, whereas TPA27 was a non-competitive inhibitor. Ibu-AM5 and Flu-AM1 enantiomers were mixed-type inhibitors of rat brain [³H]AEA hydrolysis. In contrast, in mouse brain homogenates, both TPA5 and TPA27 were mixed-type inhibitors, whereas (*R*)-Flu-AM1 was competitive in nature. A mixed-type inhibition has been associated to an allosteric mode of inhibition, or to a non-competitive binding to the active site [82]. As an example of non-competitive binding to the active site, NSAIDs such as flurbiprofen (but not ibuprofen) interact with COX in a two-step reaction whereby an initial competitive interaction is followed by a slower tight-binding or even irreversible inhibition. However, in these cases, the time dependency is very marked, occurring over minutes [83]. In the present case, there was some apparent time-dependency with (*R*)-Flu-AM1 (Fig. 28A), but it was very slow, and we have previously not seen such time-dependency with racemic Flu-AM1, despite its mixed-type mode of inhibition [25]. Moreover, dilution experiments demonstrated the full reversibility of (*R*)-Flu-AM1 (Fig. 28C).

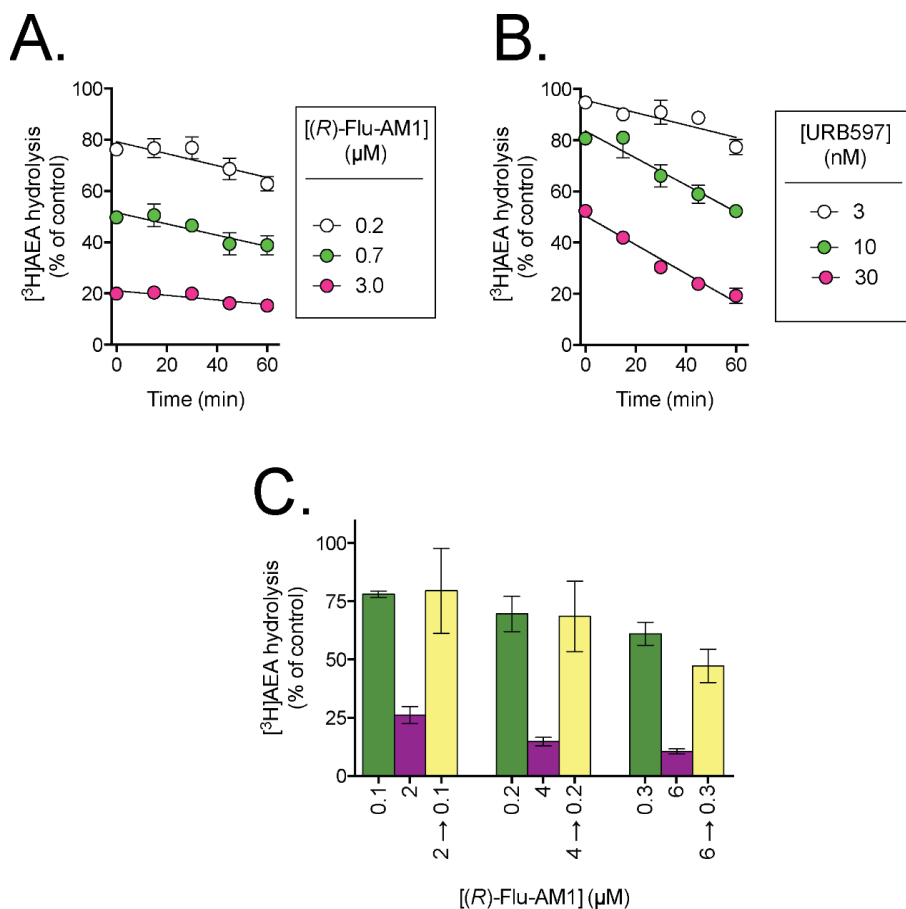


Fig. 28: Time-dependency and reversibility of the inhibition of rat brain FAAH by (*R*)-Flu-AM1. Panels A and B show the time-dependencies of (*R*)-Flu-AM1 and URB597, respectively. The data are means \pm SEM, $N = 3$. In Panel C, homogenates (at 20-fold normal strength) were preincubated with either vehicle, 2, 4 or 6 μM (*R*)-Flu-AM1 for 60 min. Aliquots were then diluted 20-fold and assayed for FAAH activity. These are shown as 2 \rightarrow 0.1, 4 \rightarrow 0.2 and 6 \rightarrow 0.3. Concomitantly, (*R*)-Flu-AM1 was added to vehicle-preincubated aliquots to give concentrations of 0.1, 0.2 and 0.3 μM (representing free concentrations after a 20-fold dilution), 2, 4 and 6 μM final concentrations. The panel shows the data as percentage of corresponding control (means \pm SEM, $N = 3$). For a fully reversible compound, the inhibition seen in the yellow bars (i.e. following the dilution) should be lower than in the purple bars (the inhibition seen at the undiluted concentrations) but equal to the green bars (the free concentrations after the dilution).

We thus do not favour this mechanism as an explanation for our data. A simpler mechanism for a fully reversible linear-mixed type inhibition of the amidic profen derivatives may involve binding to two mutually exclusive sites [80]. Such a model would be consistent with the data, and would represent a particular case of the mixed inhibition model shown in Fig. 29.

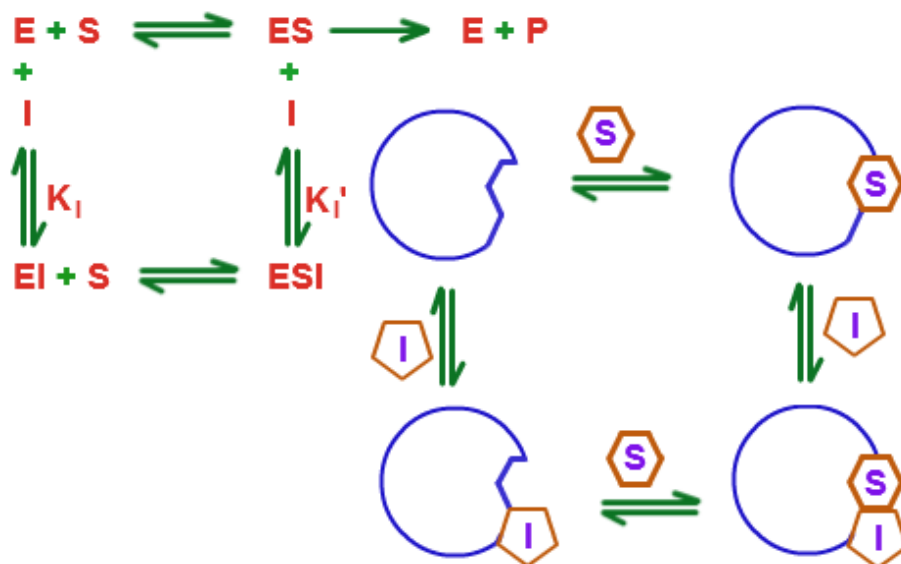


Fig. 29: Scheme of mixed-type inhibition

Indeed, we could speculate that mixed inhibition arise from comparable affinities toward the two binding sites, with weak preference for the competitive site (determined by α ; Table 9). Competitive inhibitors such as TPA5 would bind the non-competitive site with very little affinity, if any. Finally, the non-competitive mechanism of TPA27 could be explained by a marked binding preference for the non-competitive binding site, so that the binding to FAAH is not affected by the presence of the substrate. Structural differences in the competitive and non-competitive binding sites for rat and mouse FAAH could then give rise to the different observed modes of inhibition, and the lower potencies of the compounds, generally by one order of magnitude, in mouse FAAH compared to the rat enzyme. Similarly, small differences in structure would drive the affinity toward the two binding sites giving rise to different mode of inhibition.

In light of such considerations, we were prompted to search of an allosteric binding site for these compounds.

6.1 Pocket detection

A first step to harness the regulatory potential and versatility of allosteric sites would be to identify their presence and location. A sequence-based prediction approach proposes to use a multiple sequence alignment to identify networks of co-evolving residues in a protein family. Based solely on sequence, it would be very hard to predict the location of allosteric sites as it has been done by homology on active sites [84, 85], because the evolutionary pressure for sequence conservation on allosteric sites is generally much lower and

harder to detect, if at all present [86, 87]. Instead, a structure-based prediction approach identifies and ranks the druggable pockets in the 3D structure of the protein.

In order to detect an allosteric site on the FAAH enzyme, we have used fpocket webserver [88] to analyse the overall FAAH cavities in the 3D structure of rFAAH and mFAAH. The main goal of this approach is to discover druggable binding sites on FAAH able to be modulated by small-molecule interactions. We focused the analysis on the 10 best pockets scored by fpocket and compared the amino acidic sequence involved in the composition of the pockets between mouse and rat structures, with the aim to compare whether differences in the protein sequence may lead to different cavities in the enzyme (Table 10).

pocket	colour	Residue rFAAH	Mutation mFAAH
1	black	L192,F194,I238,S241,K263,V270,T274,Q277,Y335,L372,L380,G385,F388,L401,L404,V407,F431,R486,T488,G489,I491,V495,I530,I534 (A)	Y194,V407,M530 (A)
2	blue	T257,N259,K263,S264,G268,A275,L280,P310,L375,I451,Y454,R455,L500 (A) L192,T236,S262,K263,G268,V270,Y271,T274,Q277,L280,P310,L380,G385,F388,Q448,R455,Q456,I459,D501,P555 (B)	S268,V280 (A) S268,V280 (B)
3	green	L192,S193,F194,L372,L380,L401,L404,I407,F432,R486,T488,G489,I491,V495,I530 (B)	Y194,V407,M530 (B)
4	red	K46,S51,S116,Y117,H150,D151 (A)	G51,A151 (A)
5	cyan	K46,S51,S116,Y117,H150,D151 (B)	G51,A151 (B)
6	yellow	A460 (A) M162,C168,V169,T304,L305 (B)	V162,R304 (B)
7	orange	N159,C269,R386,S387,Q390,N391 (A) W445,K446,H449 (B)	C386 (A) E446 (B)
8	magenta	I251,R285,D286 (A)	-
9	pink	M162,S164,K267 (A)	V162 (A)
10	grey	K142,M191,S241 (B)	-

Table 10: Best 10 pockets ranked by fpocket webserver. Predictions were performed on FAAH dimer, thus the residue that define each pocket are specified by monomer in parenthesis. Residues are defined for the rat FAAH structure and the corresponding mutants are reported in mouse FAAH.

Analysis of the results revealed that the best three pockets were internal cavities, while pockets from 4 to 9 were located on the surface exposed to the solvent (Fig. 30).

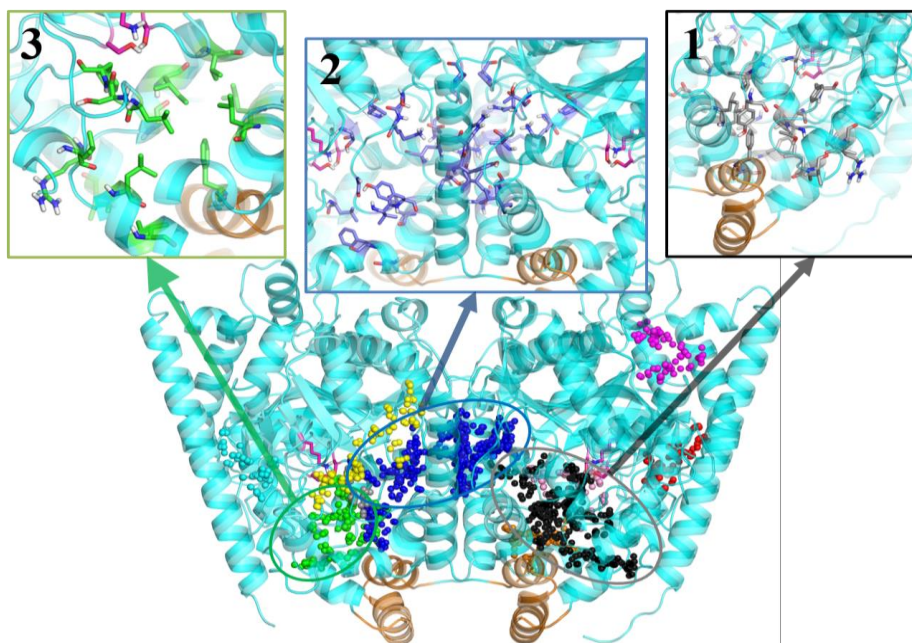


Fig. 30: Results of the pockets screened by fpocket webserver. Rat FAAH are represented by cyan cartoon with helices $\alpha18$ - $\alpha19$ highlighted in orange. Residues of the catalytic triad are represented by magenta sticks. Pockets are represented in spheres by colour code reported in the table below. Three best results of fpocket are highlighted on the top of the figure.

Moreover, we also found some asymmetric differences between monomers A and B of rFAAH. In fact, among the best ranked pockets, pocket 1 in monomer A (black spheres) is larger than the corresponding pocket in monomer B (pocket 3, green spheres), since pocket 1 includes residues classified as an independent pocket in monomer B (pocket 10, grey). Therefore, we found two druggable internal cavities in FAAH: i) (in black and green) the first cavity is located between the catalytic triad and the membrane interacting helices $\alpha18$ - $\alpha19$ and represents the pocket occupied by the substrate and hence is considered as the competitive pocket, and ii) (in blue) a second cavity is located in the cytosolic port that connects the catalytic triad to the cytosol, allowing the release of the ethanolamine produced by the hydrolysis of anandamide and the access of water needed to release arachidonic acid.

To further check the capability of all detected pockets to bind amide profen derivatives, we performed docking with Autodock4.2 on a box including all the pockets found with the previous pocket analysis. Docking was performed on Ibu-AM5, which is the smallest ligand that could bind an allosteric site. We performed 200 iterations with the aim to improve the search for potential binding sites enlarging the sampling.

Docking solutions were located between the pockets coloured in blue, green and grey as determined by fpocket (Fig. 31), excluding the implication of the external cavities.

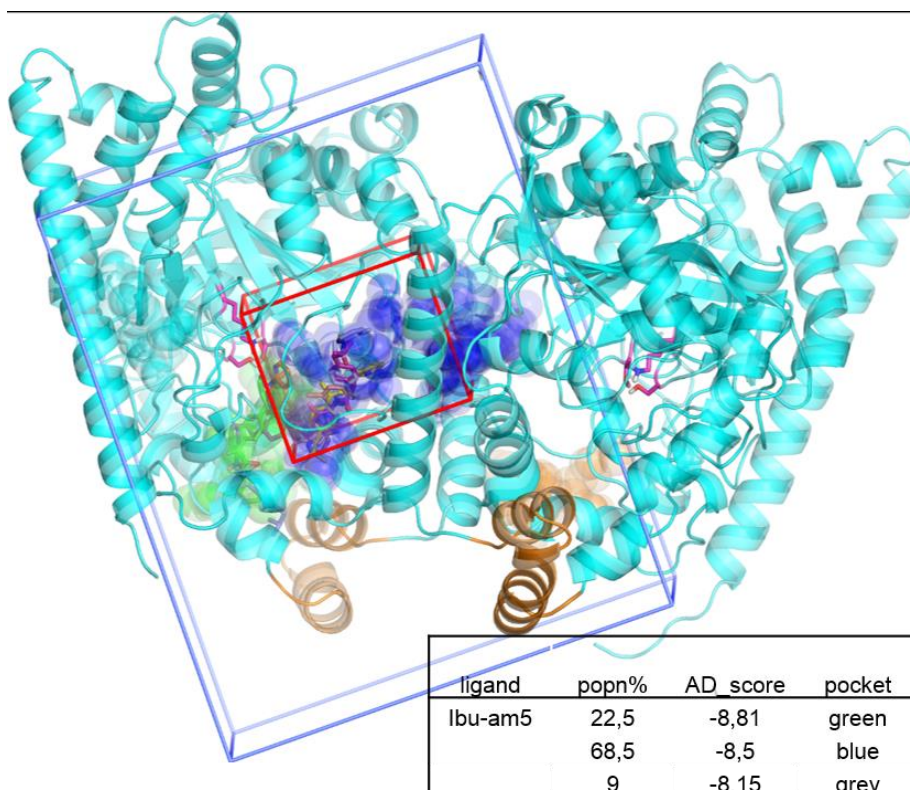


Fig. 31: Docking results on the box (blue) that includes the pockets predicted by fpocket (in transparent spheres with the colour code used in the Table 12). Rat FAAH are represented by cartoon, showing helices $\alpha 18$ - $\alpha 19$ in orange cartoon and catalytic triad in magenta sticks. Ligand poses of the docking are displayed in sticks and the putative box for the allosteric site are represented in red. Results are listed in the table at the bottom of the figure. AD scores are expressed in kcal/mol.

The docking prediction has reported all the solutions investigated in the competitive site for the binding of the enantiomers of Ibu-AM5, Flu-AM1 and TPA5. These solutions could be included in the green and grey pockets. Nonetheless, a high percentage of solutions fill the blue pocket. Taking into account these results, we have defined a box located between the catalytic triad and the interface between monomers and we used this box to examine the binding of mixed-type and non-competitive inhibitors in this pocket (red box in Fig. 31).

6.2 Molecular docking in the allosteric pocket

The binding mode of the inhibitors (*S*)-Ibu-AM5, (*R*)-Flu-AM1 and TPA27 to the rFAAH allosteric site was studied combining molecular docking and MD simulations.

The ligands bind a region between catalytic triad and CP. Two binding modes that differ in the orientation of the amide moiety were found (Fig. 32). Thus, the amide moiety may point towards either the catalytic triad (A-mode) or the interface between FAAH monomers (B-mode).

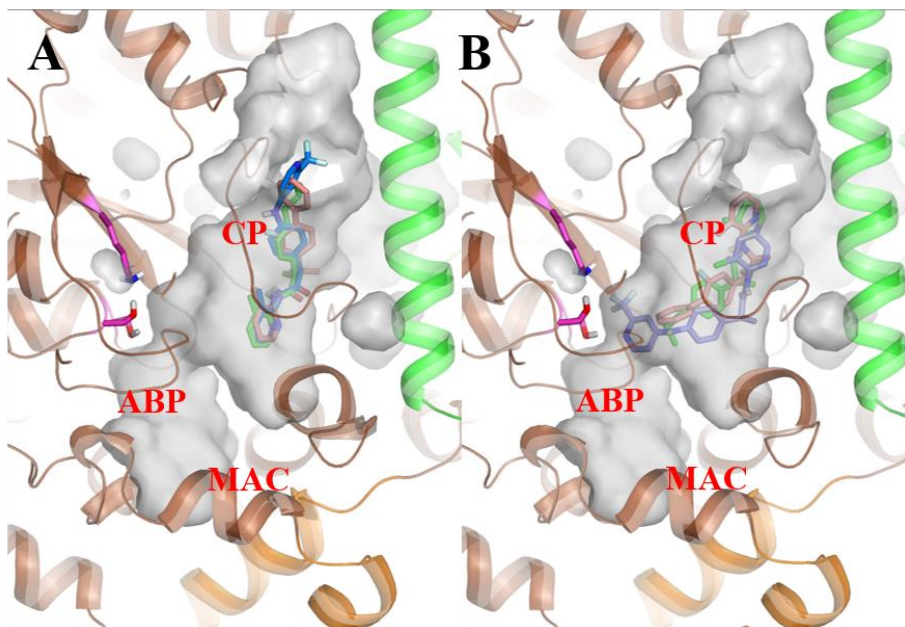


Fig. 32: Molecular docking of (*S*)-Ibu-AM5 (green), (*R*)-Flu-AM1 (pink) and TPA27 (blue) in the allosteric pocket found by fpocket. A: A-mode; B: B-mode. FAAH monomers are represented in cartoons (green for monomer A and brown for monomer B). Internal cavities are represented by surface and catalytic triad is represented by magenta sticks.

The A-mode achieved better scores for all the ligands and was found to be the most populated cluster (Table 11). The A-binding mode yielded very similar results for (*S*)-Ibu-AM5, (*R*)-Flu-AM1 and TPA27, having the pyridine ring in the same conformation, whilst few differences in the positioning of pyridine ring were found for the B-binding mode. Docking results were also re-scored using MM/GBSA calculations that confirmed that the two modes slightly differ in energy, confirming the preference for the A mode for Ibu-AM5 and Flu-AM1, but indicating a preference for the B-mode for TPA27. However, keeping in mind the uncertainty of MM/GBSA calculations, caution must be taken to not overemphasize the significance of the reduced differences in the predicted binding affinities.

DOCKING

ligand	mode	Pop%	AD score	MMGBSA
(S)-Ibu-am5	A	79	-8,2	-35,14
	B	5	-8,02	-33,17
(R)-Flu-am1	A	60	-8,62	-36,66
	B	30	-8,22	-35,79
TPA27	A	51	-8,68	-45,57
	B	3	-8,22	-47,62

Table 11: Docking results in the allosteric pocket for (S)-Ibu-AM5, (R)-Flu-AM1 and TPA27. AD score and MM/GBSA values are expressed in kcal/mol.

6.3 Molecular dynamics studies in the allosteric pocket

To further check the structural integrity of two binding modes, the best poses of each docking cluster were submitted to 100 ns of all atom MD simulation. MD simulations were run on the FAAH dimer, loading the same docking pose in each monomer, while the analysis of MD simulations was carried out in the single monomer.

6.3.1 Ibu-AM5 MD simulations

The MD simulation starting from the A-mode of Ibu-AM5 showed differences about the position of the ligand within the CP in the two monomers, as a consequence of the different fluctuation of the ligand in the first 40 ns of MD simulation, as showed by the RMSD plot (Fig. 33).

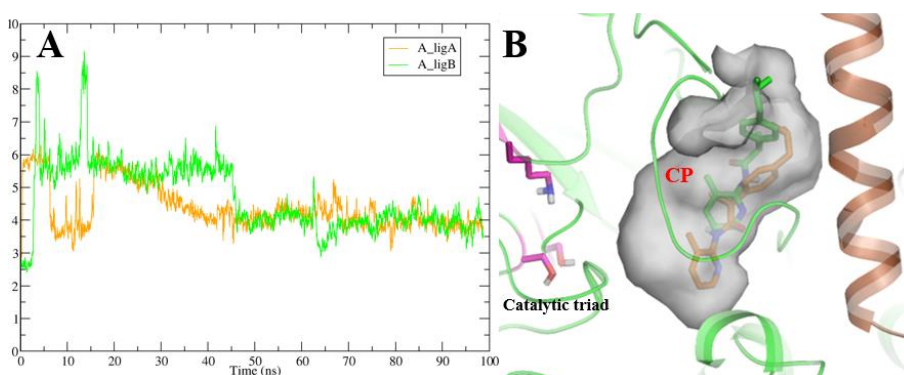


Fig. 33: MD refinement of Ibu-AM5 A-mode in the allosteric pocket. A: RMSD plot during 100 ns of MD refinement of the ligand in monomer A (orange) and monomer B (green), referred to the docking. B: superimposition of the monomers after 100 ns of MD refining: allosteric pocket is represented as internal surface (grey), ligand in monomer A is orange and in monomer B is green. The brown helix represents the other monomer.

The ligand in monomer A, after an initial equilibration, formed two stable hydrogen bonds between the carbonyl group of the amide moiety and the main chains of Gly272 and Gln273, and the hydrogen bond between the nitrogen atom of the pyridine ring and the sidechain of Gln273 (Fig. 34). On the contrary, the simulation in monomer B did not show specific H-bonds between ligand and enzyme, while the isobutyl moiety was located in the tip of the CP.

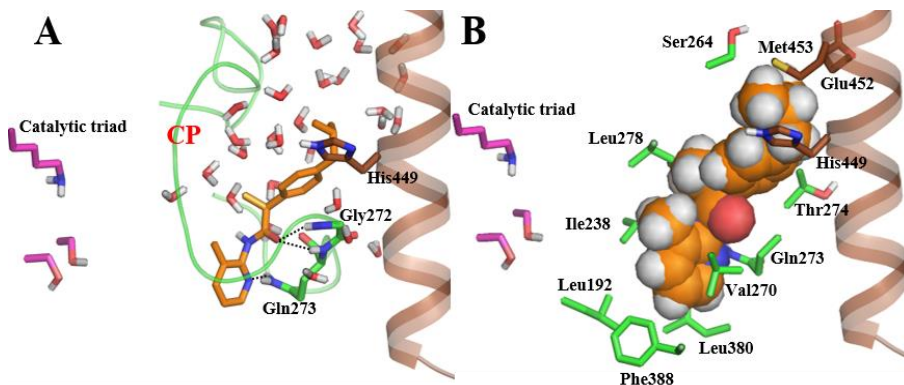


Fig. 34: A-mode of Ibu-AM5 refined after 100 ns of MD. Residues of monomer A are coloured in green and residues of monomer B are coloured in brown. A) Hydrogen bond of Ibu-AM5 (orange, in sticks) in A-mode. Water molecule at the interface between FAAH monomers are displayed as sticks. B) Apolar interaction in the binding pocket of the FAAH. The ligand Ibu-AM5 is represented in orange by van der Waals spheres.

In addition, MD simulations starting from the B-mode showed different results in the two monomers. In fact, as showed in the RMSD plot, the ligands in the two monomers led to different ensembles after 50 ns, showing an increase of the RMSD for the ligand in monomer A (Fig. 35).

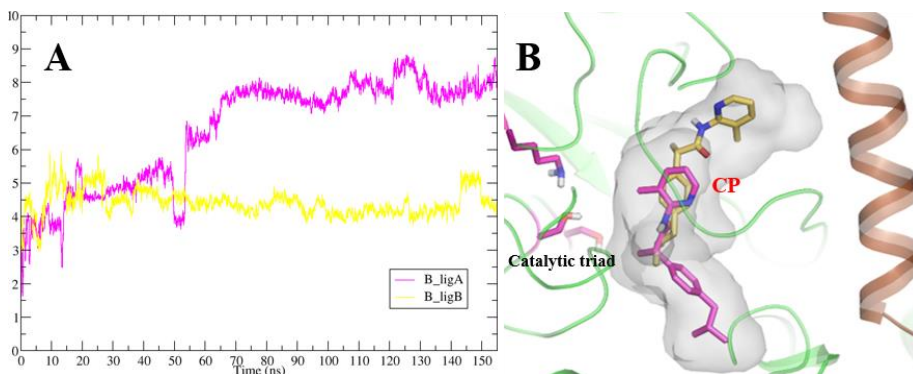


Fig. 35: MD refinement of Ibu-AM5 B-mode in the allosteric pocket. A: RMSD plot during 150 ns of MD refinement of the ligand in monomer A (magenta) and monomer B (yellow), referred to the docking. B: superimposition of the monomers after 150 ns of MD refining: allosteric pocket is represented as internal surface (grey), ligand in monomer A is magenta and in monomer B is yellow. The brown helix represents the other monomer.

In particular, the RMSD relative to the ligand in monomer A showed large fluctuations in the first 50 ns of simulations and highlights a slow equilibration of the ligand. Visual inspection of the MD trajectory revealed that, during this long equilibration, the ligand, starting from a position very similar to that found in the monomer B, progressively enter within the CP, until the isobutyl moiety of Ibu-AM5 fills in a hydrophobic cavity formed by Phe381, Phe388, Leu380, Leu192 and Leu404. This binding mode is further stabilised by the formation of hydrogen bonds between the nitrogen on the pyridine ring and the main chains of Cys269 and Val270. In addition, Tyr271 formed stacking interaction with the pyridine ring, while the methyl group on the pyridine ring was packed between Met191, Leu278 and Leu154 (Fig. 36).

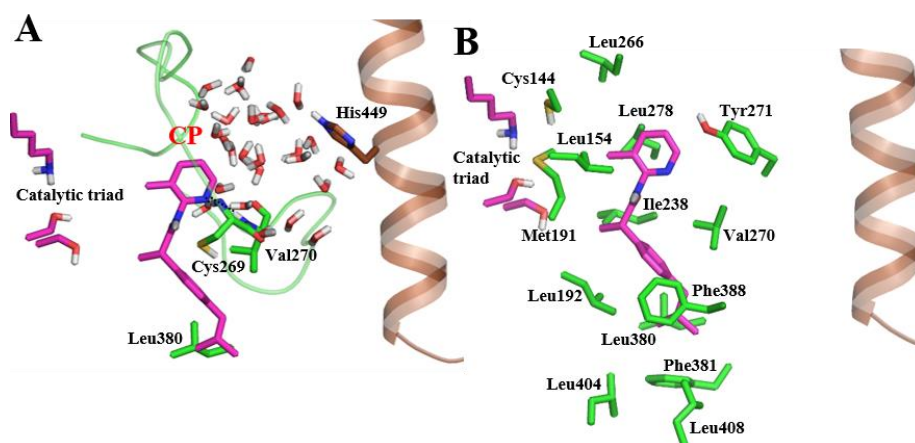


Fig. 36: B-mode of Ibu-AM5 in monomer A refined after 150 ns of MD. Residues of monomer A are coloured in green and residues of monomer B are coloured in brown. A) Hydrogen bond of Ibu-AM5 (magenta, in sticks) in B-mode. Water molecule at the interface between FAAH monomers are displayed by sticks. B) Apolar interaction in the binding pocket of the FAAH.

The binding of the ligand in monomer B showed different behaviour, with fewer fluctuations in the initial phase of MD simulation. The isobutyl moiety interacts with Leu192, Phe388, Leu380 and Ile238, while the carbonyl of the amide moiety forms hydrogen bonds through water molecule with the main chains of Cys269 and Val270. Moreover, this conformation is further stabilised by hydrogen bonds of the amide moiety with the backbone of Lys263, and between the nitrogen on the pyridine group and the backbone of Leu266 (Fig. 37).

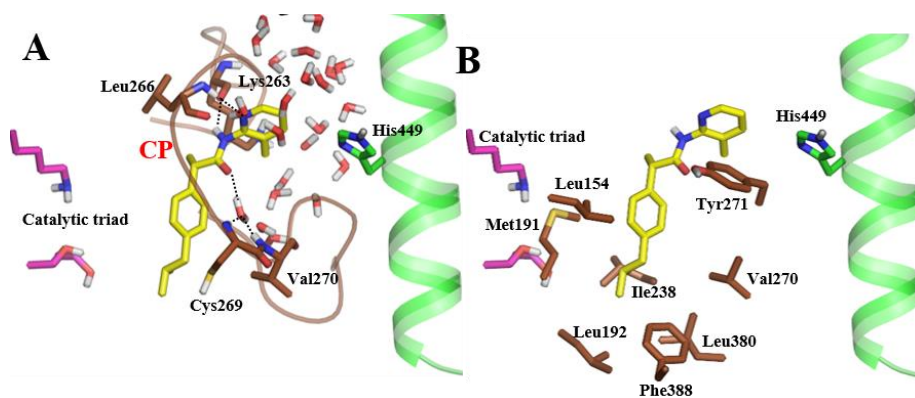


Fig. 37: B-mode of Ibu-AM5 in monomer B refined after 150 ns of MD. Residues of monomer B are coloured in brown and residues of monomer A are coloured in green. A) Hydrogen bond of Ibu-AM5 (yellow, in sticks) in B-mode. Water molecule at the interface between FAAH monomers are displayed by sticks. B) Apolar interaction in the binding pocket of the FAAH.

Superimposition of the bindings in the two monomers highlights some differences in the enzyme structure that lead to different ensembles (Fig. 38): i) the displacement of the loop 376-399 leads to the rearrangement of Leu380 and Phe381, that accommodate the isobutyl moiety deeper in an hydrophobic cavity formed by Phe381, Phe388, Leu380, Leu192 and Leu404; ii) the direct interactions of the pyridine nitrogen with the anionic hole formed by main chains of Cys269 and Val270, that helped the inhibitor to adopt the conformation able to gain the entrance in the hydrophobic pocket; and iii) the orientation of the methyl group on the pyridine ring that permanently interacts with Met191 and Leu156.

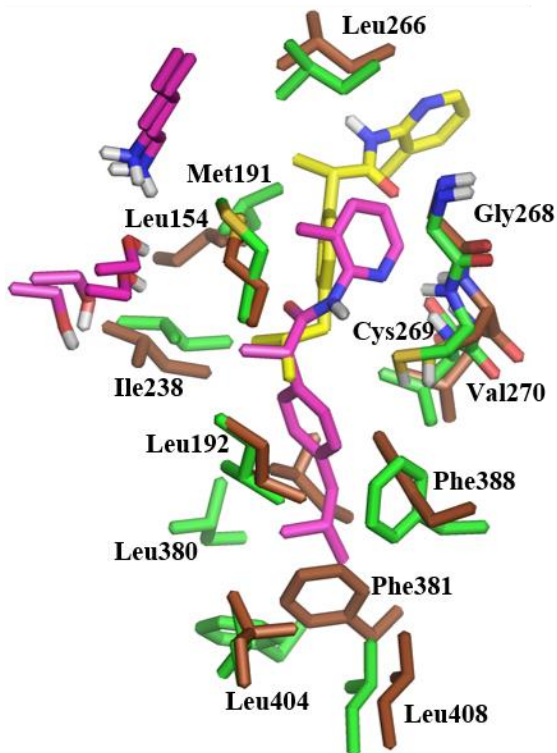


Fig. 38: Superimposition of the binding mode B of Ibu-AM5 in the allosteric pocket. Catalytic triad are represented in magenta sticks. Ibu-AM5 (magenta in monomer A, yellow in monomer B) and surrounding residues are (green in monomer A, brown in monomer B) represented by stick.

6.3.2 Flu-AM1 MD simulations

The MD simulations starting from the A-binding mode of Flu-AM1 showed slightly different conformations of the ligand in the two monomers. As shown in the RMSD plot, the ligand in monomer A undergoes to major modifications, resulting in a different occupation of the CP by biphenyl and methyl on C-2 moieties (Fig. 39), while the ligand in monomer B showed a very stable binding mode along the 100 ns trajectory.

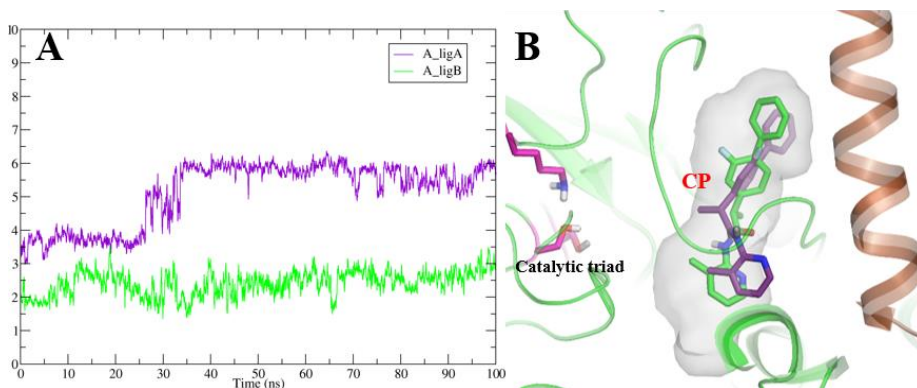


Fig. 39: MD refinement of Flu-AM1 A-mode in the allosteric pocket. A: RMSD plot during 100 ns of MD refinement of the ligand in monomer A (violet) and monomer B (green), referred to the docking. B: superimposition of the monomers after 100 ns of MD refining: allosteric pocket is represented as internal surface (grey), ligand in monomer A is violet and in monomer B is green. The brown helix represents the other monomer.

The stability of the binding after 100 ns MD of the ligand in monomer B prompted us to select this binding mode as the most representative pose of the A-mode. Analysis of the binding mode showed similar array of interactions of the A-mode of Ibu-AM5, with the biphenyl moiety partially facing to the aqueous environment, establishing few hydrophobic contacts with Met453 and Leu278, while the polar portion of the inhibitor is stabilised by hydrogen bonds with Gln273 backbone and sidechain (Fig. 40). Finally, the methylpyridine ring established hydrophobic contacts with Ile238, Leu380 and Val270.

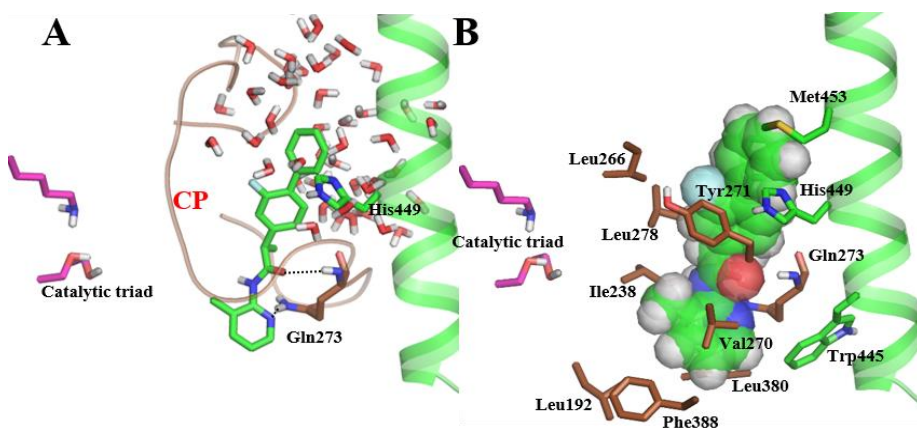


Fig. 40: A-mode of Flu-AM1 in monomer B refined after 100 ns of MD. Interacting residues are showed in sticks (brown, monomer B; green, monomer A). A) Hydrogen bond of Flu-AM1 (green, in sticks) in B-mode. B) Apolar interaction in the binding pocket of the FAAH. The ligand Flu-AM1 is represented in green by van der Waals spheres.

The MD simulation of the B-binding mode of Flu-AM1 showed the same conformation of the ligand in the two monomers, but a different positioning within the pocket. The RMSD plot showed some fluctuations, in particular in the last 15 ns of MD (Fig. 41). Analysis of the trajectory revealed that they were due to the transient rotation of the methyl-pyridine ring.

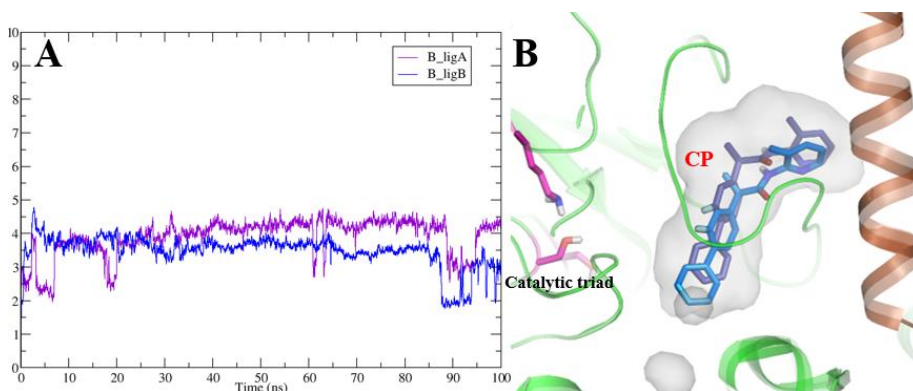


Fig. 41: MD refinement of Flu-AM1 B-mode in the allosteric pocket. A: RMSD plot during 100 ns of MD refinement of the ligand in monomer A (violet) and monomer B (blue), referred to the docking. B: superimposition of the monomers after 100 ns of MD refining: allosteric pocket is represented as internal surface (grey), ligand in monomer A is violet and in monomer B is blue. The brown helix represents the other monomer.

The analysis of the binding modes found in the two monomers highlighted a similar pattern of interactions. Here we describe the binding in monomer B, since it is characterized by a better stability according to the RMSD plot in Fig. 41. The B-mode of Flu-AM1 showed the biphenyl moiety filling a hydrophobic pocket formed by Leu192, Ile238, Val276, Leu278, Leu380 and Phe388. Furthermore, the carbonyl of the amide moiety forms hydrogen bond with the backbone of Gly272, the methyl-pyridine ring is stabilised through stacking interactions with His449 and Tyr271, but the methyl group is surrounded by water molecules (Fig. 42).

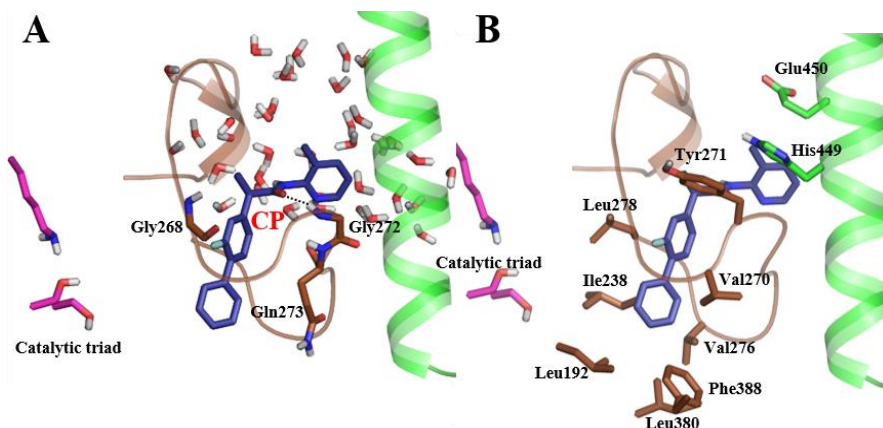


Fig. 42: A-mode of Flu-AM1 in monomer B refined after 100 ns of MD. Interacting residues are showed in sticks (brown, monomer B; green, monomer A). A) Hydrogen bond of Flu-AM1 (blue, in sticks) in B-mode. Water molecule at the interface between FAAH monomers are displayed by sticks. B) Apolar interaction in the binding pocket of the FAAH.

6.3.3 TPA27 MD simulations

The MD simulations of the A-binding mode of TPA27 yielded similar results in the two monomers after 100 ns MD refinement, showing slightly difference in the orientation of the chloropyridine ring and trifluoropyridine moieties (Fig. 43).

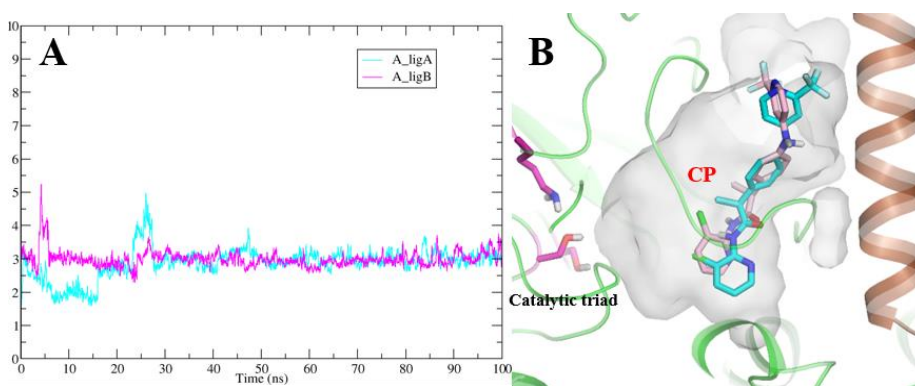


Fig. 43: MD refinement of TPA27 A-mode in the allosteric pocket. A: RMSD plot during 100 ns of MD refinement of the ligand in monomer A (cyan) and monomer B (magenta), referred to the docking. B: superimposition of the monomers after 100 ns of MD refining: allosteric pocket is represented as internal surface (grey), ligand in monomer A is cyan and in monomer B is pink. The brown helix represents the other monomer.

The A-binding mode of TPA27 was similar to the pose described for Ibu-AM5 and Flu-AM1, in particular regarding the portion of the molecule shared with profen derivatives. Thus, the ligand is stabilised by hydrogen bonds between the carbonyl amide and the backbone of Gln273 (as seen for A-mode of Ibu-AM5 and Flu-AM1), and hydrophobic interactions of the methylpyridine ring with Phe388, Leu380, Ile238 and Val270, and of the methyl on the chiral centre with Leu278. The different shape of the 4-((2-(trifluoromethyl)pyridin-4-yl)amino)phenyl moiety, with respect to the biphenyl of Flu-AM1, allow more hydrophobic contacts with residues of the second monomer (Met454, His449 and Trp445), but also water-mediated hydrogen bond of the trifluoromethyl-pyridine moiety with sidechains of Ser254 and Glu453 at the interface with the other monomer (Fig. 44). Therefore, the presence of hydrogen bond donors and acceptors that characterize the TPA series with respect to the profen derivatives, contributed to stabilise the A-mode in the allosteric pocket.

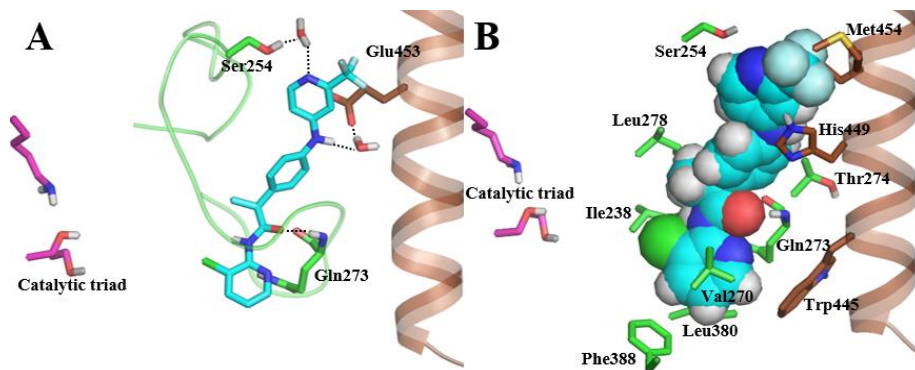


Fig. 44: A-mode of TPA27 in monomer A refined after 100 ns of MD. Interacting residues are showed in sticks (brown, monomer B; green, monomer A). A) Hydrogen bond of TPA27 (cyan, in sticks) in B-mode. B) Apolar interaction in the binding pocket of the FAAH. The ligand TPA27 is represented in cyan by van der Waals spheres.

The B-binding mode of TPA27 showed very distinct poses in the two monomers. As seen in the RMSD plot, the ligand in monomer A showed large fluctuations and filled an area near to the catalytic triad. On the contrary, the simulation in monomer B led to a stable binding in the CP (Fig. 45).

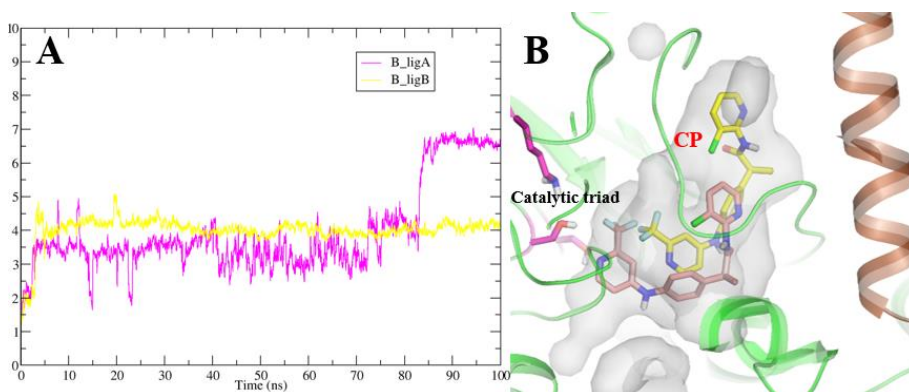


Fig. 45: MD refinement of TPA27 B-mode in the allosteric pocket. A: RMSD plot during 100 ns of MD refinement of the ligand in monomer A (magenta) and monomer B (yellow), referred to the docking. B: superimposition of the monomers after 100 ns of MD refining: allosteric pocket is represented as internal surface (grey), ligand in monomer A is pink and in monomer B is yellow. The brown helix represents the other monomer.

The B-mode in the monomer B formed a water-mediated hydrogen bond with the sidechain of Ala275 and showed stacking interaction with Tyr271 and hydrophobic contacts with Met191, Leu192, Val270, Leu278 (Fig. 46).

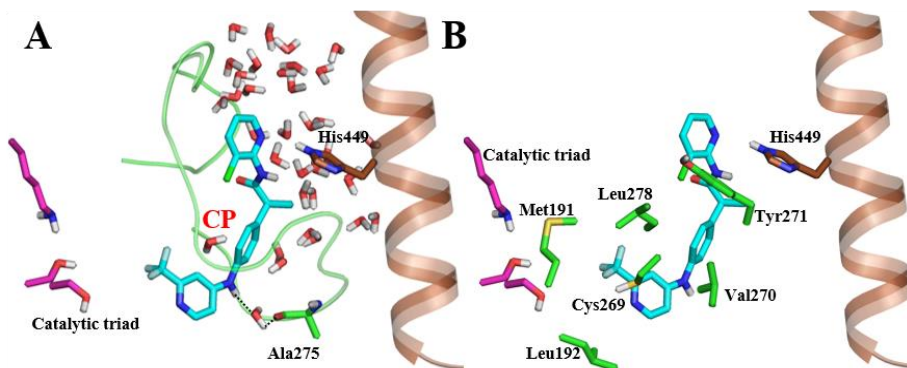


Fig. 46: B-mode of TPA27 in monomer A refined after 100 ns of MD. Interacting residues are showed in sticks (brown, monomer B; green, monomer A). A) Hydrogen bond of TPA27 (cyan, in sticks) in B-mode. B) Apolar interaction in the binding pocket of the FAAH.

Computational data about the binding mode of Ibu-AM5, Flu-AM1 and TPA27 do not allow a clear definition of the binding mode. QM/MM calculations are currently running in order to have a clearer picture of the binding energetics in order to establish the preferred binding mode of each ligand in the allosteric site.

Nevertheless, we designed a series of derivatives of Ibu-AM5 and Flu-AM1, in order to get more information on the SAR that could lead to the selection of the best binding mode for each ligand.

6.4 Profen amide derivatives

6.4.1 Ibu-AM5 derivatives

Taking into account the binding hypothesis of (*S*)-Ibu-AM5 for the competitive and allosteric site, we designed a number of Ibu-AM5 derivatives by varying the chemical nature of the amide group in order to improve the SAR.

Kinetic experiments highlighted how small substitutions should dramatically affect the inhibition mechanism and binding preferences of TPA and Ibu-am derivatives. Moreover, due to the mixed nature of Ibu-AM5 inhibition, we hypothesize that these compounds bind two different binding sites. In light of such considerations, limited information can be derived by SAR analysis, since we actually do not know if changes in the activity are due to changes in affinity toward the competitive site, the allosteric site or both.

We firstly investigated the role of the pyridine nitrogen substitution (Table 12).

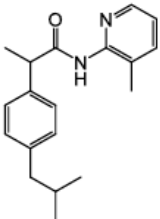
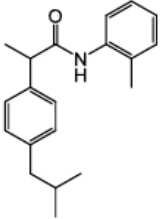
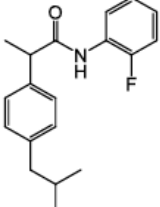
Compound	Formula	Max inhibition (%)	IC ₅₀ (μM)
Ibu-AM5		100	0.52
Ibu-AM48		100	2.0
Ibu-AM49		100	2.4

Table 12: Maximum percentage and IC₅₀ values for inhibition of rat brain AEA hydrolysis by compound Ibu-AM5, Ibu-AM48-49.

The loss of the pyridine nitrogen worsened the affinity, in agreement with the (*S*)-Ibu-AM5 binding mode described in chapter 2. The nitrogen is indeed involved in a hydrogen bond with Trp531. The substitution of the methyl group of the pyridine moiety of TPA5 with the more polar hydroxyl group resulted in a reduction of activity (Ibu-AM50, Table 13). This result is in agreement with the binding mode proposed for the competitive site, wherein the methyl group fills a hydrophobic pocket formed by Leu404 and Ile407 (mutated in mouse). In the putative allosteric binding mode, the methyl group fills a hydrophobic environment in the B-mode of Ibu-AM5, while the pyridine nitrogen is involved in hydrogen bond with Val270.

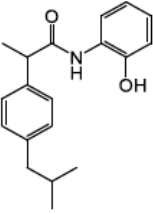
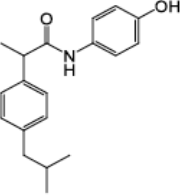
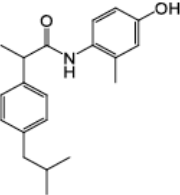
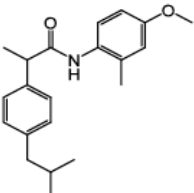
Compound	Formula	Max inhibition (%)	IC ₅₀ (μM)
Ibu-AM50		100	8.5
Ibu-AM51		100	3.8
Ibu-AM52		100	0.35
Ibu-AM53		100	4.6

Table 13: Maximum percentage and IC₅₀ values for inhibition of rat brain AEA hydrolysis by compound Ibu-AM50-53.

To further explore the chemical features of the pockets filled by the methylpyridine moiety of Ibu-AM5, we also designed a series of compounds bearing hydrogen donor and acceptor groups on a phenyl ring in the amide moiety (Table 13). The results demonstrated that the hydroxyl group on the phenyl ring induce loss of activity when introduced in position 2, but it is better tolerated in position 4 (Ibu-AM51). Hence, we designed compound Ibu-AM52, which is the only compound of this series to show low micromolar activity for rFAAH, showing 7-fold increase in activity compared to Ibu-am48. Therefore, Ibu-AM52 confirmed the need of a hydrophobic group in *ortho* to the amide bond, while demonstrated the possibility to exploit the *para* position for extra polar interactions. Among the putative binding mode found in the allosteric pocket, this behaviour would be in better agreement with both B-mode hypotheses of binding (Fig. 36 and 37), since the amidic portion points to the cytosolic environment where the 4-hydroxyl group might establish water bridged interactions with residues in the CP. On the contrary,

in the competitive site the methyl-pyridine moiety (Fig. 13) is tailored in a hydrophobic pocket, and therefore should not accommodate any substituent in position 4 of the phenyl ring. Therefore, we cannot exclude that Ibu-AM52 could reveal a different mode of inhibition with respect to Ibu-AM5.

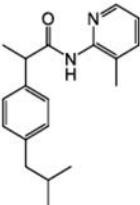
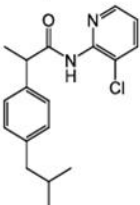
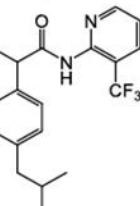
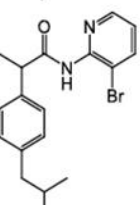
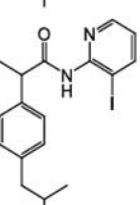
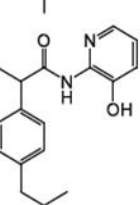
Compound	Formula	Max inhibition (%)	IC ₅₀ (μM)
Ibu-AM5		100	0.52
Ibu-AM54		100	0.91
Ibu-AM55		100	0.36
Ibu-AM56		100	0.083
Ibu-AM57		100	0.12
Ibu-AM58		100	2.1

Table 14: Maximum percentage and IC₅₀ values for inhibition of rat brain AEA hydrolysis by compound Ibu-AM5, Ibu-AM54-58.

To explore the chemical requirements of the position 3 of the pyridine amide moiety we have designed compounds with halogen. The 3-chlorine derivative showed small reduction in activity as compared to Ibu-AM5, while the replacement of chlorine with bromine, iodine and trifluoromethyl groups improved the inhibitory activity. Among these, the 3-bromopyridine analogue Ibu-AM56 is the most potent FAAH inhibitor of the Ibu-am series with an IC₅₀ value of 0.083 μ M. It is noteworthy that the effects of the 3-chlorine and 3-bromine substitution induce different effects in the Ibu-am and TPA series. The comparison of the activities of Ibu-AM54 with TPA27 and of Ibu-AM56 with TPA24 revealed different structure-activity relationships, suggesting different binding modes for the two series, which is in agreement with our computational data.

We also evaluated the effects of a polar group in place of the methyl group of Ibu-AM5. The comparison of Ibu-AM58 with Ibu-AM5 reveals that the replacement of the methyl with a hydroxyl group leads to a 4-fold reduction in activity, confirming the trend showed by the aryl analogues Ibu-am48 and Ibu-AM50. Therefore, the introduction of the hydroxyl group in position 3 of the pyridine ring is not favourable for the activity, as expected by the predicted binding modes, where 3-methyl group of Ibu-AM5 fills hydrophobic cavities in both competitive (Fig. 13) and allosteric (Fig. 36) binding sites. However, the comparison of Ibu-AM58 and Ibu-AM50 activities indicates that the pyridine nitrogen increased the inhibitory activity by a factor of 4. (Table 14).

6.4.2 Flu-AM1 derivatives

On the basis of (*R*)-Flu-AM1 putative binding modes found for competitive and allosteric sites, we designed a number of Flu-AM1 derivatives. The first compounds synthesized and tested are reported in Table 15.

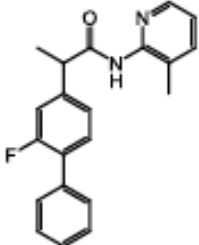
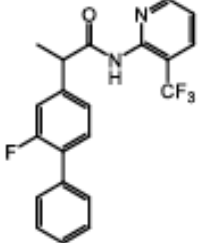
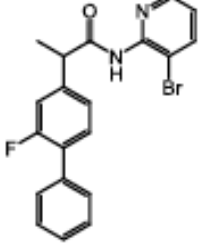
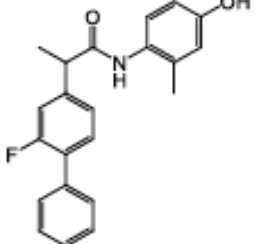
Compound	Formula	Max inhibition (%)	IC ₅₀ (μM)
Flu-AM1		100	0.44
Flu-AM2		100	0.11
Flu-AM3		100	0.021
Flu-AM4		100	0.15

Table 15: Maximum percentage and IC₅₀ values for inhibition of rat brain AEA hydrolysis by compound Flu-AM1-4.

As a general observation, we found that the behaviour of Flu-AM1 derivatives correlate with the trends observed for Ibu-AM5 derivatives reported in paragraph 5.4.1. Indeed the 3-bromo-pyridine derivative Flu-AM3 is the most active of the series, while 3-CF₃-pyridine (Flu-AM2) and the 2-methyl-4-hydroxy-phenyl (Flu-AM4) show little improvements of activity with respect to the lead Flu-AM1. This consideration is in good agreement with the reported binding modes in the competitive site. On the contrary, the Flu-AM1 B-binding mode described for the allosteric site don't show specific interactions of the methyl-pyridine moiety, that is not involved in any specific

interactions, being surrounded by water molecules, and it would be in better agreement with the A-binding mode. Therefore, more detailed investigations will be required in order to study the binding mode of these promising ligands.

7. Identification and rational design of novel peptides that interfere with the interaction between hUbA1/UbcH10.

7.1 Introduction

UbcH10 is a member of the ubiquitin conjugation enzymes (Ubc), a component of the anaphase-promoting complex and a key regulator of cell cycle progression [89], as it induces the ubiquitination and degradation of cyclins A and B [90]. Previous studies have indicated that UbcH10 overexpression might be associated in the late stages of thyroid neoplastic transformation [91], and that high levels of UbcH10 correlate with most aggressive grade tumour in breast cancer [92]. Similar evidences have been found for several tumour types, such as ovarian [93], colorectal and brain cancers [94] and different lymphoma [95]. Moreover, in numerous cancer tissues the UbcH10 expression is relatively higher if compared with the adjacent non-malignant tissues. All these evidences point out that the aberrant expression of UbcH10 could promote tumour expansion through dysfunction of mitotic progression, leading to deregulation of cell growth as confirmed in both thyroid [94] and breast carcinoma [96], where the interference with UbcH10 appears to be potential target for developing an anticancer therapy based on the suppression of its specific biological function.

A key step in the discovery of inhibitors of the UbcH10-mediated ubiquitination is the comprehension of the structural and mechanistic features that mediate conjugation of proteins to ubiquitin (Ub), a complex process that involves a three-step cascade mechanism characterised by growing specificity [96, see 97 for a recent review] (Fig. 47). Thus, the ubiquitin-activating enzyme (UbA1, also known as E1) initiates the ubiquitination cascade by catalysing the ATP-dependent adenylation of the Ub C-terminus (step I). The high-energy anhydride bond thus formed is attacked by the E1 active site cysteine (Cys632 in human UbA1), forming a thioester bond between E1 and Ub (step II). Then Ub is transferred to the active site cysteine of an Ub-Conjugation enzyme (denoted E2), a process promoted by non-covalent binding of a second Ub molecule in the adenylation site (step III and IV). Finally, Ub is conjugated to its substrate with the aid of a protein ligase (known as E3), resulting in the covalent linkage of the Ub C-terminus to the ϵ -amino group of a lysine in the substrate (steps V and VI). In humans there are two E1 enzymes (UbA1 and UbA6) [98], over 30 distinct forms of E2 and about 500-1000 forms of E3, which is largely responsible for conferring specificity to ubiquitination [99].

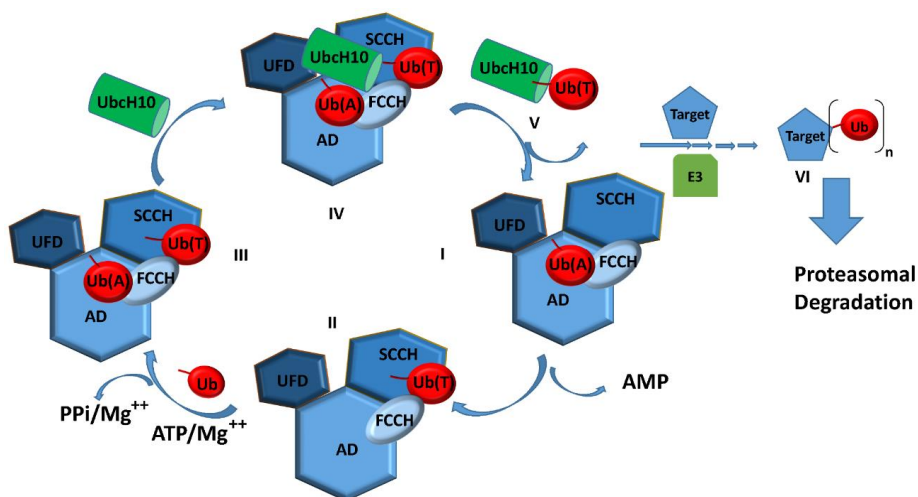


Fig. 47: Ubiquitin conjugation cascade. UbA1 consists of four domains: the Adenylation domain (AD), the First Catalytic Cysteine Half-domain (FCCH), the Second Catalytic Cysteine Half-domain (SCCH) and the Ubiquitin Folding Domain (UFD). I) UbA1 catalyzes the adenylation of the Ub C-terminus in an ATP-dependent process in the AD domain; II) the activated Ub forms a thioester bond with a conserved catalytic cysteine in the SCCH domain of UbA1 [Ub(T)]; III) UbA1 is loaded with a second Ub molecule in the AD domain, followed by its C-terminal adenylation [Ub(A)]; IV) the ternary UbA1,Ub(T)-Ub(A) thioester complex recruits E2 (e.g. UbchH10); V) the thioester-linked Ub is transferred to a conserved E2 cysteine (transthioesterification); VI) E3 mediates the binding of Ub to the target lysine ϵ -amino groups.

To the best of our knowledge, there is not a complete 3D model of the quaternary complex required for the transfer of Ub to the E2 Ubiquitin conjugation enzyme. In these studies we describe a computational strategy to build up the first structural model of the transient tetrameric complex between the doubly Ub-loaded human UbA1 (hereafter denoted UbA1~Ub(T)-Ub(A)) and UbchH10, as a member of E2 family.

The work discussed in this chapter has been published in a peer-reviewed journal article [100] and it is the result of an interdisciplinary collaboration. S. Correale, A. Federico, P. Pallante, A. Fusco and E. Pedone performed protein expression and affinity assays; I. de Paola, L. Zaccaro and A. Galeone synthesised the peptides; C. M. Morgillo, F. J. Luque and B. Catalanotti performed computational calculations.

7.2 Building of the 3D trimeric complex of hUbA1 with doubly loaded Ub

The structural model of hUbA1 was built up by using 1Z7L and 3CMM structures as templates for the hUbA1 SCCH region (1Z7L) and for the AD, FCCH and UFD domains (3CMM), respectively. Moreover, the two conformations of *S. cerevisiae* UbA1 (scUbA1) found in the X-ray structure

3CMM were considered, leading to 3D models named UbA1_A and UbA1_C (see experimental section). The quality of the models was checked by considering a number of structural features, including stereochemical properties, the compatibility between the amino acid sequence and the environment of amino acid side chains, and the patterns of non-bonded interactions. Taking into account the similar scores obtained for the two models and their structural resemblance (RMSD = 1.2 Å), MD refinement was accomplished only for UbA1_C. A stable structure was obtained after the first 5 ns of the trajectory (Fig. 48A). Nevertheless, the structure of each domain was very stable along the trajectory, as demonstrated by the stability of the RMSD of the single domains (Fig. 48B).

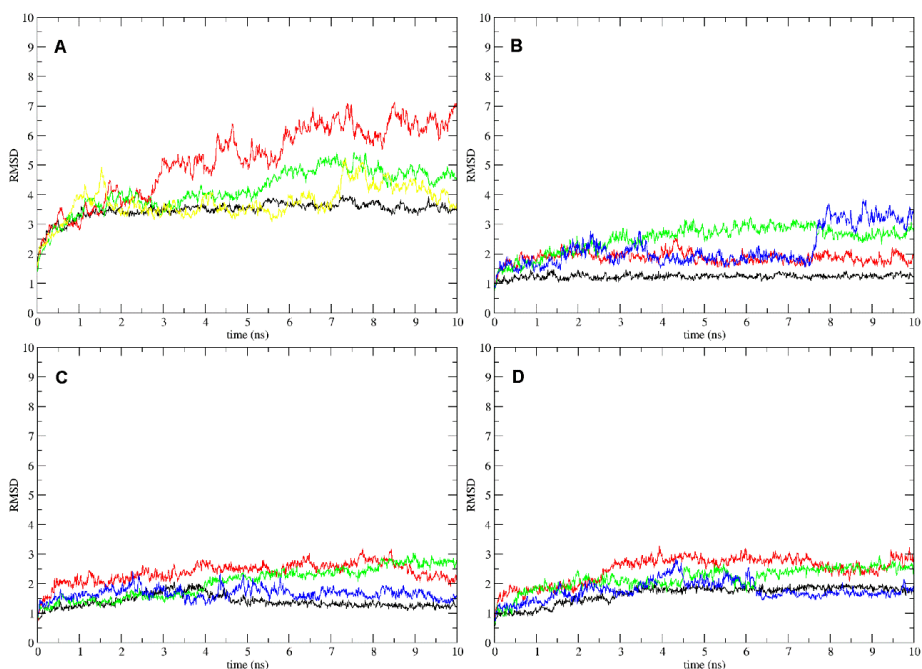


Fig. 48: A: Time evolution (ns) of the RMSD (Å) of the UbA1_C model: hUbA1 apo (red), hUbA1~Ub(T) (yellow), hUbA1~Ub(T)-Ub(A) (green) and hUbA1~Ub(T)-Ub(A)-UbcH10 (black). B, C and D: Structural preservation of the structure of each region. of: hUbA1 apo (B), hUbA1-Ub(T) (C) and UbA1~Ub(T)-Ub(A) (D), AD (black), UFD (green), SCCH (red) and FCCH (blue).

To build up the tetrameric complex between hUbA1, Ub(T), Ub(A) and UbcH10, we first modelled the hUbA1~Ub(T) thioester complex, which was subsequently used to dock a second Ub molecule in the AD domain. Modelling the binding mode of Ub(T) is challenged by the lack of structural and biochemical information about this interaction, and by the covalent linkage of Ub, which is an unusual feature in protein-protein docking. To this end, was adopted a multistep strategy that included the use of two protein-protein docking webserver, HADDOCK [101] and RosettaDock [102], in order to disclose the non-covalent interfaces between the E1 and Ub(T).

Accordingly, we first docked Ub to hUbA1 using HADDOCK by restraining the contact between Cys632 (UbA1) and Gly76 (Ub). Among the 9 clusters that embody the 200 best structures yielded by HADDOCK (Table 16), solutions were chosen on the basis of four criteria: i) the distance from the sulphur atom of Cys632 and the carboxylic oxygen of Gly76, ii) the total score, iii) the total number of poses, and iv) the buried surface area. The selected poses lead to a distance lower than 3.8 Å, and are characterized by a high score, a large number of poses, and a large burial of surface area (see Table 16).

HADDOCK Cluster	population	UbcH10 S-C114 Ub(T) C-ter G76	Haddock Score	SIE ΔG
3	32	3,7	-47,6 +/- 4,6	-4,88
5	5	4,2	-32,6 +/- 6,0	1,78
2	62	3,6	-31,9 +/- 1,2	-6,71
6	5	4,3	-26 +/- 6,5	-4,07
8	4	4,1	-25,8 +/- 2,4	-5,57
4	10	4,7	-19,8 +/- 6,3	-6,91
1	73	4,7	-17,7 +/- 3,6	-4,89
7	5	6,4	-2,3 +/- 5,3	-5,1

Table 16: HADDOCK results for the dimeric complex hUbA1-Ub(T). The structural data include the distance (Å) from the sulphur of the hUbA1 Cys632 to the C-terminal Gly76 of Ub(T). The energy data report the score of the docked structures obtained from HADDOCK and from SIE (kcal/mol). Lowest energy result for clusters 3 and 2 (named respectively Ha and Hb) were selected for Rosetta calculations.

These poses (denoted Ha and Hb) mainly differ in the orientation of Ub relative to the SCCH domain (Fig. 49A). In the lowest energy solution (Ha), Ub forms contacts with SCCH, mainly through ionic and polar interactions, and FCCH, primarily through hydrophobic interactions via the Ile44 patch, which is known to be involved in other non-covalent interactions of Ub, such as in the recognition of UbcH5c, UEV and GLUE domains [103]. In the second pose (Hb), Ub only showed polar contacts between residues in the Ub tail with the SCCH domain.

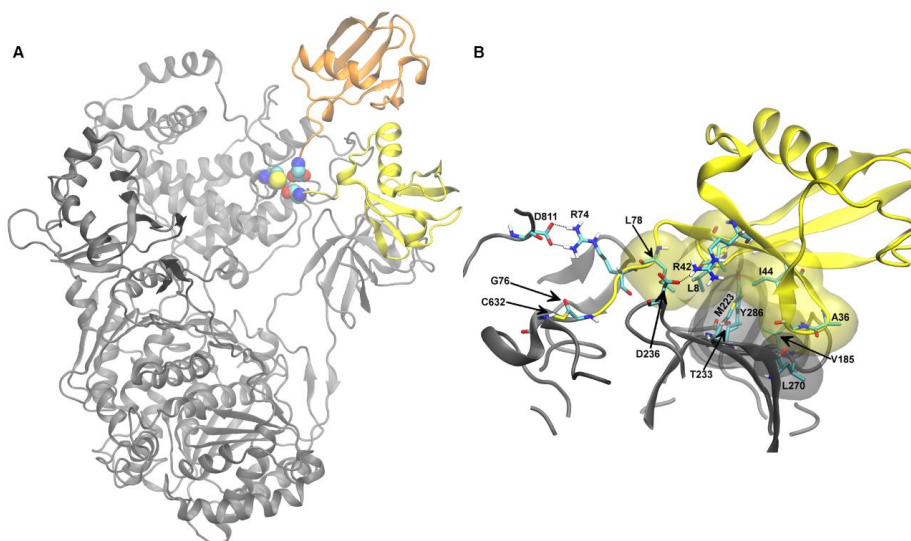


Fig. 49: Model of hUbA1-Ub(T) complex. A) Comparison of the best two binding modes of Ub resulting from HADDOCK calculation, Ha and Hb, shown in yellow and orange, respectively. Terminal Ub-Gly76 and catalytic UbA1-Cys632 are highlighted in spheres coloured by atom type. B) Detail of hUbA1~Ub(T) interactions in the lowest energy MD frame (time 9.6 ns). Apolar hydrogens were omitted for sake of clarity. Colour code: hUbA1, grey; Ub(T), yellow; van der Waals interactions are highlighted with transparent Connolly surfaces. Carbons are in cyan, nitrogen in blue, oxygens in red, sulphur in yellow and hydrogens in white.

The two poses were then checked using RosettaDock. The best ranked solution turned out to be very similar to the best HADDOCK solution (Ha), as noted in a RMSD of 0.82 Å. In contrast, calculations started from pose Hb yielded solutions that showed significant structural differences with regard to the initial structure. Therefore, due to the structural consistency of pose Ha, it was chosen as a model of the hUbA1~Ub(T) complex and subsequently refined by MD simulations, which led to a stable trajectory after the first 2 ns (see Fig. 48A, C). The refined structure supports the hydrophobic contacts between residues Leu8, Ile44, Val70 and Leu73, which interact with FCCH residues Y286, Met223, Val277, Leu178 and Thr233. The hydrophobic interactions involving the Ile44 patch were also reinforced by ionic interactions between Arg42 (Ub(T)) and Asp236 and between Arg74 (Ub(T)) and Asp811 (Fig. 49B).

The trimeric complex was obtained through docking of Ub to the AD site and subsequent MD refinement, which led to a stable trajectory after the first 2 ns (see Fig. 48A, D). The 3D structures closely resembled the X-ray template 3CMM (RMSD of 1.1 Å; Fig. 50A). Three different interfaces might be identified: i) the loop pocket defined by hUbA1 residues Tyr618, Ser621, Glu626, Arg515, Asn512, Asn516 and Arg551 interacting with Ub(A) tail residues Arg72, Arg42 and Arg74 and AMP (Fig. 50B); ii) an hydrophobic patch formed by the Ub residues Leu8, Ile44 and Val70 that form contacts with a hydrophobic area in the hUbA1 AD region formed by residues Phe933

and Phe926 (Fig. 3-C); and iii) the polar interface formed by Ub(T) residues Thr9, Lys11, Thr12, Asp3 interacting with the FCCH region, mainly with residues Glu243, Arg239 and Asn212 (Fig. 50C). Moreover, interactions between Ub(T)-Lys48 and Asp920 and Glu938, not present in the 3CMM structure, were also found.

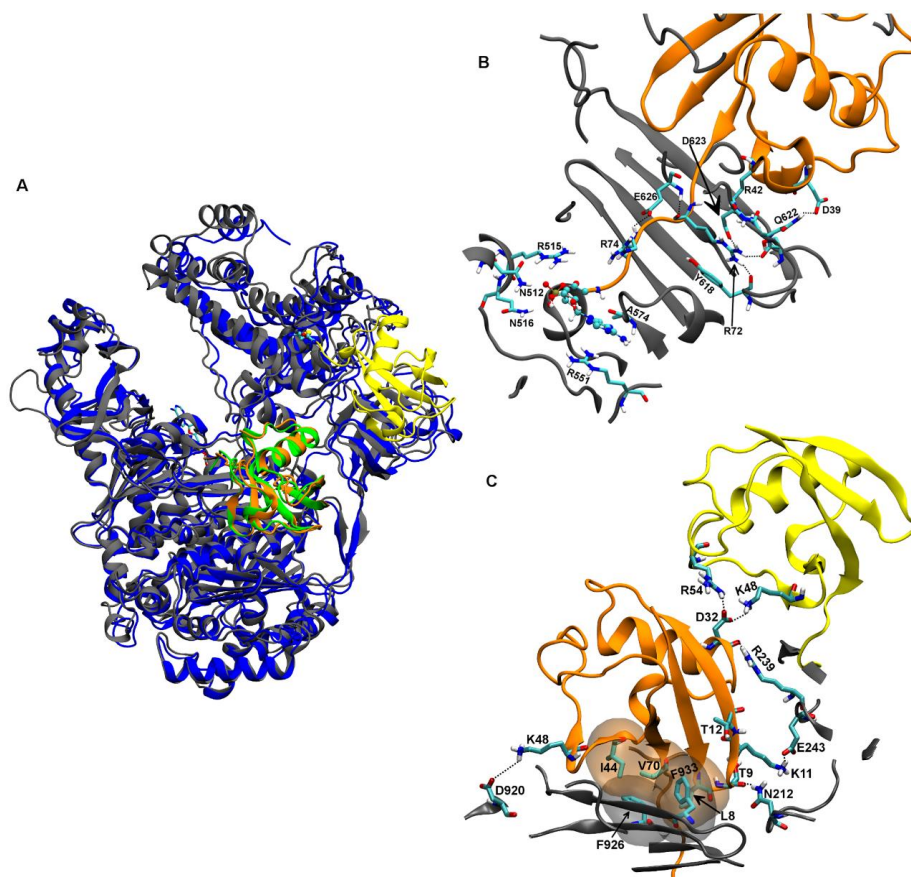


Fig. 50. Model of hUbA1-Ub(T)-Ub(A) complex. A) Superimposition of the hUbA1~Ub(T)-Ub(A) model C_Ha on the crystal structure 3CMM_C; B) Detail of the main interactions of Ub(A) and AMP in the hUbA1 loop pocket; C) Detail of the main interactions between Ub(A) and hUbA1: hydrophobic and polar interface. AMP is highlighted in CPK. Apolar hydrogens were omitted for the sake of clarity. Colour code: hUbA1, grey; Ub(T) yellow; Ub(A), orange; scUbA1, blue; scUb(A), green.

Finally, during our studies, a novel structure of the scUbA1 loaded with two ubiquitin molecules was released in the PDB with the name 4NNJ [104]. The superimposition of the model of hUbA1-Ub(T)-Ub(A) complex obtained with our incremental strategy to the crystal structure (chains C, D, E) leads to a RMSD of 1.5 Å (determined for the Ca carbon atoms), and showed a position of Ub(T) very similar to the pose C_Ha selected in our calculations (Fig. 51), thus supporting the reliability of our model.

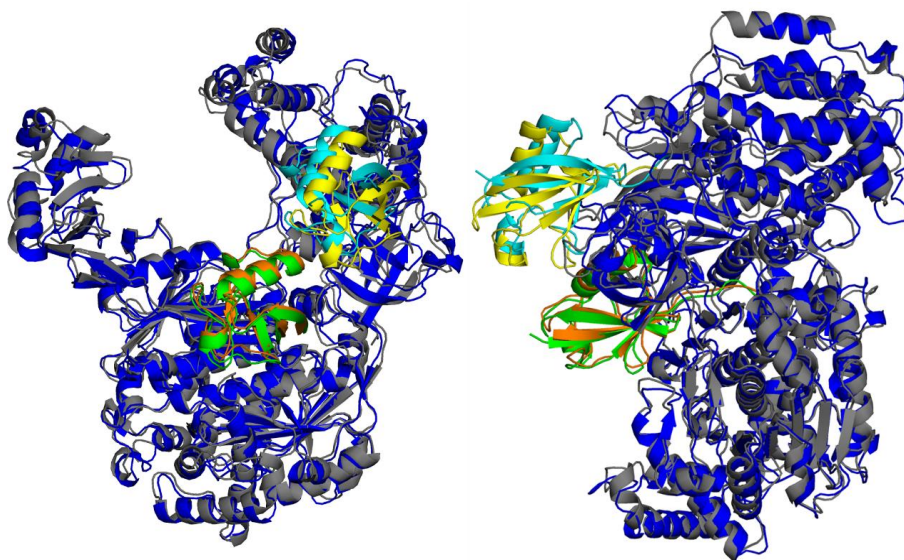


Fig. 51: Superposition of the backbone for the X-ray structure 4NNJ and the 3D model of the ternary complex. Front and side views are shown in the left and right pictures, respectively. Colour code: hUbA1, grey; Ub(T) yellow; Ub(A), orange; scUbA1, magenta scUb(A), green, scUb(A), Cyan.

7.3 Building of the quaternary complex $hUbA1\sim Ub(T)-Ub(A)-UbcH10$

The $hUbA1\sim Ub(T)-Ub(A)$ model was the starting point for the docking with UbcH10. In order to make a more exhaustive sampling, up to four different starting points were considered for docking calculations (see experimental section). HADDOCK calculations yielded 80 clusters. The results were filtered by selecting only poses where the distance from the sulphur atom of the UbcH10 catalytic cysteine (Cys114) to the carbonyl carbon of the C-terminal Gly in Ub(T) was lower than 20 Å, considering this limit as indicative of the side of UbcH10 facing the SCCH region. Moreover, this criterion is consistent with the distance between the Cys residues involved in the transthiolation reaction in the crystal structure 2NVU, representing the tetrameric complex of the NEDD8 system. Only six clusters satisfied the distance cutoff. Among these clusters, Ub(T) adopted the Ha binding mode in five cases, and the Hb arrangement was found in a single case. This suggests that the Ha binding mode position was better suited to accommodate the E2 partner within the E1 groove with the catalytic cysteines facing each other. Table 17 shows the distinct poses ranked according to HADDOCK score as well as to the binding free energy of the complex calculated with the SIE method using the snapshots collected in the MD simulation. A_Ha_L2 emerges as the best pose according to HADDOCK score and SIE binding affinity. Both HADDOCK and SIE scores are consistent in suggesting C_Ha_R and C_Ha_L as feasible poses. The structures of these complexes

differ by around 5.5 Å relative to A_Ha_L2. The A_Ha_L1 and A_Ha_R poses were structurally similar to A_Ha_L2 (RMSD of 3.3 Å) and Ca_Ha_R (RMSD of 4.3 Å), respectively. However, SIE calculations predict that they are less stabilized compared to A_Ha_L1 and A_Ha_R. Finally, C_Hb_R was discarded due to the low energetic score.

Docking	UbcH10 S-C114 HUbA1 S-C632	UbcH10 S-C114 Ub(T) C-ter G76	Haddock Score	SIE ΔG
A_Ha_L2	15,2	17,6	-147.7±11.2	-11.0
C_Ha_R	14,6	14,5	-126.7±5.4	-9,6
C_Ha_L	18,1	17,4	-125.0±5.4	-9,2
A_Ha_L1	16,9	15,1	-118.9±7.3	-8,0
A_Ha_R	11,3	11,8	-125.0±10.0	-7,6
C_Hb_R	16,7	18,5	-96.6±8.3	-3,6

The structural data include the distance (Å) from the sulphur of the UbcH10 Cys114 to the hUbA1 Cys632, and to the C-terminal Gly76 of Ub(T). The energy data report the score of the docked structures obtained from HADDOCK and from SIE (kcal/mol).
doi:10.1371/journal.pone.0112082.t002

Table 17. Comparison of structural and energy data for selected docking results of the quaternary complex.

It is experimentally known that the N-terminal helix and $\beta 1\beta 2$ loop of E2 are directly involved in the formation of the complex [105-109]. In particular, mutational and structural studies disclosed the main role of two basic residues, conserved in the E2 family (positions 33 and 37 in UbcH10 numbering), in assisting the binding to E1. We have therefore examined the role played in the selected models by i) the conserved acidic residues of the UFD region of hUbA1 (i.e. Glu1037, Asp1047 and Glu1049) and ii) the conserved basic residues of the N-terminal helix of UbcH10 (i.e. Lys33' and Gln37'). It is worth noting that while a basic residue in position 33 is conserved in all the members of the E2 family, position 37 shows a higher variation, albeit basic or polar residues are generally found in this position. To this end, the best three solutions (A_Ha_L2, C_Ha_R and C_Ha_L) were subjected to a virtual alanine scanning analysis in order to evaluate the contribution of these residues to the E1-E2 interaction. Even though the results (Table 18) did not show significant interactions (defined as $\Delta\Delta G \geq -0.5$ kcal/mol) with Gln37', the best three models showed a significant contribution to the binding of at least one residue from the N-terminal helix and one residue from the UFD region of UbA1. For the sake of comparison, no significant contribution was found for the mutations in the N-terminal helix for poses A_Ha_L1 and A_Ha_R. In fact, only a single mutation in hUbA1 (Asp1047→Ala) was found to lead to a significant destabilization. This finding, together with the structural resemblance to A_Ha_L2 and Ca_Ha_R and the lower SIE binding free energy (see above), led to their exclusion from further refinements.

Docking	$\Delta\Delta G$ hUbA1			$\Delta\Delta G$ Ubch10	
	E1037A	D1047A	E1049A	K33A	N37A
A_Ha_L2	0.0	-0.8	0.0	-0.8	-0.4
C_Ha_R	-0.2	-0.4	-1.5	-0.7	0.0
C_Ha_L	-0.3	-1.3	0.1	-1.0	-0.1
A_Ha_L1	0.0	-1.2	0.0	-0.2	-0.2
A_Ha_R	-0.2	-0.6	0.0	-0.3	0.1
C_Hb_R	-0.4	0.2	-0.6	-0.7	0.0

Results of the virtual alanine scanning ($\Delta\Delta G$; kcal/mol) due to the mutation to Ala of residues Glu1037, Asp1047 and Glu1049 in hUbA1 and Lys33' and Gln37' in Ubch10 are reported.
doi:10.1371/journal.pone.0112082.t003

Table 18: Alanine scanning.

The three models were further refined by running a series of 50 ns MD simulations, and the binding free energy was determined from SIE calculations performed for the snapshots sampled in the last four 10 ns windows. The results consistently showed that the best binding affinity was obtained for model C_Ha_R (-26.6 ± 0.2 kcal/mol), it being more favorable by 6 and 9 kcal/mol compared to A_Ha_L (-20.2 ± 1.4 kcal/mol) and C_Ha_L (-17.2 ± 1.5 kcal/mol) models. On the basis of the preceding findings, the C_Ha_R model was further refined by extending the MD simulation to 500 ns. The analysis of the trajectory revealed a progressive stabilization of the complex, leading to a binding affinity close to -31 kcal/mol in the last 250 ns (Fig. 52A). The alanine scanning analysis also demonstrated that the residues known to be critical to E1–E2 complex formation contributed significantly to the protein-protein interaction with the only exception of Gln37' (Fig. 52B).

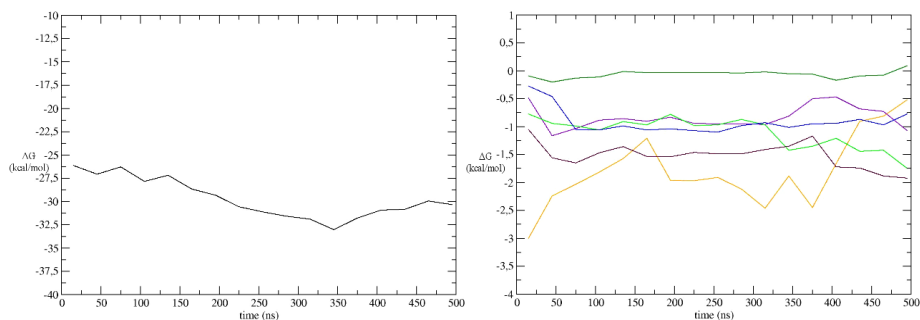


Fig. 52. Energetic analysis. A) SIE values (kcal/mol) determined for the E1-E2 interaction along the trajectory (averaged for 20 ns windows). B) Contribution of key residues as derived from alanine scanning in Ubch10 N-terminal helix and the hUbA1 UFD region during the MD simulation of the model C_Ha_R. Colours: Glu1037, orange; Asp1047, violet; Glu1049, light green; Lys33', bordeaux; Gln36', blue; Gln37', dark green.

During the MD run we observed a change in hUbA1 associated to the rotation in opposite directions of the UFD and SCCH domains with respect to the AD domain (by 20° and of 13° , respectively, as calculated with DynDom [110]). This conformational change caused the widening of the groove defined by the three domains, thus allowing a closer contact between hUbA1 and Ubch10, leading to an increase of the interaction surface (Table 19) and the gradual decrease of the distance between the Ubch10 catalytic cysteine and the Ub(T)

C-terminal glycine crosslinked to UbA1-Cys632 until it stabilised at around 8 Å (Fig. 53).

time (ns)	TOTAL interface	UFD interface	SCCH interface	% UFD	% SCCH
docking	2518	1301	703	52	28
100	2662	1391	588	52	22
200	3211	1628	766	51	24
300	3278	1625	957	50	29
400	2964	1557	728	53	25
500	2659	1571	724	59	27
Final Complex	5437	1558	3162	29	58
X-ray (4II2)	3326	1154	1715	35	52

Table 19: Time evolution of interaction surface (Å²) for selected domains in hUbA1.

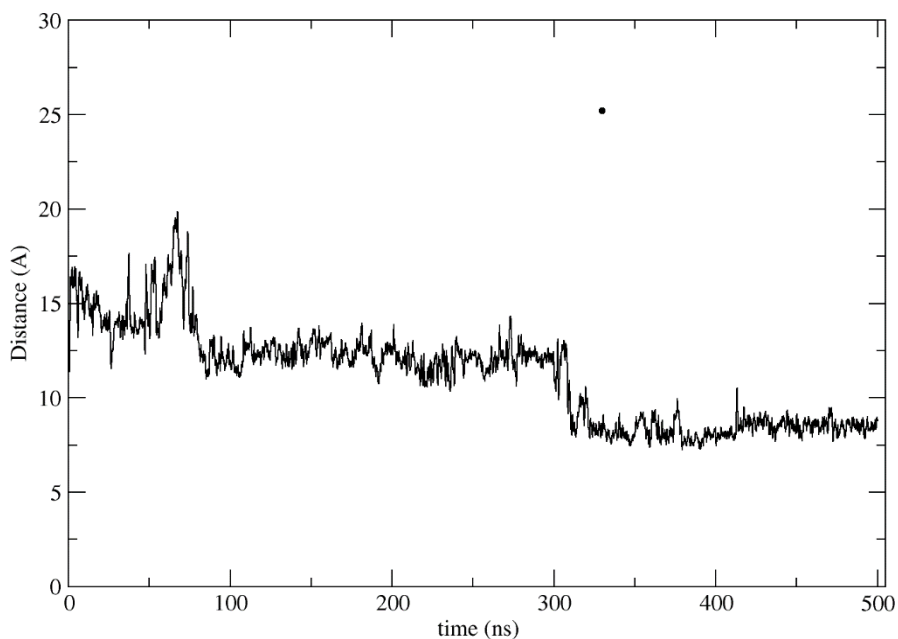


Fig. 53: Analysis of the distance between the sulphur atom of the UbCh10 Cys114 and the carbonyl group of the crosslinked Ub(T) terminal glycine during the 500 ns unconstrained MD.

Analysis of the last 50 ns of the trajectory revealed the presence of two main interaction surfaces, which involve contacts between i) UbCh10 helix H1 and β 1 β 2 loop and hUbA1 UFD domain, and ii) the hUbA1 Cys-cap loop and Ub(T) (Fig. 54).

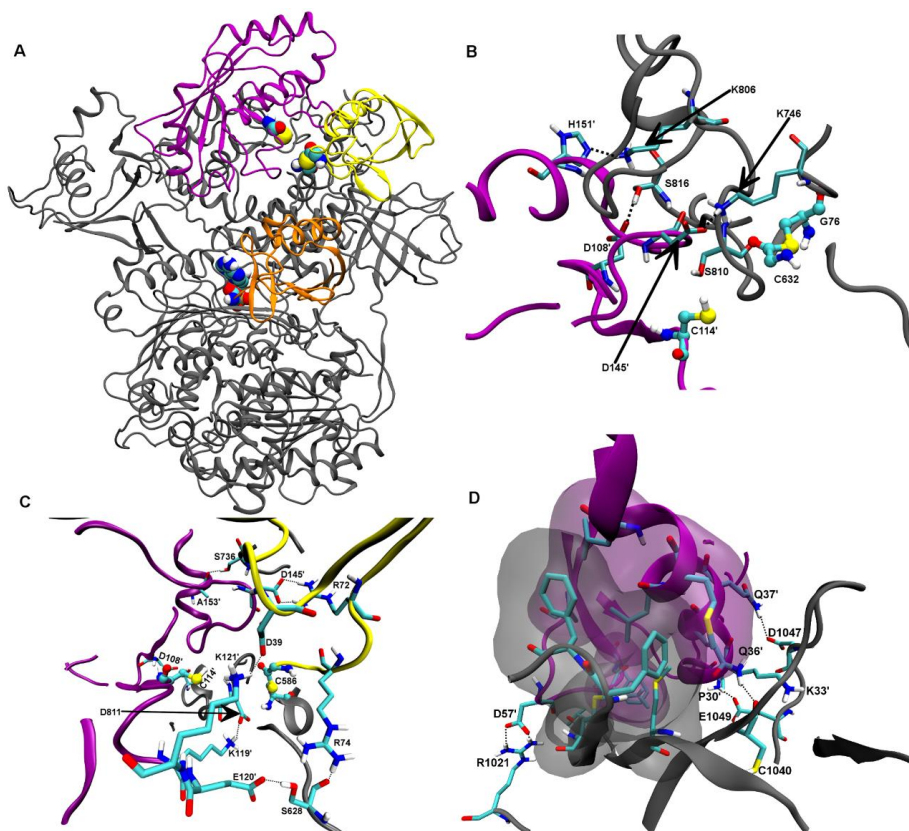


Fig. 54. Model of the hUbA1-Ub(T)-Ub(A)-UbcH10 complex. A) Average structure of last 20 ns of MD simulation of the C_Ha_R model. The catalytic cysteines, the thioester bond and AMP were highlighted in spheres. Detail of interactions between B) UbcH10 and SCCH region, C) UbcH10 and Ub(T) and D) UbcH10 and UFD region. Catalytic cysteins and the thioester bond were highlighted in CPK. Apolar hydrogens were omitted for the sake of clarity. Colour code: hUbA1, grey; sUbA1, blue; Ub(T) yellow; Ub(A), orange; UbcH10, violet. The van der Waals interactions are highlighted with transparent Connolly surfaces.

7.4 Final refinement of the tetrameric complex

Although MD simulations led to a progressive refinement of the quaternary complex, the distance between residues Cys114 in UbcH10 and the terminal glycine of the crosslinked Ub(T) was still too large (~ 8 Å; Fig. 53) as to mimic a state that resembles the catalytic arrangement of the interacting proteins. Inspection of the final MD structure showed that a closer approach between hUbA1 and UbcH10 was prevented by the Cys-cap loop, which retained the orientation found in the PDB template 3CMM. In contrast, in the available structure of the E1–E2 complex (PDB structure 4II2) the Cys-cap loop is not assigned, thus suggesting a large flexibility in the covalent construct that mimics the thioester crosslinking event. We have therefore forced the approach of UbcH10 by using steering forces applied on the sulphur of the UbcH10 Cys114 toward the carbonyl group of the crosslinked

Ub(T) C-terminal glycine, after manual removing of the Cys-cap loop. Steered molecular dynamics (SMD) simulations allowed us to reduce the distance between those atoms from 8 Å to 3.2 Å in 8 ns. After loop reconstruction, the final structure was refined in a 50 ns MD simulation, leading to a stable trajectory (Fig. 55).

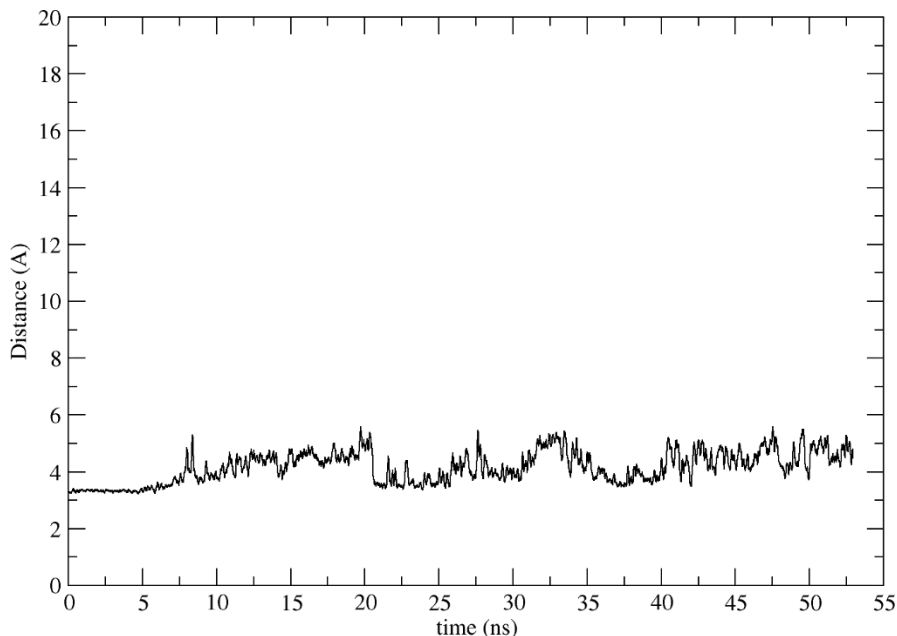


Fig. 55: Analysis of the distance between the sulphur of the UbC110 Cys114 and the carbonyl group of the crosslinked Ub(T) C-terminal glycine during the 50 ns unconstrained MD of the final model obtained after SMD.

This approach led to a closer fitting of UbC110 into the groove defined by the UFD and SCCH domains, increasing the total interaction surface, especially between hUbcA1 SCCH and the UbC110 region around the catalytic cysteine, in better agreement with the crystal structure of the E1–E2 crosslinked construct (Table 19). Moreover, SIE calculations revealed an increase of the binding energy to -42.7 kcal/mol.

Comparison of the refined model with the recently reported X-ray crystallographic structure of the trimeric complex of *S. pombe* Uba1-Ub-Ubc4 (PDB ID: 4II2) lends support to the theoretical 3D model of the quaternary complex. Thus, after deletion of the E2 partners (UbC110 and Ubc4) and the additional Ub present in the quaternary complex, superposition of the backbone C α carbon atoms leads to a positional RMSD of 2.5 Å, which indicates the similar structural arrangement of the AD, SCCH and UFD domains in the two complexes (Fig. 56). Furthermore, retention of the E2 partners in the superposed structures leads to an RMSD value of 2.6 Å, thus suggesting a similar arrangement in the trimeric and quaternary complexes.

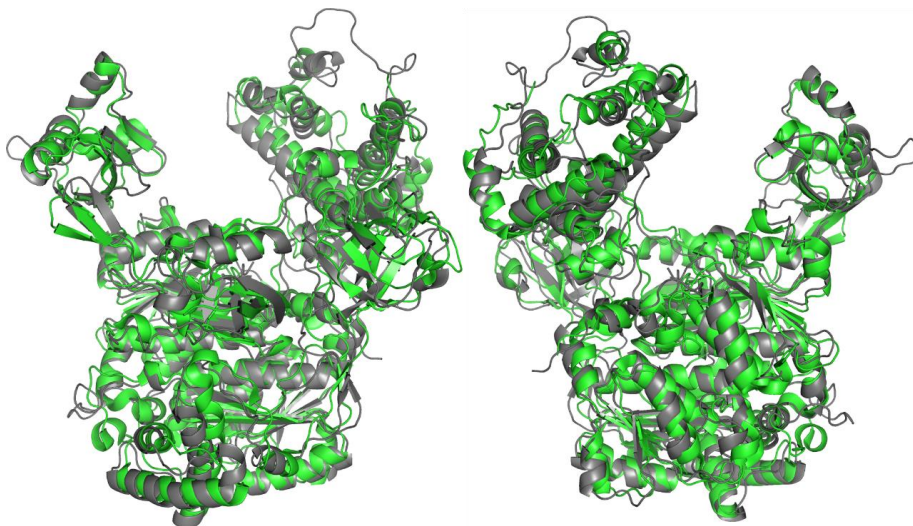


Fig. 56: Superposition of the UbA1 and Ub(A) backbone for the X-ray structure 4II2 (grey) and the 3D model of the quaternary complex (Green). Front and rear views are shown in the left and right pictures, respectively.

The analysis of the snapshots sampled in the last 20 ns of the trajectory allowed us to identify key interactions in the complex, which involve three interfaces: i) the contacts between the hUbA1 UFD domain and the UbcH10 helix H1 and $\beta 1\beta 2$ loop, ii) the interaction between the hUbA1 SCCH domain and Ub(T) with the region surrounding the UbcH10 Cys114', involving residues from the 3–10 helix and helices H2 and H3, and iii) the contacts between the hUbA1 crossing loop and Ub(A) with UbcH10.

The first interface (Fig. 57) comprises the UbcH10 residues Lys33' and Gln37', which are experimentally known to be critical for the interaction between E1 and E2 [107-109]: Lys33' interacts with Asp1042 and with Ser1044, and Gln37' is hydrogen-bonded to the backbone oxygen of Cys1040 and the hydroxyl group of Thr988 (Fig. 57F). Moreover, hydrogen bonds were also formed between the side chains of Gln36' and Asp1042, between Tyr91 and Asp1047, and between the N-terminal Pro30' with Glu1049 (Fig. 57F). Finally, the ionic interactions were supplemented by hydrophobic contacts involving hUbA1 residues Met989, Val994, Met996, Phe1000, Phe1001, and UbcH10 residues Leu42', Pro54', Leu59' and Phe60' (Fig. 57E).

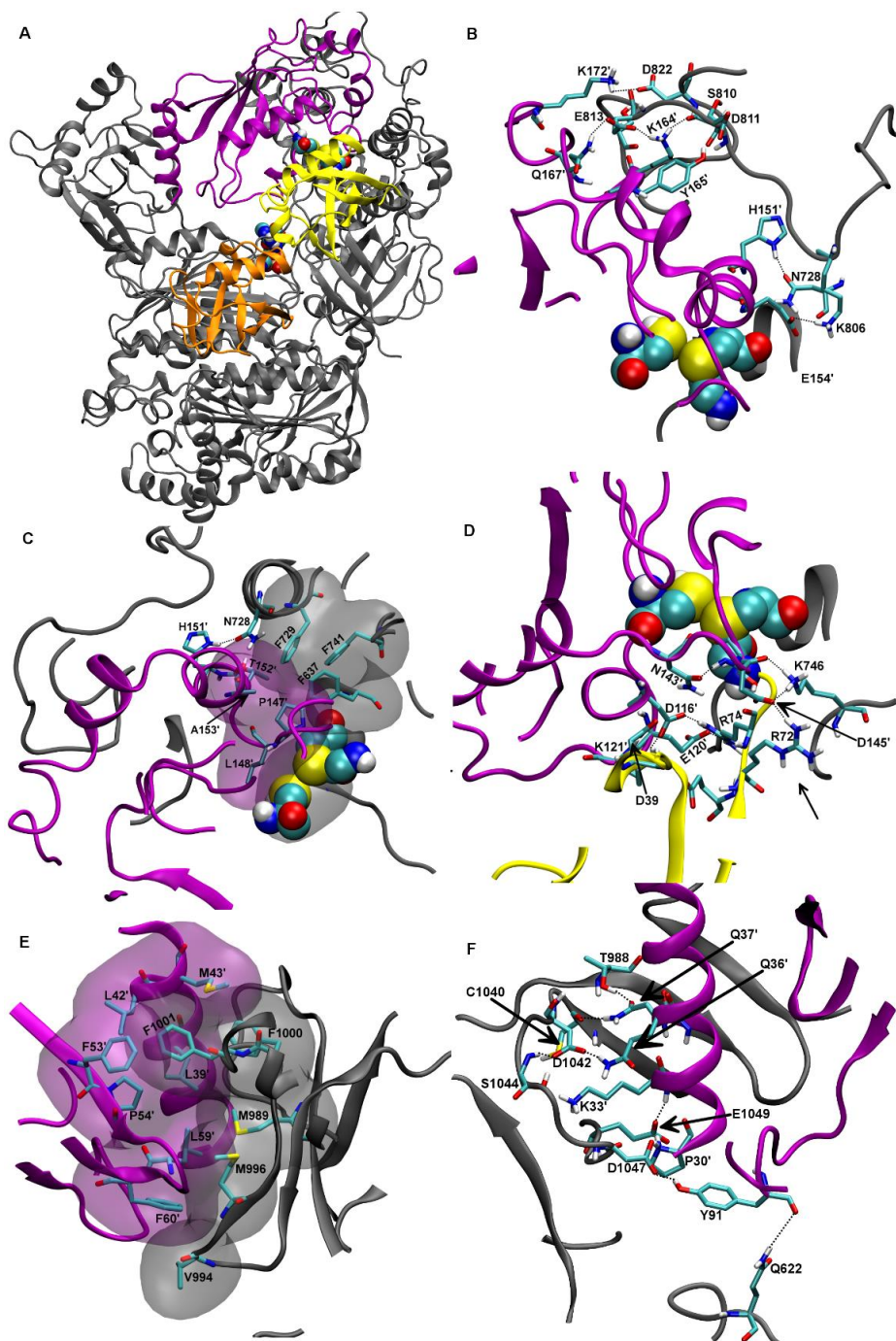


Fig. 57. Final refined model of the tetrameric complex. A) Average structure of the last 20 ns of MD simulation of the model after SMD. B) Detail of the UbCh10-Cys-cap loop interactions. C) Detail of UbCh10-Cys region involved in hydrophobic interactions; D) Detail of the UbCh10-Cys region involved in polar interactions; E) Detail of the hydrophobic interactions between hUbA1 UFD and UbCh10. F) Detail of the polar interactions between hUbA1 UFD and UbCh10. Colour code: hUbA1, grey; Ub(T) yellow; Ub(A), orange; UbCh10, violet. Catalytic

cysteins were highlighted in spheres. Apolar hydrogens were omitted for the sake of clarity. Van der Waals interactions are highlighted with transparent Connolly surfaces.

Interactions between the hUbA1 SCCH domain and the region surrounding the E2 catalytic cysteine were mainly characterized by a number of ionic and polar interactions between residues from H3 and H4 helices of UbcH10 (Glu154', Lys164', Lys172' and Tyr165') and residues from the hUbA1 Cys-cap loop (Gln728, Lys806, Glu813, Asp811 and Asp822) (Fig. 57B), while the region around the UbcH10 catalytic cysteine, including residues in the 3–10 helix, were involved in interactions with the residues around hUbA1 Cys632 and Ub(T). In particular, two main clusters of interactions are formed: i) the first, mainly based on hydrophobic interactions, between the UbcH10 helix H3 (Pro147', Ala153' and T150') with the UbA1 coiled stretch between H24 and H25 (Phe637, Phe729 and Phe741), also supported by hydrogen bonds between Asn728 with His151' and Thr150' (Fig. 57C); ii) the second mainly involves residues closer to the catalytic cysteines, such as the ionic contact between the UbcH10 Asp145' with UbA1-Lys746 and Ub(T)-Arg 72, and interactions between charged residues in the UbcH10 3–10 helix (Asp116', Asp120' and Lys121') with Ub(T) residues (Gln40, Arg74, Asp39) and with the hUbA1 FCCH domain (Glu237) (Fig. 57D).

These findings demonstrated that the crosslinked Ub plays a key role in the transthiolation intermediate with UbcH10. In particular, MD simulations highlighted that the approach of the catalytic cysteines induced a rotation of 25° of Ub(T) with respect to hUbA1 and a rearrangement of the Ub(T) pattern of interactions showed in models lacking E2 (Fig. 58).

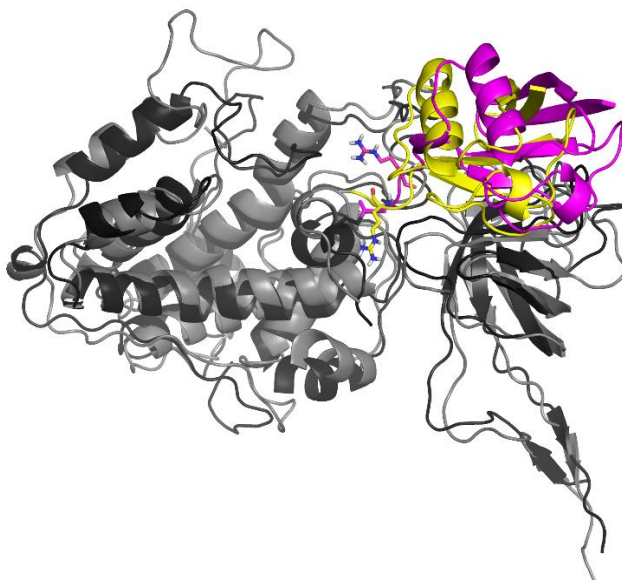


Fig. 58. Rotation of the Ub(T) induced by UbcH10 interaction in the final quaternary model with respect to the UbA1~Ub(T) model. Superimposition was made on the C α atoms of the SCCH and FCCH domains. Colour code: Final quaternary complex model: hUbA1, grey;

UbA1~Ub(T) model: UbA1, black; Ub(T), magenta; Arg74 in the two models is shown as licorice. Apolar hydrogens were omitted for sake of clarity.

In particular, in absence of E2 Arg74 was hydrogen-bonded to Cys-cap residues (Asp811 and Gln812), while in the final model it was involved in ionic interactions with UbcH10-Glu120' and Asp116', and with Glu237, bearing to the hUbA1 FCCH domain. These data support the hypothesis that products of the transthiolation reaction might be released upon a process involving the rearrangement of the Ub(T) binding to E1, driven by the charged residues in the region surrounding the catalytic cysteine of E2. Finally, we also observed some interactions in the loop region of hUbA1, in particular hydrogen bonds between the side chain of Asn622 with the backbone of UbcH10-Tyr 91' (Fig. 57F), and between the backbone of Ser628 and the side chain of Glu120' (Fig. 57D). A representative snapshot of the 3D model is available as supplemental PDB file.

7.5 Rational design of peptides that interfere with the formation of the tetrameric complex

On the basis of the 3D model of the quaternary complex, we have designed six peptides as molecular probes in order to calibrate their ability to interfere the binding of UbcH10. This strategy was motivated by two main reasons. First, the identification of short peptides that mediate protein-protein interaction seemed a priori effective for disrupting the protein-protein recognition and binding. While other strategies, i.e. introduction of specific mutations, may also be envisaged, it is unclear whether single-point mutants might lead to a significant destabilization of the complex or even to impede the formation of the quaternary complex. Second, since our ultimate goal is the design of compounds that might disrupt the ubiquitilation process, testing a series of suitably chosen short peptides represents a valuable proof of concept for supporting the potential therapeutic effect of peptidomimetics. Specifically, the peptides were designed to examine the capability of hUbA1 stretches that contribute to the protein-protein interface with UbcH10 (Fig. 59).

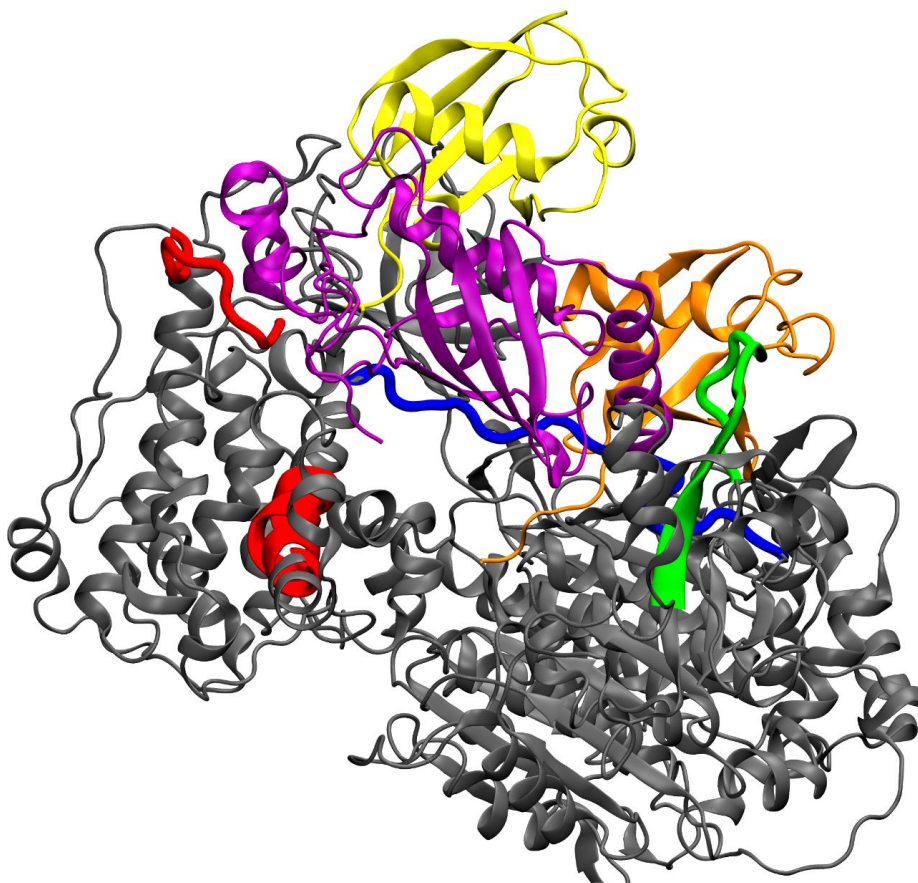


Fig. 59: Strategy of peptide design, highlights of the hUbA1 regions used to design the peptides. Colour code: hUbA1, grey; Ub(T) yellow; Ub(A), orange; UbcH10, violet; S1 and S2 red; U1 and U2 green; L1 and L2 blue.

In particular, we have designed two peptides per interface, which will be denoted S for SCCH region, L for cross loop, and U for UFD (Table 20). In the UFD region peptides U1 and U2 were selected to test the relevance of the acidic residues in mediating the binding of the UbcH10 H1 helix. In the SCCH region peptide S1 was chosen to test the role of the Cys-cap in binding UbcH10, while peptide S2, corresponding to helix H19 in the SCCH region, was designed as negative control, since the 3D model revealed the lack of any interaction in the complex. Finally, peptides L1 and L2 were chosen to explore the role of the cross loop region in assisting the interaction with UbcH10. All the peptides were synthesized as biotinylated derivatives by solid phase method and purified by RP-HPLC. Unfortunately, S1 and U2 were insoluble and so not testable in binding assays. The ability of the soluble peptides to bind recombinant GST-UbcH10 was checked by ELISA, utilizing GST as control (data not shown).

UbA1 region	peptide	sequence	K _D (μM)
UFD	U1	1038-LCCNDESGEDVEV-1050	10
	U2	1036-LELCCNDESGEDV-1048	Not soluble
SCCH	S1	807-IHVSDQELQSA-817	Not soluble
	S2	649-RDEFEGFLKQPAEN-662	No binding
LOOP	L1	621-SQDPPPEKSIPI-631	No binding
	L2	615-TEYSYSSQDPPEK-627	20
Scrambles	ScrU1	ELNCDVEVEGSDC	>100
	ScrL2	SDPSKTSEYQPSE	>80

Numbering is referred to the human UbA1 sequence. K_D values are calculated by Elisa assays.
doi:10.1371/journal.pone.0112082.t004

Table 20. Sequence and binding assays results of the designed peptides.

The best results (Table 20) were obtained with U1 and L2, which were found to bind UbcH10 with an apparent K_D of about 10 and 20 μM, respectively. In order to confirm that the binding of U1 and L2 peptides was sequence-dependent, two scrambled peptides were synthesized, ScrU1 and ScrL2. The results demonstrated that these peptides exhibited a very poor binding, much weaker than U1 and L2, which might then be considered indicative of native protein-protein interactions. In particular the good affinity showed by U1 allowed us to validate the role of the acidic residues of the UFD region in binding E2, thus giving confidence to our 3D model. The U1 peptide, indeed, contained D1047 and E1049, two of the three acidic residues involved in the hUbA1 UFD-UbcH10 H1 interface. Unfortunately, the low solubility of U2 did not allow us to verify the role of E1037, which is the third residue proven to be involved in the interaction by mutagenesis studies. Similarly, the results obtained for L2 support the role of Gln622 in assisting the interaction of the crossover loop with UbcH10, in agreement with the 3D model. The low affinity showed by L1 peptide, which contains Gln622 at the N-terminus side of the sequence, might be indicative of the importance of flanking residues in L2 binding. Finally, the results obtained from the SCCH peptides allowed us to exclude a role in the binding of the helix region corresponding to S2, as expected for this peptide, which was designed as negative control.

Overall, the results support the involvement of the selected peptides in mediating the protein-protein interactions in the hUbA1~Ub(T)-Ub(A)-UbcH10, which in turn reinforces the reliability of the 3D model built up for the quaternary complex between E1, E2 and Ub partners. On the other hand, they also demonstrate the feasibility of interfering the formation of the complex, which paves the way to the structure-based design of peptidomimetics for UbcH10-related anticancer strategies.

7.6 Conclusions

By combining homology modelling, protein-protein docking, classical and advanced MD simulations, the structural features of the proposed model have allowed us to identify the regions that mediate the recognition between the interacting proteins. In turn, this information has been used to examine the

reliability of the structural model through experimental assays performed to evaluate the binding affinities of a number of short peptides that were suitably chosen from the contact region between interacting partners in the complex. Overall, this information can be valuable to gain insight into the specificity of recognition between E1 and E2 partners, as well as for the design of peptidomimetic compounds that can bind selectively to E2s and inhibit the ubiquitination process in pathological disorders.

7.7 Experimental section

7.7.1 Homology building

The amino acid sequence of human UbA1 (hUbA1) was retrieved from the National Center for Biotechnology Information (<http://www.ncbi.nlm.nih.gov>; accession ID P22314). To find suitable templates for homology modelling, a BLASTP search was performed against the Protein Data Bank. At the beginning of this work, the search identified three templates: i) the crystal structure of mouse Ubiquitin-Activating Enzyme (PDB code 1Z7L; 2.8 Å resolution) [111], which covers 25% of the query sequence corresponding to the SCCH domain (sequence identity of 96%), ii) the crystal structure of the *Saccharomyces cerevisiae* UbA1 (scUbA1) - Ub complex (PDB code 3CMM; 2.7 Å resolution) [112], which covers 98% of the query sequence (sequence identity of 53%; similarity 71%), and iii) the NMR solution structure of a fragment of mouse UbA1 (PDB code 2V31) [113], which covers 10% of the query sequence corresponding to the FCCH region, with sequence identity of 93%. This latter structure showed that only the core region of FCCH was structured. Therefore, homology building was accomplished by using 1Z7L as template for the hUbA1 SCCH region (residues 629–884; hUbA1 numbering will be followed unless otherwise noted), and 3CMM as template for the AD, FCCH and UFD domains (residues 1–628 and 885–1057). Finally, since chains A and C in the X-ray structure 3CMM differ by a rigid-body rotation of the UFD domain, hUbA1 was modelled using the two monomers, leading then to two models hereafter designated UbA1_A and UbA1_C.

The ClustalW2 (<http://www.ebi.ac.uk/Tools/msa/clustalw2/>) [114] program was used for sequence alignment. The 3D structure of the target protein was modelled using SWISSMODEL [115]. The secondary structure of the target protein was assigned using DSSP [116]. Coordinates for two loops with undetermined coordinates in the UbA1 template structure (residues 812–824 and 964–969) were built up using the loop building ProMod tool [117] by scanning through the loop database in SWISSMODEL. The models were refined on the basis of energy minimization by GROMOS96 [118] and the models were validated for the 3D–1D profile with VERIFY3D [119], non-bonded interactions with ERRAT2 [120] and stereochemical qualities with PROCHECK [121] and WHATCHECK [122]. The comparison of the final model with the recently released structure of *Schizosaccharomyces Pombe*

UbA1 (spUbA1; PDB code 4II3) revealed similar homology parameters with hUbA1 (covered sequence 94%; sequence identity of 54%; similarity 70%) and a RMSD for the backbone atoms of 1.6 Å, thus confirming the reliability of the model.

7.7.2 General strategy for docking calculations

The 3D model of the quaternary complex between hUbA1, two Ub molecules and UbcH10 was determined by using an experimentally guided incremental strategy that relies on the building and refinement of models for the dimeric and trimeric complexes. Thus, we first explored the recognition between hUbA1 and Ub, leading to the UbA1~Ub(T) complex (Ub(T) stands for Ub bound to E1 through a thioester bond). Next, this model was used to build up the ternary UbA1~Ub(T)-Ub(A) system (Ub(A) denotes Ub bound to the AD domain). Finally, this model was the starting point for assembling the quaternary complex, UbA1~Ub(T)-Ub(A)/UbcH10. To this end, we adopted a computational approach that combines protein-protein docking, guided by the available structural information, and subsequent refinement through MD simulations (see below).

In order to generate the structural models, two docking programs were used: HADDOCK [101] and RosettaDock [102]. HADDOCK uses experimentally derived data, in conjunction with the available structures, to carry out flexible data-driven docking of proteins. Residues that are known to be implicated in the protein-protein recognition are designated active and are used to introduce suitable restraints to drive the docking process (i.e, the so-called ambiguous interactions restraints; AIRs). HADDOCK expert interface was used to generate a reasonable rough complex, which was subsequently refined with the HADDOCK refinement interface.

To assess the initial orientation of the interacting partners in order to check the suitability of the restraints to be imposed in HADDOCK calculations (i.e., the extension and solvent accessibility of the region comprising passive residues, which are solvent-exposed residues that surround the active ones) the mutual complementarity of the interacting partners was first explored by superposing the structures of Uba1 and Ub(T) in the X-ray structure of the APPBP1-Uba3~NEDD8-NEDD8-Ubc12 complex [105] (PDB entry 2NVU). A list of the restraints used in calculations is given in Table 21.

Docking step	UbA1	Ub(T)	Ub(A)	UbcH10
dimeric complex UbA1~Ub(T)	Cys632	Gly76		
	Arg239		Asp32	
trimeric complex UbA1~Ub(T)-Ub(A)	Asp576		Arg72	
	Tyr600		Gly75	
tetrameric complex UbA1~Ub(T)-Ub(A)-UbcH10			Gly76	
	Glu1037			Lys33'
	Asp1047			Gln37'
	Glu1049			
	Cys632			Cys114'

Table 21: List of the active residues used in each docking step.

Finally, the RosettaDock server performs a local docking searching for conformations near the starting 3D structure in order to find the optimal fit between the partners. It was then used to calibrate the models derived from HADDOCK.

7.7.3 The UbA1~Ub(T)-Ub(A)-UbcH10 complex

Following the incremental docking strategy, the dimeric UbA1~Ub(T) system was generated using as input structures the previously generated hUbA1_A and hUbA1_C models, and the NMR structure of human Ub (PDB ID 2K6D) [123]. For HADDOCK calculations, the active residues were only those involved in covalent interactions, i.e. UbA1 Cys632 and Ub Gly76, and passive residues were defined as neighbouring residues in a range of 8.5 Å from the active ones. Residues in the Ub tail (residues 70–76) and in the loop above the catalytic cysteine, whose coordinates were undetermined in template structures (residues 803–819), were set as fully flexible during all stages of the docking protocol. Since RosettaDock accepts a maximum of 600 residues, docking was performed using a truncated form of UbA1 that retains the residues pertaining to the interaction domain. Taking into account that RosettaDock allows the sliding of proteins around 8 Å, a binding region that includes residues 216–296 and 627–888 was defined.

The ternary complex was generated taking into account experimental information taken from the PDB structure 3CMM, in which Ub is bound to the AD domain of scUbA1. In HADDOCK calculations the active residues were those known to participate in the binding between UbA1 (Arg239, Asp576, Tyr600) and Ub (Asp32, Arg72, Gly75, Gly76). Passive residues were automatically defined as neighbours in a range of 8.5 Å from active residues. Besides the Ub tail, full flexibility was also given to residues of the

UbA1 crossover loop (residues 592–630) to facilitate the accommodation of the Ub tail.

Finally, to build up the 3D model of the quaternary complex, the UbcH10 structure was taken from PDB ID 1I7K. Let us note that this structure is functionally active even though it lacks the first 30 residues at the N-terminus [124]. Note also that Ser114 in the crystal structure was mutated to Cys to restore the native sequence. In order to enhance the sampling in predicting the quaternary complex, four starting structures of the UbA1~Ub(T)-Ub(A) complex were generated by combining the two UbA1 models (UbA1_A and UbA1_C) with two orientations of Ub in the UbA1~Ub(T) complex (denoted Ha and Hb; see below). Hence, four ternary models were used to build up the 3D structure of the quaternary complex. Active residues in HADDOCK calculations comprised those involved in E1–E2 interactions based on mutagenesis studies [105-109]: Glu1037, Asp1047 and Glu1049 in UbA1 (numbering for the UbA1-Ub2 complex), and Lys33' and Gln37' in UbcH10. Moreover, the two catalytic cysteine residues (Cys632 in UbA1 and Cys114' for UbcH10) involved in the transthiolation process were also treated as active residues in order to guide the complex formation. Passive residues were defined as neighbours in a range of 8.5 Å from active residues. Residues of the UbA1 crossover loop (residues 592–630) and the Ub tail (residues 70–76) were also flexible. Each ternary model was docked twice with UbcH10 structure yielding a total of 80 clusters.

7.7.4 Molecular Dynamics

MD simulations were performed to refine the different complexes. To this end, each complex was immersed in a pre-equilibrated octahedral box of TIP3P water molecules, and the system was neutralized. The final systems contained between 93000 and 99000 atoms. All simulations were performed with the ff99SB force field [63]. The thioester bond between Ub(T) Gly76 and UbA1 Cys362 was manually added, and suitable force field parameters were derived using $\text{CH}_3\text{CH}_2\text{SCOCH}_3$ as a representative model. The AMP position was derived from the ATP molecule as found in the PDB structure 2NVU. To this end, the AD domain of the UbA1~Ub(T)-Ub(A) model was superimposed to the AD domain of NAE1/UbA3. On the other hand, the phosphodiester bond between Ub(A) Gly76 and AMP was manually added, and the force field parameters for the phosphodiester linkage between UbA1 Cys632 and Ub(T) Gly76 were derived using $\text{CH}_3\text{OP}(\text{O})_2\text{OCOCH}_3$ as a model system.

For each complex the geometry was minimized, equilibrated and subjected to MD production run, following the general protocol described in §3.2. The structural analysis was performed using in-house software and standard codes of Amber 12.

7.7.5 Steered Molecular Dynamics and refinement of the final complex

Comparison of the final MD structures and the recently solved X-ray structure of Uba1 in complex with Ubc4 (PDB entry 4II2; [125]) showed that the loop masking the hUbA1 catalytic cysteine (Cys-cap loop) prevented a close packing between UbcH10 and the ternary complex. Accordingly, the protein-protein interface was refined by means of SMD simulations, which were set up using Amber 12. To this end, the Cys-cap loop (residues 801–825) was deleted and capping groups were added to the newly formed terminals. The distance between the sulphur atom of the UbcH10 catalytic cysteine (C114) and the carbon atom of the terminal carboxyl group of Ub(T) was constrained to 3 Å in 4 steps: i) from the initial distance (9.4 Å) to 7 Å in 0.5 ns with a force constant of 5 kcal/mol; ii) from 7 to 4 Å in 1.5 ns with a force constant of 5 kcal/mol; iii) from 4 to 3 Å in 2 ns with a force constant of 10 kcal/mol; iv) and finally from 3 to 2.5 Å in 4 ns with a force constant of 20 kcal/mol. At the end, the system was rebuilt by adding the removed Cys-cap loop (UbA1 residues 801–825), equilibrated with suitable constraints in order to relax the residues in the Cys-cap loop, and finally subjected to an unrestrained MD (50 ns) simulation.

7.7.6 Binding free energy evaluation and virtual alanine scanning

Binding free energies of the docking solutions and sampled in MD simulations were estimated using the SIE method, as described in §3.3.2. The contribution of specific residues to the binding between interacting proteins was examined by using alanine scanning [126, 127].

8. Structural studies of small Peptide Nucleic Acid, a new inhibitor of miR-509-3p involved in the regulation of Cystic Fibrosis Disease-Gene expression

The work discussed in this chapter has been published in a peer-reviewed journal article [128] and it is the result of an interdisciplinary collaboration. F. Amato, R. Tomaiuolo, A. Elce and G. Castaldo performed biological experiments; F. Nici, S. D'Errico, N. Borbone, G. Piccialli and G. Oliviero performed the PNA synthesis; G. De Rosa and L. Mayol provided technology for cell penetration; C. M. Morgillo and B. Catalanotti performed computational calculations.

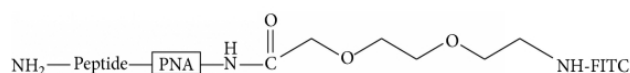
8.1 Introduction

A number of human diseases have been associated with a deregulation of specific microRNAs (miRNAs) [129–134]. Among these is the genetic disease Cystic Fibrosis (CF). CF is the most common lethal genetic disorder among Caucasians with one in every 3,000 new-borns affected. CF is due to mutations in the CFTR gene encoding the CFTR chloride channel expressed by most epithelial cells [135]. The CF phenotype typically includes the altered sweat test, pancreatic insufficiency, and pulmonary infections that gradually lead to respiratory insufficiency. To date more than 1,900 mutations of CFTR gene have been described, and a set of miRNAs inhibiting the CFTR expression at the posttranscriptional level has been described [136]. Furthermore, the group of Prof. G. Castaldo and Prof. G. Oliviero has shown that mutations in the 3'UTR of the CFTR gene may have a pathogenic effect by enhancing the affinity for the miR-509-3p miRNA [137].

The approaches to downregulate a specific miRNA essentially use oligonucleotide (ON) analogues which being complementary to miRNAs are able to reduce or inhibit their activity. Recently, several studies have demonstrated that the DNA mimics named peptide nucleic acids (PNAs) can be effectively used as anti-miRNA [138-140]. In the PNAs a 2-aminoethyl-glycine polymer replaces the ribose-phosphate DNA backbone [141]. PNA molecules are resistant to protease and nuclease degradation and recognize with a high affinity complementary fragments of DNA or RNA [142]. Many studies have been performed on the binding capability of PNAs and on the topological way in which they can recognize nucleic acids in single strand, duplex, or quadruplex arrangements to form heteroduplex, heterotriplex, and heteroquadruplex complexes [143-147] or to act as quadruplex ligands, respectively [148, 149]. The anti-miRNA activity of a PNA can occur in the

nucleus by targeting the pre-miRNA or in the cytoplasm by binding the pre-miRNA and/or the mature miRNA [150]. In both cases, it is necessary that the PNA can pass through the cell membrane and through the nuclear membrane for the former case. The main drawback in the use of PNAs as intracellular probes lies in the poor water solubility when their length exceeds the 12–14 bases. Furthermore, the cellular uptake behaviour of a PNA is not easily predictable because it is mostly dependent on the PNA base composition and the overall lipophilicity. Recent studies report on the feasibility of a miRNA regulation approach by using unmodified PNAs and PNAs conjugated with peptides or hydrophilic groups [151, 152].

The group of Prof. Oliviero (Department of Pharmacy, University of Naples) synthesized a 14-base long PNA fully complementary to the 5'-end of miR-509-3p and carrying a tetrapeptide tail containing two serine phosphates at its C-terminus and a fluorescein group at its N-terminus (PNA1, Table 22). They demonstrated, by *in vitro* studies on A549 cell lines, that the serine phosphate tail represents a suitable conjugation to improve both the water solubility and the cellular uptake of a PNA molecule. Furthermore, they have demonstrated that PNA1 is able to recognize miR-509-3p in A549 cells by reverting the expression of the luciferase gene containing the 3'UTR of the CFTR gene.



miRNA	U	G	A	U	U	G	G	U	A	C	G	U	C	U	G	U	G	G	U	A	G	
PNA1	G-S(P)-S(p)-G-a	c	t	a	a	c	c	a	t	g	c	a	g	a	Linker-FITC							
PNA2	G-S(P)-S(p)-G-a	c	t	a	a	c	c	Linker-FITC														
PNA3	G-S(P)-S(p)-G-t	t	t	t	t	t	t															

Table 22: Structures and sequences of miR-509-3p and PNA1–3. PNA sequences are written from C- to N-terminus.

Synthesis of longer PNAs (14–16 bases long) is an expensive and not an easily achievable task, especially when the PNA is conjugated to peptide tails and/or labelled at both ends. In addition, a recent study has reported that a very short LNA (8 bases long) was able to recognize and silence a family of miRNAs with no off-target effects [153]. Furthermore, experimental and computational evidence for different types of miRNA target sites demonstrated that probes with as few as seven base pairs of complementarity to the 5'-end of miRNAs are sufficient to confer regulation *in vivo* and are used in biologically relevant targets [154, 155]. The synthesis of PNA2 was preceded by a molecular modelling study aimed at evaluating the structural behaviour of the goal seven bases long miR-509-3p/PNA2 heteroduplex in comparison with that of the longer miR-509-3p/PNA1 heteroduplex. The stability and the structure of the miR-509-3p/PNA2 duplex were evaluated by molecular modelling and by UV, CD, and EMSA analyses. Based on these analyses, PNA2, notwithstanding its reduced length, was still able to

recognize miR-509-3p in A549 cells where it reverted the expression of the luciferase gene containing the 3'UTR of the CFTR gene.

8.2 MD simulations of the heteroduplex miR-509-3p/PNA1 and miR-509-3p/PNA2

The miR-509-3p/PNA2 and miR-509-3p/PNA1 heteroduplexes were built starting from the NMR structure of the RNA(GAGUUC)/PNA(GAACTC) duplex (PDB ID: 176D) [156] as described in Materials and Methods. Each system was firstly analysed by means of three runs of 20 ns molecular dynamics in order to better sample the conformational behaviour of the complexes. Secondly, in order to further assay the stability of the miR-509-3p/PNA2 duplex, we extended one run of miR-509-3p/PNA2 up to 50 ns, for a total simulation time of 90 ns for miR-509-3p/PNA2 and 60 ns for miR-509-3p/PNA1.

The macroscopic properties of the systems, such as temperature, pressure, volume, density, and energy, were fairly constant during the whole simulation for both of the systems (data not shown). As expected, the analysis of the RMSD in the trajectories of miR-509-3p/PNA2 and miR-509-3p/PNA1 complexes showed high flexibility of the single stranded miRNA segment (Fig. 60). On the contrary, the behaviour of the region of miR-509-3p hybridized with PNAs was characterized by low RMSD values and low fluctuations, thus indicating the presence of a stable secondary structure (Fig. 60).

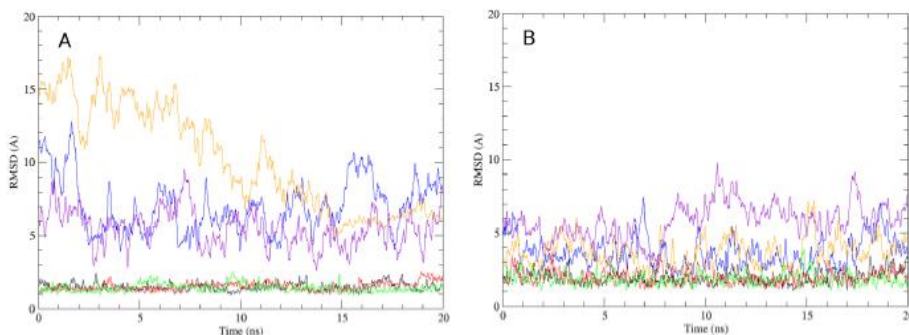


Fig. 60: Root-mean-square deviation in the three MD runs on miR-509-3p/PNA2 (a) and miR-509-3p/PNA1 (b) heteroduplexes. Superimpositions were made on the MD-averaged structures for each trajectory taking into account the whole structure (blue, orange, and purple) or only the duplex region (black, red, and green).

Moreover, the comparison of the average structures obtained from each trajectory (Fig. 61) revealed the convergence of the trajectories as shown by the low RMSD values in the duplex region of both complexes with PNA1 and PNA2 ($>0.5 \text{ \AA}$ and $>0.9 \text{ \AA}$, respectively).

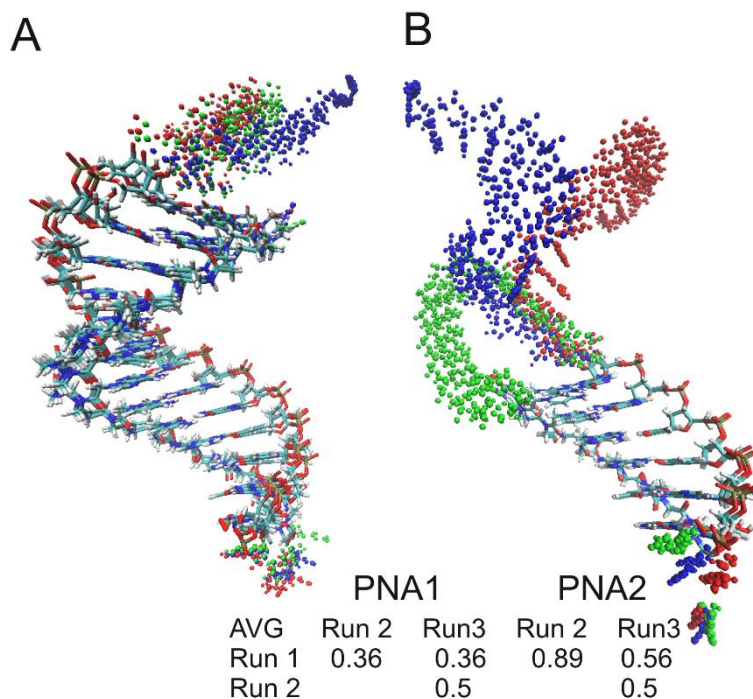


Fig. 61: Superimposition of the MD average structures of miR-509-3p/PNA1 complex (a) and of miR-509-3p/PNA2 complex (b). Duplexes regions are represented in licorice coloured by atom type (carbon in cyan, oxygen in red, nitrogen in blue, phosphate in brown, and hydrogen in white). The miR-509-3p single strand regions are represented in spheres coloured by MD run (blue, run 1; green, run 2; red, run 3). (c) RMSD in Å, calculated on phosphates in the duplexes regions, among the average structures of the MD runs.

The analysis of the helicoidal parameters and torsion angles (Table 22) demonstrated that both miRNA/PNA duplexes could be described as A-type double helix with few noticeable deviations from the canonical structure. In particular, the lower step-averaged twist values reported in Table 22 indicated a slight unwinding of the RNA/PNA helices with respect to canonical A-RNA structures, in agreement with what was previously observed in other MD simulations of RNA/PNA duplexes [157, 158]. The lower roll and tilt values observed in the MD run pointed at an expansion of the major groove. Finally, the analysis of torsion angles reported in Table 22 highlighted the strong similarity between the two duplexes.

Helicoidal Parameters							
Duplex name	Twist	Roll	Tilt	Inclination	H.Ris	H.Twi	Groove width
PNA:RNA_NMR ^a	30.1 (4)	4.9 (4.3)	1.0 (3.3)	9.0 (2.7)	2.98 (0.2)	30.6 (4.2)	6.1 (0.5)
PNA:RNA_MD ^b	23.7;23.2						
A-RNA ^c	32	12	2.8	15.8	3.3		3.8
PNA7	AVG tot	24.5 (1.1)	6.5 (1.6)	1 (0.9)	14.2 (0.6)	2.79 (0.10)	25.3 (1.1)
PNA14	AVG tot	24.9 (2.8)	5.7 (2.2)	0.9 (1.3)	13 (1.1)	2.77 (0.16)	25.5 (2.9)
Torsional PNA angles (in degrees)							
		N4-C5	C5-C	C-N1	C2-C3	C3-N4	N4-C7
PNA:RNA_NMR ^a		-84.9	80	105.7	66	-100.1	9.1
PNA7	AVG tot	-79.9	125.2	78.6	70.4	-103	-2.9
PNA14	AVG tot	-81.3	129	131.5	69.5	-103.3	-2.1
Torsional RNA angles (in degrees)							
		α	β	γ	δ	ϵ	ζ
PNA:RNA_NMR ^a		-68.4	111.75	58.4	78.5	-148.7	-72.5
A-RNA ^c		-52	175	42	79	-146	-75
AGO2-RNA ^d		-99.1	162.6	73.1	88.7	-138	-119.4
PNA7	AVG tot	-84.4	172.8	81.3	79.2	-160.4	-70.3
PNA14	AVG tot	-88.8	145.8	85.5	81.8	-161.1	-70.9

^a calculated on the average of the 10 NMR structures of PDB structure 176D; ^b From ref. M1; ^c From Ref M3; ^d From Ref MX

Table 22: Comparison of backbone torsion angles and helicoidal parameters for average structures of each run after 20 ns MD simulation. Values for structure obtained by averaging all the three runs are reported in bold. Standard deviation is reported in brackets.

Taken together, the MD results indicated that both heteroduplexes assumed a conformation resembling the canonical A-type RNA helix rather than the experimentally determined NMR structure. Moreover, the torsion angles of RNA segments in miR-509-3p/PNA2 and miR-509-3p/PNA1 duplexes showed values very similar to those adopted by miR20a in the 4F3T crystal structure [159] suggesting that PNA2 and PNA1 could easily interact with the AGO-miRNA complex, not requiring any conformational adaptations. On the basis of the positive indications coming from the MD studies, the PNA2 molecule were synthesised and was demonstrated its ability to recognize the 2'-OMe mimic of miR-509-3p by CD, UV, and EMSA studies and to restore the expression of the luciferase gene containing the 3'UTR of the CFTR gene in the presence of miR-509-3p.

8.3 Experimental section

The initial structures of the heteroduplexes formed by miR-509-3p with PNA1 and PNA2 were built by using the NMR structure of the 6-mer RNA(GAGUUC)/PNA(GAAGTC) heteroduplex (PDB ID = 176D) [157]. Starting from the lowest energy NMR structure, one nucleotide was added aligning a duplicate of the reference structure on the PNA backbone. Once the 7-mer heteroduplex was obtained, the bases were mutated to match the PNA2 sequence. Watson-Crick canonical pairs were then refined using distance restraints on the first seven bases of miR-509-3p/PNA2 heteroduplex. The

same procedure was used to build the miR-509-3p/PNA1 heteroduplex, starting from the refined structure of miR509-3P/PNA2 heteroduplex.

The equilibration of the systems and production of MD simulations were performed using the Amber 12 suite of programs [62]. The Leap module of Ambertools13 was used to create parameter and topology files for the MD simulations using the ff99SB force field for RNA and standard amino acids [160]. For PNAs parameterization we used the Sanders et al. force field for PNA [161] downloaded from the RESP and ESP charge database (R.E.DD.B. <http://q4md-forcefieldtools.org/REDDB> Project ID = F93) [162], whereas the parameters for serine phosphate were taken from reference [163]. TIP3P water molecules were added with a minimum spacing of 10.0 Å from the box edges to the RNA:PNA molecules and Na⁺ counterions were added to each system to reach the neutralization of the system.

The geometry of the system was minimized, equilibrated and subjected to MD production following the general procedure described in §3.2 During thermalization, interstrand distance restraints were applied to the RNA:PNA heteroduplex to preserve all base pairs canonical Watson-Crick bond, allowing 0.1 Å movement from the equilibrium bond distance (either closer or farther). Thus, the force constant applied during thermalization was set to 32 kcal/mol·Å² and was gradually reduced in the next step to 10 kcal/mol·Å² and subsequently decreased by increments of 5 kcal/mol·Å² in the next stages.

All production simulations were repeated in triplicate with random seeding for initial velocities and extended to 20 ns. In order to further assay the stability of the RNA:PNA heteroduplexes, we extended one run of PNA2 up to 50 ns, for a total simulation time of 90 ns for PNA2 and 60 ns for PNA1. The structural features were determined using the Curves+ software package [164], and visualization of trajectories was performed in VMD [165], while the trajectory analyses were performed using Ambertools13.

9. Conclusions

In this study we reported computational studies of the binding mode of the flurbiprofen and ibuprofen amide derivatives (Flu-AM1 and Ibu-AM5) as mean for the rational design of new potent FAAH/COX dual inhibitors. In order to investigate the binding mode of such compounds, a computational approach consisting of molecular docking, MD simulations and free energy evaluation of the ligand-receptor complexes has been applied. The molecular modelling studies point out the binding mode of the enantiomers of Ibu-AM5 and Flu-AM1 into the substrate access channel of FAAH supported by mutagenesis studies. Indeed, our results showed the formation of a stable hydrogen bond between the carbonyl amide moiety and the sidechain of Thr488, and enzymatic assays revealed lower activity of (*R*)-Flu-AM1 against the FAAH^{T488A} mutated variant. Given the potentially useful properties of compounds with combined FAAH/COX inhibitory properties, the characterisation of the binding mode of Ibu-AM5 and Flu-AM1 into the substrate access channel of FAAH provided information for the design of new derivatives. The substitution of the isobutyl group of Ibu-AM5 with (2-(trifluoromethyl)pyridin-4-yl)amino group led to the design of TPA5 derivative, showing a comparable activity ($IC_{50} = 0.59 \mu M$) with the lead (Ibu-AM5, $IC_{50} = 0.52 \mu M$). Kinetic studies of TPA5 revealed that it is a pure competitive inhibitor of rFAAH. Computational studies, exploiting QM/MM and free energies approaches, allowed us to identify a putative binding mode for TPA5, overlapping the anandamide analogue MAFP and strictly resembling the binding mode of α -ketoheterocycles, competitive FAAH inhibitors. A number of TPA5 derivatives have been designed and tested. Among them, the compound TPA27 exhibited a 10-fold enhancement in the inhibitory profile against FAAH ($IC_{50} = 0.058 \mu M$). Kinetics studies showed that TPA27, unlike TPA5, behaves as non-competitive inhibitor with K_i and α values of $0.28 \mu M$ and 1.03 , respectively. Thermodynamic Integration focussing on the transformation of TPA5 in TPA27 yielded a free energy difference of 0.3 kcal/mol demonstrating a remarkable lower affinity of TPA27 with respect to TPA5, in the competitive binding site. Moreover, incubation and time-dependency experiments demonstrated that TPA27 is a reversible inhibitor and cannot be considered as tight inhibitor. Taking together these results highlighted that TPA27 can be considered the first non-competitive reversible FAAH inhibitor reported so far, and that it more likely binds to an allosteric site.

Enzymatic and kinetics assays carried on mFAAH highlighted differences in the inhibitory potency against rat and mouse FAAH, for all the compounds studied. In particular, we observed a weakening in the inhibition against mFAAH, regardless the inhibition mechanism, suggesting a different

aminoacid composition of both competitive and non-competitive binding site. Hence, the differences in the sequence of rat and mouse FAAH, were used as criteria in the analysis of the binding site search. A putative allosteric site was found between the CP and the interface of the monomers. Computational studies in the allosteric site allowed the definition of the binding mode of Ibu-AM5 and TPA27, but not of Flu-AM1. Nevertheless, we designed a series of derivatives of Ibu-AM5 and Flu-AM1, in order to get more information on the SAR leading to the identification of derivatives with improved activity against FAAH (Ibu-AM56, $IC_{50} = 0.08 \mu\text{M}$; Ibu-AM57, $IC_{50} = 0.1 \mu\text{M}$; Flu-AM3, $IC_{50} = 0.02 \mu\text{M}$).

Results confirmed the agreement of the SAR of Ibu-AM derivatives with the selected binding mode for Ibu-AM5, but could not give useful information about the non-competitive binding mode of Flu-AM1.

However, kinetic experiments highlighted how small substitutions in the compounds, should dramatically affect the inhibition mechanism and binding preferences of these inhibitors. In light of such considerations, caution should be taken in order to derive the SAR, since apparently minor structural modifications could influence not only the binding mode, but also the inhibition mechanism.

Moreover, working on two side projects were designed potential anticancer peptides that interfere in the formation of the tetrameric complex hUbA1/UbcH10/Ub² and structural studies on the inhibition of miR-509-3p, involved in the regulation of CF, by PNA strands of various length was pursued.

Bibliography

1. Scarpelli R, Sasso O, Piomelli D. A Double Whammy: Targeting Both Fatty Acid Amide Hydrolase (FAAH) and Cyclooxygenase (COX) To Treat Pain and Inflammation.
2. Rouzer CA, Marnett LJ. Endocannabinoid Oxygenation by Cyclooxygenases, Lipoxygenases, and Cytochromes P450: Cross-Talk between the Eicosanoid and Endocannabinoid Signaling Pathways. *Chem Rev.* 2011 Oct 12; 111(10): 5899–5921.
3. Axelrod J, Felder CC. Cannabinoid receptors and their endogenous agonist, anandamide. *Neurochem Res.* 1998 May;23(5):575-81.
4. Cencioni MT, Chiurchiù V, Catanzaro G, Borsellino G, Bernardi G, Battistini L, Maccarrone M. Anandamide suppresses proliferation and cytokine release from primary human T-lymphocytes mainly via CB2 receptors. *PLoS One* 2010 Jan 14;5(1):e8688.
5. Di Marzo V, De Petrocellis L. Endocannabinoids as regulators of transient receptor potential (TRP) channels: A further opportunity to develop new endocannabinoid-based therapeutic drugs. *Curr Med Chem.* 2010;17(14):1430-49.
6. Fu J, Gaetani S, Oveisi F, Lo Verme J, Serrano A, Rodríguez De Fonseca F, Rosengarth A, Luecke H, Di Giacomo B, Tarzia G, Piomelli D. Oleyethanolamide regulates feeding and body weight through activation of the nuclear receptor PPAR-alpha. *Nature* 2003 Sep 4;425(6953):90-3.
7. Ahn K, McKinney MK, Cravatt BF. Enzymatic pathways that regulate endocannabinoid signaling in the nervous system. *Chem Rev.* 2008 May;105(5):1687-707.
8. Cravatt BF, Giang DK, Mayfield SP, Boger DL, Lerner RA, Gilula NB. Molecular characterization of an enzyme that degrades neuromodulatory fatty-acid amides. *Nature* 1996 Nov 7;384(6604):83-7.
9. Sugiura T, Kodaka T, Nakane S, Miyashita T, Kondo S, Suhara Y, Takayama H, Waku K, Seki C, Baba N, Ishima Y. Evidence that the cannabinoid CB1 receptor is a 2-arachidonoylglycerol receptor. Structure-activity relationship of 2-arachidonoylglycerol, ether-linked analogues, and related compounds. *J Biol Chem.* 1999; 274(5):2794–801.
10. Storr MA, Keenan CM, Emmerdinger D, Zhang H, Yüce B, Sibaev A, Massa F, Buckley NE, Lutz B, Göke B, Brand S, Patel KD, Sharkey KA. Targeting endocannabinoid degradation protects against experimental colitis in mice: involvement of CB1 and CB2 receptors. *J Mol Med.* 2008;86:925–936.
11. Blobaum AL, Marnett LJ. Structural and functional basis of cyclooxygenase inhibition. *J Med Chem.* 2007 Apr 5;50(7):1425-41.
12. Iñiguez MA, Cacheiro-Llaguno C, Cuesta N, Diaz-Munoz MD, Fresno M. Prostanoid function and cardiovascular disease. *Arch Physiol Biochem.* 2008;114:201–9.
13. Patrignani P, Tacconelli S, Sciulli MG, Capone ML. New insights into COX-2 biology and inhibition. *Brain Res Rev.* 2005 Apr;48(2):352-9.
14. Ghilardi JR, Svensson CI, Rogers SD, Yaksh TL, Mantyh PW. Constitutive spinal cyclooxygenase-2 participates in the initiation of

- tissue injury-induced hyperalgesia. *J Neurosci* 2004 Mar 17;24(11):2727-32.
15. Yu M, Ives D, Ramesha CS. Synthesis of prostaglandin E2 ethanolamide from anandamide by cyclooxygenase-2. *J Biol Chem* 1997 Aug 22;272(34):21181-6.
 16. Ross RA, Craib SJ, Stevenson LA, Pertwee RG, Henderson A, Toole J, Ellington HC. Pharmacological characterization of the anandamide cyclooxygenase metabolite: prostaglandin E2 ethanolamide. *J Pharmacol Exp Ther*. 2002 Jun;301(3):900-7.
 17. World Health Organization (Ed.), *Cancer pain relief: with a guide to opioid availability*, second Ed., World Health Organization, Geneva, 1996.
 18. Meade EA, Smith W L, DeWitt D L. *J. Biol. Chem.* 199.; 268:6610.
 19. Wallace, JL. Prostaglandins, NSAIDs, and gastric mucosal protection: why doesn't the stomach digest itself? *Physiol Rev*. 2008; 88:1547–65.
 20. Naidu P, Booker L, Cravatt B, Lichtman A. Synergy between enzyme inhibitors of fatty acid amide hydrolase and cyclooxygenase in visceral nociception. *J Pharmacol Exp Ther*. 2009; 329:48–56.
 21. Clapper JR, Moreno-Sanz G, Russo R, Guijarro A, Vacondio F, Duranti A, Tontini A, Sanchini S, Sciolino NR, Spradley JM, Hohmann AG, Calignano A, Mor M, Tarzia G, Piomelli D. Anandamide suppress pain initiation through a peripheral endocannabinoid mechanism. *Nat. Neurosci*. 2010; 13:1265.
 22. Sasso O, Bertorelli R, Bandiera T, Scarpelli R, Colombano G, Armirotti, A, Moreno-Sanz G, Reggiani A, Piomelli D. Peripheral FAAH inhibition causes profound antinociception and protects against indomethacin-induced gastric lesions. *Pharmacol. Res*. 2012; 65:553.
 23. Huggins JP, Smart TS, Langman S, Taylor L, Young T. An efficient randomised, placebo-controlled clinical trial with the irreversible fatty acid amide hydrolase-1 inhibitor PF-04457845, which modulates endocannabinoids but fails to induce effective analgesia in patients with pain due to osteoarthritis of the knee. *Pain* 153, 1837–46.
 24. Gatta L, Piscitelli F, Giordano C, Boccella S, Lichtman A, Maione S, Di Marzo V. Discovery of prostamide F2 α and its role in inflammatory pain and dorsal horn nociceptive neuron hyperexcitability. *PLoS ONE* 7, e31111.
 25. Cipriano M, Bjorklund E, Wilson AA, Congiu C, Onnis V, Fowler CJ. Inhibition of fatty acid amide hydrolase and cyclooxygenase by the N-(3-methylpyridin-2-yl)amide derivatives of flurbiprofen and naproxen. *Eur J Pharmacol*. 2013; 720:383–90.
 26. Cocco MT, Congiu C, Onnis V, Morelli M, Cauli O. Synthesis of ibuprofen heterocyclic amides and investigation of their analgesic and toxicological properties. *Eur J Med Chem*. 2003; 38:513–8.
 27. Morphy R, Rankovic Z. Designed multiple ligands. An emerging drug discovery paradigm. *J Med Chem*. 2005; 48:6523–43.
 28. Fowler CJ, Naidu PS, Lichtman A, Onnis V. The case for the development of novel analgesic agents targeting both fatty acid amide hydrolase and either cyclooxygenase or TRPV1. *Br J Pharmacol*. 2009 Feb; 156(3):412-9.
 29. Chebrou H, Bigey F, Arnaud A, Galzy P. Study of the amidase signature group. *Biochim Biophys Acta* 1996; 1298:285–93.

30. McKinney MK, Cravatt BF. Structure and function of fatty acid amide hydrolase. *Annu Rev Biochem* 2005; 74:411–32.
31. Patricelli MP, Lovato MA, Cravatt BF. Chemical and mutagenic investigations of fatty acid amide hydrolase: evidence for a family of serine hydrolases with distinct catalytic properties. *Biochemistry* 1999 Aug 3; 38(31):9804-12
32. Bracey MH, Hanson MA, Masuda KR, Stevens RC, Cravatt BF. Structural adaptations in a membrane enzyme that terminates endocannabinoid signaling. *Science*. 2002 Nov 29; 298(5599):1793-6.
33. Cravatt BF, Lichtman AH. Fatty Acid Amide Hydrolase: an emerging therapeutic target in the endocannabinoid system. *Curr Opin Chem Biol* 2003; 7:469-75.
34. Kage KL, Richardson PL, Traphagen L, Severin J, Pereda-Lopez A, Lubben T, Davis-Taber R, Vos MH, Bartley D, Walker K, Harlan J, Solomon L, Warrior U, Holzmann TF, Faltynek C, Surowy CS, Scott VE. A high throughput fluorescent assay for measuring the activity of fatty acid amide hydrolase. *J Neurosci Methods* 2007; 161: 47–54.
35. <http://crdd.osdd.net/oscadd/ketodrug/>
36. Seierstad M, Breitenbucher JG. Discovery and development of fatty acid amide hydrolase (FAAH) inhibitors. *J Med Chem*. 2008; 51:7327-43.
37. Wei BQ, Mikkelsen TS, McKinney MK, Lander ES, Cravatt BF. A second fatty acid amide hydrolase with variable distribution among placental mammals. *J Biol Chem*. 2006; 281:36569–78.
38. Mileni M, Johnson DS, Wang Z, Everdeen DS, Liimatta M, Pabst B, Bhattacharya K, Nugent RA, Kamtekar S, Cravatt BF, Ahn K, Stevens RC. Structure-guided inhibitor design for human FAAH by interspecies active site conversion. *Proc Nat. Acad Sci USA* 2008; 105:12820-4.
39. Bertolacci L, Romeo E, Veronesi M, Magotti P, Albani C, Dionisi M, Lambruschini C, Scarpelli R, Cavalli A, De Vivo M, Piomelli D, Garau G. A binding site for non-steroidal anti-inflammatory drugs in FAAH. *J Am Chem Soc*. 2013 Jan 9; 135(1): 22–5.
40. Ahn K, Johnson DS, Mileni M, Beidler D, Long JZ, McKinney MK, Weerapana E, Sadagopan N, Liimatta M, Smith SE, Lazerwith S, Stiff C, Kamtekar S, Bhattacharya K, Zhang Y, Swaney S, Van Becelaere K, Stevens RC, Cravatt BF. Discovery and characterization of a highly selective FAAH inhibitor that reduces inflammatory pain. *Chem Biol*. 2009; 16:411-20.
41. Mileni M, Garfinkle J, DeMartino JK, Cravatt BF, Boger DL, Stevens RC. Binding and inactivation mechanism of a humanized fatty acid amide hydrolase by alpha-ketoheterocycle inhibitors revealed from cocrystal structures. *J Am Chem Soc*. 2009; 131:10497-506.
42. Mileni M, Garfinkle J, Ezzili C, Kimball FS, Cravatt BF, Stevens RC, Boger DL. X-ray crystallographic analysis of alpha-ketoheterocycle inhibitors bound to a humanized variant of fatty acid amide hydrolase. *J Med Chem*. 2010; 53:230-40.
43. Mileni M, Kamtekar S, Wood DC, Benson TE, Cravatt BF, Stevens RC. Crystal structure of fatty acid amide hydrolase bound to the carbamate inhibitor URB597: discovery of a deacylating water molecule and insight into enzyme inactivation. *J Mol Biol*. 2010; 400:743-54.
44. Min X, Thibault ST, Porter AC, Gustin DJ, Carlson TJ, Xu H, Lindstrom M, Xu G, Uyeda C, Ma Z, Li Y, Kayser F, Walker NP, Wang Z.

- Discovery and molecular basis of potent noncovalent inhibitors of fatty acid amide hydrolase (FAAH). *Proc Natl Acad Sci USA* 2011; 108:7379-84.
45. Ezzili C, Mileni M, McGlinchey N, Long JZ, Kinsey SG, Hochstatter DG, Stevens RC, Lichtman AH, Cravatt BF, Bilsky EJ, Boger DL. Reversible competitive alpha-ketoheterocycle inhibitors of fatty acid amide hydrolase containing additional conformational constraints in the acyl side chain: orally active, long-acting analgesics. *J Med Chem.* 2011; 54:2805-22.
 46. Otrubova K, Brown M, McCormick MS, Han GW, O'Neal ST, Cravatt BF, Stevens RC, Lichtman AH, Boger DL. Rational design of fatty acid amide hydrolase inhibitors that act by covalently bonding to two active site residues. *J Am Chem Soc.* 2013; 135:6289-99.
 47. Kathuria S, Gaetani S, Fegley D, Valiño F, Duranti A, Tontini A, Mor M, Tarzia G, La Rana G, Calignano A, Giustino A, Tattoli M, Palmery M, Cuomo V, Piomelli D. Modulation of anxiety through blockade of anandamide hydrolysis. *Nat Med.* 2003; 9:76-81.
 48. Tarzia GI, Duranti A, Tontini A, Piersanti G, Mor M, Rivara S, Plazzi PV, Park C, Kathuria S, Piomelli D. Design, synthesis, and structure-activity relationships of alkylcarbamic acid aryl esters, a new class of fatty acid amide hydrolase inhibitors. *J Med. Chem.* 2003; 46:2352-60.
 49. Mor M, Rivara S, Lodola A, Plazzi PV, Tarzia G, Duranti A, Tontini A, Piersanti G, Kathuria S, Piomelli D. Cyclohexylcarbamic acid 3'- or 4'-substituted biphenyl-3-yl esters as fatty acid amide hydrolase inhibitors: synthesis, quantitative structure-activity relationships, and molecular modelling studies. *J Med Chem.* 2004; 47:4998-5008.
 50. Lodola A, Capoferri L, Rivara S, Chudyk E, Sirirak J, Dyguda-Kazmierowicz E, Andrzej Sokalski W, Mileni M, Tarzia G, Piomelli D, Mor M, Mulholland AJ. Understanding the role of carbamate reactivity in fatty acid amide hydrolase inhibition by QM/MM mechanistic modelling. *Chem Commun (Camb).* 2011; 47:2517-9.
 51. Lodola A, Mor M, Rivara S, Christov C, Tarzia G, Piomelli D, Mulholland AJ. Identification of productive inhibitor binding orientation in fatty acid amide hydrolase (FAAH) by QM/MM mechanistic modelling. *Chem Commun (Camb).* 2008; 2:214-6.
 52. Keith JM, Apodaca R, Xiao W, Seierstad M, Pattabiraman K, Wu J, Webb M, Karbarz MJ, Brown S, Wilson S, Scott B, Tham CS, Luo L, Palmer J, Wennerholm M, Chaplan S, Breitenbucher JG. Thiadiazolopiperazinyl ureas as inhibitors of fatty acid amide hydrolase. *Bioorg Med Chem Lett.* 2008; 18:4338-43.
 53. Ahn K, Johnson DS, Fitzgerald LR, Liimatta M, Arendse A, Stevenson T, Lund ET, Nugent RA, Nomanbhoy TK, Alexander JP, Cravatt BF. Novel mechanistic class of fatty acid amide hydrolase inhibitors with remarkable selectivity. *Biochemistry* 2007; 46:13019-30.
 54. Okine BN, Norris LM, Woodhams S, Burston J, Patel A, Alexander SP, Barrett DA, Kendall DA, Bennett AJ, Chapman V. Lack of effect of chronic pre-treatment with the FAAH inhibitor URB597 on inflammatory pain behaviour: evidence for plastic changes in the endocannabinoid system. *Br J Pharmacol.* 2012; 167:627-40.

55. Alhouayek M, Muccioli GG. COX-2-derived endocannabinoid metabolites as novel inflammatory mediators. *Trends Pharmacol Sci.* 2014 Jun;35(6):284-92.
56. Fowler CJ, Janson U, Johnson RM, Wahlström G, Stenström A, Norström K, Tiger G. Inhibition of anandamide hydrolysis by the enantiomers of ibuprofen, ketorolac and flurbiprofen *Arch Biochem Biophys.* 1999; 362(2):191-6.
57. Favia AD, Habrant D, Scarpelli R, Migliore M, Albani C, Bertozzi SM, Dionisi M, Tarozzo G, Piomelli D, Cavalli A, De Vivo M. Identification and characterization of carprofen as a multitarget fatty acid amide hydrolase/cyclooxygenase inhibitor. *J Med Chem.* 2012; 55(20):8807-26.
58. Fowler CJ, Bjorklund E, Lichtman AH, Naidu PS, Congiu C, Onnis V. Inhibitory properties of ibuprofen and its amide analogues towards the hydrolysis and cyclooxygenation of the endocannabinoid anandamide. *J Enzyme Inhib Med Chem.* 2013; 28:172–82.
59. Sasso O, Migliore M, Habrant D, Armirotti A, Albani C, Summa M, Moreno-Sanz G, Scarpelli R, Piomelli D. Multitarget fatty acid amide hydrolase/cyclooxygenase blockade suppresses intestinal inflammation and protects against nonsteroidal anti-inflammatory drug-dependent gastrointestinal damage. *FASEB J.* 2015 Jun;29(6):2616-27
60. Morris GM, Huey R, Lindstrom W, Sanner MF, Belew RK, Goodsell DS, Olson AJ. Autodock4 and AutoDockTools4: automated docking with selective receptor flexibility. *J Comput Chem.* 2009; 16:2785–91.
61. Gustin DJ, Ma Z, Min X, Li Y, Hedberg C, Guimaraes C, Porter AC, Lindstrom M, Lester-Zeiner D, Xu G, Carlson TJ, Xiao S, Meleza C, Connors R, Wang Z, Kayser F. Identification of potent, noncovalent fatty acid amide hydrolase (FAAH) inhibitors. *Bioorg Med Chem Lett* 2011; 21:2492-6.
62. Case DA, Darden TA, Cheatham TE III, Simmerling CL, Wang J, Duke RE, et al. AMBER 12, University of California, San Francisco, 2012.
63. Lindorff-Larsen K, Piana S, Palmo K, Maragakis P, Klepeis JL, Dror RO, et al. Improved side-chain torsion potentials for the Amber ff99SB protein force field. *Proteins.* 2010; 78:1950–8.
64. Wang J, Wolf RM, Caldwell JW, Kollman PA, Case DA. Development and testing of a general amber force field. *J Comput Chem.* 2004; 25:1157–74.
65. Bayly CI, Cieplak P, Cornell WD, Kollman PA. A well-behaved electrostatic potential based method using charge restraints for deriving atomic charges *J Phys Chem.* 1993; 97:10269–80.
66. Gaussian 09, Revision D.01, Frisch MJ, Trucks GW, Schlegel HB, Scuseria GE, Robb MA, Cheeseman JR, et al. Gaussian, Inc., Wallingford CT, USA, 2009.
67. Hou T, Wang J, Li Y, Wang W. Assessing the performance of the MM/PBSA and MM/GBSA methods. 1. The accuracy of binding free energy calculations based on molecular dynamics simulations. *J Chem Inf Model.* 2011; 51: 69–82.
68. Miller BR 3rd, McGee TD Jr., Swails JM, Homeyer N, Gohlke H, Roitberg AE. MMPBSA.py: An Efficient Program for End-State Free Energy Calculations. *J Chem Theory Comput.* 2012; 8: 3314–3321.

69. Wang J, Wolf RM, Caldwell JW, Kollman PA, Case DA. Development and testing of a general amber force field. *J Comput Chem.* 2004; 25: 1157–74.
70. Naim M, Bhat S, Rankin KN, Dennis S, Chowdhury SF, et al. Solvated interaction energy (SIE) for scoring protein-ligand binding affinities. 1. Exploring the parameter space. *J Chem Inf Model* 2007; 47:122–33.
71. Chan SL and Purisima EO. Molecular surface generation using marching tetrahedra. *J Comput Chem.* 1998; 19:1268–77.
72. Purisima EO, Nilar SH. A simple yet accurate boundary element method for continuum dielectric calculations. *J Comput Chem.* 1995; 16:681–9.
73. Steinbrecher T, Joung I, Case DA. Soft-core potentials in thermodynamic integration: comparing one- and two-step transformations. *J Comput Chem.* 2011; 32(15):3253–63.
74. Amber 14. Reference manual. <http://ambermd.org/doc12/Amber14.pdf>
75. Biasini M, Bienert S, Waterhouse A, Arnold K, Studer G, Schmidt T, et al. SWISS-MODEL: modelling protein tertiary and quaternary structure using evolutionary information. *Nucleic Acids Res.* 2014;42:W252–8.
76. Myllymäki MJ, Käsnänen H, Kataja AO, Lahtela-Kakkonen M, Saario SM, Poso A, et al. Chiral 3-(4,5-dihydrooxazol-2-yl)phenyl alkylcarbamates as novel FAAH inhibitors: Insight into FAAH enantioselectivity by molecular docking and interaction fields. *Eur J Med Chem.* 2009;44:4179–91
77. Hart T, Macias AT, Benwell K, Brooks T, D'Alessandro J, Dokurno P, et al. Fatty acid amide hydrolase inhibitors. Surprising selectivity of chiral azetidine ureas. *Bioorg Med Chem Lett.* 2009;19:4241–4.
78. Patel JZ, Parkkari T, Laitinen T, Kaczor AA, Saario SM, Savinainen JR, et al. Chiral 1,3,4-oxadiazol-2-ones as highly selective FAAH inhibitors. *J Med Chem.* 2013;56:8484–96.
79. Karlsson J, Morgillo CM, Deplano A, Smaldone G, Pedone E, Luque FJ, Svensson M, Novellino E, Congiu C, Onnis V, Catalanotti B, Fowler CJ. Interaction of the N-(3-Methylpyridin-2-yl)amide Derivatives of Flurbiprofen and Ibuprofen with FAAH: Enantiomeric Selectivity and Binding Mode. *PLoS One.* 2015 Nov 13;10(11):e0142711
80. Segel IH (1975). *Enzyme kinetics. Behavior and analysis of rapid equilibrium and steady-state enzyme systems.* John Wiley & Sons, New York.
81. Knight JL, Brooks CL 3rd. Lambda-dynamics free energy simulation methods. *J Comput Chem.* 2009 Aug;30(11):1692–700.
82. Blat Y. Non-competitive inhibition by active site binders. *Chem Biol Drug Des.* 2010;75:535–40.
83. Rome LH, Lands WEM. Structural requirements for time-dependent inhibition of prostaglandin biosynthesis by anti-inflammatory drugs. *Proc Natl Acad Sci USA.* 1975;72:4863–5.
84. Porter CT, Bartlett GJ, Thornton JM: *The Catalytic Site Atlas: a resource of catalytic sites and residues identified in enzymes using structural data.* *Nucleic Acids Res* 2004, 32(Database issue):D129–D133.
85. Mistry J, Bateman A, Finn RD: Predicting active site residue annotations in the Pfam database. *BMC Bioinformatics* 2007, 8: 298.
86. Goodey NM, Benkovic SJ: Allosteric regulation and catalysis emerge via a common route. *Nat Chem Biol* 2008, 4(8):474–482.

87. Panjkovich A, Daura X: Assessing the structural conservation of protein pockets to study functional and allosteric sites: implications for drug discovery. *BMC Struct Biol* 2010, 10: 9.
88. Le Guilloux V, Schmidtke P, Tuffery P, Fpocket: An open source platform for ligand pocket detection. *BMC Bioinformatics* 2009, 10:168.
89. Rape M, Kirschner MW. Autonomous regulation of the anaphase-promoting complex couples mitosis to S-phase entry. *Nature* 2004; 432:588–95.
90. De Gramont A, Ganier O, Cohen-Fix O. Before and after the spindle assembly checkpoint—an APC/C point of view. *Cell Cycle* 2006; 5: 2168–71.
91. Pallante P, Berlingieri MT, Troncone G, Kruhoffer M, Orntoft TF, et al. UbcH10 overexpression may represent a marker of anaplastic thyroid carcinomas. *Br J Cancer* 2005; 93:464–71.
92. Fujita T, Liu W, Doihara H, Date H, Wan Y. Dissection of the APCCdh1-Skp2 cascade in breast cancer. *Clin Cancer Res.* 2008; 14:1966–75.
93. Berlingieri MT, Pallante P, Guida M, Nappi C, Masciullo V, et al. UbcH10 expression may be a useful tool in the prognosis of ovarian carcinomas. *Oncogene* 26:2136–40.
94. Donato G, Iofrida G, Lavano A, Volpentesta G, Signorelli F, et al. Analysis of UbcH10 expression represents a useful tool for the diagnosis and therapy of astrocytic tumors. *Clin Neuropathol.* 2008; 27:219–23.
95. Troncone G, Guerriero E, Pallante P, Berlingieri MT, Ferraro A, et al. UbcH10 expression in human lymphomas. *Histopathology* 2009; 54:731–40.
96. Haas AL, Warms JV, Hershko A, Rose IA. Ubiquitin-activating enzyme. Mechanism and role in protein-ubiquitin conjugation. *J Biol Chem.* 1982; 257:2543–48.
97. Kleiger G, Mayor T. Perilous journey: a tour of the ubiquitin-proteasome system. *Trends Cell Biol.* 2014; 24:352–59.
98. Jin J, Li X, Gygi SP, Harper JW. Dual E1 activation systems for ubiquitin differentially regulate E2 enzyme charging. *Nature* 2007; 447:1135–8.
99. Fang S, Weissman AM. A field guide to ubiquitylation. *Cell Mol Life Sci.* 2004 61:1546–61.
100. Correale S, de Paola I, Morgillo CM, Federico A, Zaccaro L, Pallante P, Galeone A, Fusco A, Pedone E, Luque FJ, Catalanotti B. Structural model of the hUbA1-UbcH10 quaternary complex: in silico and experimental analysis of the protein-protein interactions between E1, E2 and ubiquitin. *PLoS One.* 2014 Nov 6;9(11):e112082.
101. de Vries SJ, van Dijk M, Bonvin AM. The HADDOCK web server for data-driven biomolecular docking. *Nat Protoc.* 2010; 5:883–97.
102. Lyskov S, Gray JJ. The RosettaDock server for local protein-protein docking. *Nuc Acids Res.* 2008; 36:W233–W238.
103. Dikic I, Wakatsuki S, Walters KJ. Ubiquitin-binding domains - from structures to functions. *Nat Rev Mol Cell Biol.* 2009; 10:659–71.
104. Schäfer A, Kuhn M, Schindelin H. Structure of the ubiquitin-activating enzyme loaded with two ubiquitin molecules. *Acta Cryst.* 2014; D70, 1311–20.
105. Huang DT, Hunt HW, Zhuang M, Ohi MD, Holton JM, et al. Basis for a ubiquitin-like protein thioester switch toggling E1–E2 affinity. *Nature* 2007; 445:394–8.

106. Tokgöz Z, Siepmann TJ, Streich F Jr, Kumar B, Klein JM, et al. E1–E2 interactions in ubiquitin and Nedd8 ligation pathways. *J Biol Chem.* 2012; 287:15512–22.
107. Pitluk ZW, McDonough M, Sangan P, Gonda DK. Novel CDC34 (UBC3) ubiquitin-conjugating enzyme mutants obtained by charge-to-alanine scanning mutagenesis. *Mol Cell Biol.* 1995; 15: 1210–1219.
108. Sullivan ML, Vierstra RD. Cloning of a 16-kDa ubiquitin carrier protein from wheat and *Arabidopsis thaliana*. Identification of functional domains by in vitro mutagenesis. *J Biol Chem.* 1991; 266:23878–85.
109. Bencsath KP, Podgorski MS, Pagala VR, Slaughter CA, Schulman BA (2002) Identification of a multifunctional binding site on ubc9p required for smt3p conjugation. *J Biol Chem.* 2002; 277: 7938–45.
110. Poornam G, Matsumoto A, Ishida H, Hayward S. A method for the analysis of domain movements in large biomolecular complexes. *Proteins* 2009; 76:201–21.
111. Szczepanowski RH, Filipek R, Bochtler M (2005) Crystal structure of a fragment of mouse ubiquitin-activating enzyme. *J Biol Chem.* 2005; 280:22006–11.
112. Lee I, Schindelin H. Structural insights into E1-catalyzed ubiquitin activation and transfer to conjugating enzymes. *Cell* 2008 134: 268–78
113. Jaremko L, Jaremko M, Wojciechowski W, Filipek R, Szczepanowski RH, et al. NMR assignment of a structurally uncharacterised fragment of recombinant mouse ubiquitin-activating enzyme. *J Biomol. NMR* 2006; 36 Suppl 143.
114. Thompson JD, Higgins DG, Gibson TJ. CLUSTAL W: improving the sensitivity of progressive multiple sequence alignment through sequence weighting, position-specific gap penalties and weight matrix choice. *Nuc Acids Res.* 1994 22: 4673–80.
115. Bordoli L, Kiefer F, Arnold K, Benkert P, Battey J, et al. Protein structure homology modeling using SWISS-MODEL workspace. *Nat Protoc.* 2009; 4(1):1–13.
116. Kabsch W, Sander C. *Biopolymers.* 1983; 22:2577–637.
117. Peitsch MC. ProMod and Swiss-Model: Internet-based tools for automated comparative protein modelling. *Biochem Soc Trans.* 1996; 24:274–79.
118. Van Gunsteren WF, Berendsen HJC. Computer simulation of molecular dynamics: Methodology, applications, and perspective in *Chemistr Angew. Chem Int Ed.* 1990; 29:992–1023.
119. Luthy R, Bowie JU, Eisenberg D. Assessment of protein models with three-dimensional profiles. *Nature* 1992; 356:83–5.
120. Colovos C, Yeates TO. Verification of protein structures: patterns of nonbonded atomic interactions. *Prot Sci* 1993; 2:1511–9.
121. Laskowski RA, MacArthur MW, Moss DS, Thornton JM. PROCHECK: a program to check the stereochemical quality of protein structures. *J Appl Cryst.* 1993; 26:283–91.
122. Hooft RWW, Vriend G, Sander C, Abola EE. Errors in protein structure. *Nature* 1996; 381:272.
123. Bezsonova I, Bruce MC, Wiesner S, Lin H, Rotin D, et al. Interactions between the three CIN85 SH3 domains and ubiquitin: implications for CIN85 ubiquitination. *Biochemistry* 2008; 47:8937–49.

124. Lin Y, Hwang WC, Basavappa R. Structural and Functional Analysis of the Human Mitotic-specific Ubiquitin-conjugating Enzyme, UbcH10. *J Biol Chem.* 2002; 277:21913–21.
125. Olsen SK, Lima CD. Structure of a ubiquitin E1–E2 complex: Insights to E1–E2 thioester transfer. *Mol Cell* 2013; 49:884–96.
126. Kortemme T, Kim DE, Baker D. Computational alanine scanning of protein-protein interfaces. *Sci STKE* 2004; 219: pl2.
127. Huo S, Massova I, Kollman PA. Computational alanine scanning of the 1:1 human growth hormone receptor complex. *J Comput Chem.* 2002; 23:15–27.
128. Amato F, Tomaiuolo R, Nici F, Borbone N, Elce A, Catalanotti B, D'Errico S, Morgillo CM, De Rosa G, Mayol L, Piccialli G, Oliviero G, Castaldo G. Exploitation of a very small peptide nucleic acid as a new inhibitor of miR-509-3p involved in the regulation of cystic fibrosis disease-gene expression. *Biomed Res Int.* 2014:610718.
129. Bader AG, Brown D, Winkler M. The promise of microRNA replacement therapy. *Cancer Res.* 2010; 70(18):7027–30.
130. Costinean S, Zaneni N, Pekarsky Y et al. Pre-B cell proliferation and lymphoblastic leukemia/high-grade lymphoma in E μ -miR155 transgenic mice. *Proc Natl Acad Sci. USA* 2006; 103(18):7024–9.
131. Rodriguez A, Vigorito E, Clare S, et al. Requirement of bic/microRNA-155 for normal immune function. *Science* 2007; 316(5824):608–11.
132. Brown PN, Yin H. PNA-based microRNA inhibitors elicit anti-inflammatory effects in microglia cells. *Chem Comm.* 2013; 49:4415–7.
133. Ullah S, John P, Bhatti A. MicroRNAs with a role in gene regulation and in human diseases. *Mol Biol. Rep.* 2013
134. Li Y, Kowdley KV. MicroRNAs in common human diseases,” *Gen Prot Bioinf.* 2012; 10:246–53.
135. McIntosh I, Cutting GR. Cystic fibrosis transmembrane conductance regulator and the etiology and pathogenesis of cystic fibrosis. *FASEB* 1992; 6(10):2775–82.
136. Gillen AE, Gosalia N, Leir SH, Harris A. microRNA regulation of expression of the cystic fibrosis transmembrane conductance regulator gene,” *Biochem.* 2011; 438(1):25–32.
137. Amato F, Seia M, Giordano S, et al. Gene mutation in microRNA target sites of CFTR gene: a novel pathogenetic mechanism in cystic fibrosis? *PLoS ONE*, 2013; 8:e60448.
138. 22-33
139. Brognara E, Fabbri E, Aimi F, et al. Peptide nucleic acids targeting miR-221 modulate p27Kip1 expression in breast cancer MDA-MB-231 cells. *Int J Onc.* 2012; 41:2119–27.
140. Torres AG, Fabani MM, Vigorito E et al. Chemical structure requirements and cellular targeting of microRNA-122 by peptide nucleic acids anti-miRs, *Nuc Acids Res.* 2012; 40(5):2152–67.
141. Fabani MM, Abreu-Goodger C, Williams D et al. Efficient inhibition of miR-155 function in vivo by peptide nucleic acids. *Nuc Acids Res.* 2010; 38(13):4466–75.
142. Nielsen PE, Egholm M, Berg RH, Buchardt O. Sequence-selective recognition of DNA by strand displacement with thymine-substituted polyamide. *Science*, 1991; 254(5037):1497–1500.

143. Pooğa M, Land T, Bartfai T, Langel U. PNA oligomers as tools for specific modulation of gene expression. *Biomol Eng.* 2001; 17(6):183–192.
144. Zhang X, Ishihara T, Corey DR. Strand invasion by mixed base PNAs and a PNA-peptide chimera. *Nuc Acids Res.* 2000; 28(17):3332–8.
145. Kushon SA, Jordan JP, Seifert JL, Nielsen H, Nielsen PE, Armitage BA. Effect of secondary structure on the thermodynamics and kinetics of PNA hybridization to DNA hairpins. *J Am Chem Soc.* 2001; 123(44):10805–13.
146. Besch R, Giovannangeli C, Schuh T, Kammerbauer C, Degitz K, Characterization and quantification of triple helix formation in chromosomal DNA. *J Mol Biol.* 2004; 341(4):979–989.
147. Nielsen PE. Peptide Nucleic Acids (PNA) in chemical biology and drug discovery. *Chem Biodivers.* 2010; 7(4):786–804.
148. Amato J, Stellato MI, Pizzo E, et al. PNA as a potential modulator of COL7A1 gene expression in dominant dystrophic epidermolysis bullosa: a physico-chemical study. *Mol BioSyst.* 2013.
149. Amato J, Oliviero G, de Pauw GE, Gabelica V. Hybridization of short complementary PNAs to G-quadruplex forming oligonucleotides: an electrospray mass spectrometry study. *Biopolymers,* 2009; 91(4):244–55.
150. Amato J, Pagano B, Borbone N et al. Targeting G-Quadruplex structure in the human c-Kit promoter with short PNA sequences. *Bioconj Chem.* 2011; 22(4):654–63.
151. van Rooij E, Olson EN. MicroRNA therapeutics for cardiovascular disease: opportunities and obstacles. *Nat Rev Drug Disc.* 2012; 11:860–72.
152. Gaglione M, Milano G, Chambery A, Moggio L, Romanelli A, Messere A. PNA-based artificial nucleases as antisense and anti-miRNA oligonucleotide agents. *Mol BioSyst.* 2011; 7(8):2490–9.
153. Manicardi A, Fabbri E, Tedeschi T, et al. Cellular uptakes, biostabilities and anti-miR-210 activities of chiral arginine-PNAs in leukaemic K562 cells. *Chem Bio Chem.* 2012; 13:1327–37.
154. Obad S, dos Santos CO, Petri A et al. Silencing of microRNA families by seed-targeting tiny LNAs. *Nat Genet.* 2011; 43(4):371–80.
155. Brennecke J, Stark A, Russell RB, Cohen SM. Silencing of microRNA families by seed-targeting tiny LNAs. *Nat Genet.* 2011; 43:371–8.
156. Patrick DM, Montgomery RL, Qi X et al. Stress-dependent cardiac remodeling occurs in the absence of microRNA-21 in mice. *J Clin Investig.* 2010; 120(11):3912–6.
157. Brown SC, Thomson SA, Veal JM, Davis DG. NMR solution structure of a peptide nucleic acid complexed with RNA. *Science,* 1994; 265(5173):777–80.
158. Soliva R, Sherer E, Luque FJ, Laughton CA, Orozco M. Molecular dynamics simulations of PNA·DNA and PNA·RNA duplexes in aqueous solution. *J Am Chem Soc.* 2000; 122(25):5997–6008.
159. Elkayam E, Kuhn CD, Tocilj A, et al. The structure of human argonaute-2 in complex with miR-20a. *Cell* 2012; 150:100–10.
160. Hornak V, Abel R, Okur A, Strockbine B, Roitberg A, Simmerling C. Comparison of multiple amber force fields and development of improved protein backbone parameters. *Proteins,* 2006; 65(3):712–25.

161. Sanders JM, Wampole ME, Chen CP, et al. Effects of hypoxanthine substitution in peptide nucleic acids targeting KRAS2 oncogenic mRNA molecules: theory and experiment. *J Phys Chem B* 2013.
162. Dupradeau FY, Cézard C, Lelong R et al. R.E.DD.B.: a database for RESP and ESP atomic charges, and force field libraries. *Nuc Acids Res.* 2008; 36(1):D360–D367.
163. Craft Jr JW, Legge GB. An AMBER/DYANA/MOLMOL phosphorylated amino acid library set and incorporation into NMR structure calculations. *J Biomol NMR*, 2005; 33(1):15–24.
164. Lavery R, Moakher M, Maddocks JH, Petkeviciute D, Zakrzewska K. Conformational analysis of nucleic acids revisited: curves+. *Nuc Acids Res.* 1996; 37(17):5917–29.
165. Humphrey W, Dalke A, Schulten K. VMD: visual molecular dynamics. *J Mol Graph.* 1996; 14(1):33–8.